

UNIVERSITY OF CALIFORNIA,
IRVINE

Molecular Regulation and Cellular Heterogeneity in Skin Repair and Hair Follicle
Regeneration

DISSERTATION

submitted in partial satisfaction of the requirements
for the degree of

DOCTOR OF PHILOSOPHY

in Biomedical Sciences

by

Daniel William Haensel

Dissertation Committee:
Professor Xing Dai, Chair
Associate Professor Max Plikus
Professor Bogi Andersen
Professor Peter Donovan

2019

DEDICATION

All work is dedicated in loving memory to my mom, Carole Haensel

1956-2016

TABLE OF CONTENTS

	Page
LIST OF FIGURES	v-vii
LIST OF TABLES	viii
ABBREVIATIONS	ix
ACKNOWLEDGMENTS	x
CURRICULUM VITAE	xi-xii
ABSTRACT OF THE DISSERTATION	xii-xv
CHAPTER 1: Introduction	1-35
CHAPTER 2: Materials and Methods	36-50
CHAPTER 3: An <i>Ovol2</i> -Zeb1 transcriptional circuit regulates epithelial directional migration and proliferation	51-83
CHAPTER 4: Single-cell transcriptomics reveal molecular and metabolic heterogeneity of epidermal basal cells during skin wound healing	84-135
CHAPTER 5: Summary and Conclusions	135-144
APPENDIX 1: <i>Ovol1</i> in adult AD model	145-153
APPENDIX 2: Inducible deletion of <i>Ovol2</i> in HF and epithelial cells	154-158
APPENDIX 3: Immune response characterization in <i>Ovol2</i> SSKO wounds	159-163
APPENDIX 4: <i>Ovol1</i> / <i>Ovol2</i> double knockout generation and initial phenotypic analysis	164-167
REFERENCES	168-187

LIST OF FIGURES

	Page
Figure 1.2 EMT-associated cellular and molecular events during mammalian cutaneous wound re-epithelialization	34
Figure 3.1 Growth and gene expression defects in <i>Ovo/2</i> -deficient NBPKs	68
Figure 3.2 <i>Ovo/2</i> expression in normal and wounded adult skin	70
Figure 3.3 <i>In vivo</i> and <i>ex vivo</i> evidence for skin wound healing defects in <i>Ovo/2</i> SSKO mice	72-73
Figure 3.4 <i>In vivo</i> and <i>ex vivo</i> evidence for <i>Ovo/2</i> loss-induced HF defects	74-75
Figure 3.5 <i>Ovo/2</i> -deficient Bu-HFSCs display aberrant cell division behavior and arrest in G2/M->G1 transition	79
Figure 3.6 Compromised directional migration of <i>Ovo/2</i> -deficient Bu-HFSCs is rescued by <i>Zeb1</i> deletion	80-81
Figure S3.1 Supplemental data on NBPK analysis	69
Figure S3.2 Supplemental data on wound healing analysis	71
Figure S3.3 Supplemental data on HF analysis	76-77
Figure S3.4 Supplemental data on Bu-HFSC analysis	78
Figure S3.5 Supplemental data on Bu-HFSC migration	82-83
Figure 4.1 scRNA-Seq reveals global changes in cellular makeup during wound healing	107-108
Figure 4.2 Wound epidermal basal cells show upregulated expression of inflammation-and migration-related genes	116
Figure 4.3 Three distinct non-proliferative basal cell subsets exist in un-wounded skin	118-119
Figure 4.4 Alteration and spatial partitioning of basal cell subsets in wounded skin	122-123

Figure 4.5	Metabolic heterogeneity in basal cells of the normal and wounded skin	127
Figure 4.6	Pseudotemporal ordering and RNA velocity analysis reveal three different programs	129-130
Figure S4.1	Proliferation dynamics and quality control metrics	109
Figure S4.2	Replicate IDs and associated marker genes with heatmaps	110-111
Figure S4.3	Feature plots of major cell type populations containing all samples (2 UW and 3 WO)	112
Figure S4.4	scRNA-Seq reveals minor changes in epithelial cellular makeup during wound healing	113-114
Figure S4.5	Associated marker genes with heatmaps for epithelial cells from UW and WO samples	115
Figure S4.6	Proliferative basal cells have dramatically distinct gene expression patterns compared to non-proliferative basal cells	117
Figure S4.7	Basal cell analysis in UW skin	120-121
Figure S4.8	Basal cell states are similar in UW and WO samples	124
Figure S4.9	GO and marker gene analysis of basal cells from WO sample	125-126
Figure S4.10	Spatial localization of basal cells during repair dictates metabolic state	128
Figure S4.11	Monocle lineage analysis in UW and WO skin	131
Figure S4.12	Lineage analysis by scEpath and RNA Velocity	132-133
Figure S4.13	Pseudotemporal changes in gene expression	134-135
Figure A1.1	Ovol1-null mice have enhanced AD-like symptoms when treated with MC903	151
Figure A1.2	Ovol1-null mice have enhanced AD-like symptoms in sham-treated ears	152
Figure A1.3	Ovol1-null mice have altered endemic and systemic immune responses	153

Figure A2.1 Inducible deletion of <i>Ovol2</i> in HF and epithelial cells using Sox9CreERT	157
Figure A2.2 Inducible deletion of <i>Ovol2</i> in HF and epithelial cells using K14CreER	158
Figure A3.1 Immune response characterization in <i>Ovol2</i> SSKO wounds	163
Figure A4.1 <i>Ovol1/Ovol2</i> double knockout generation and initial phenotypic analysis	167

LIST OF TABLES

	Page
Table 1.2 Comparison of cellular and molecular changes between cutaneous wound re-epithelialization and EMT	35

ABBREVIATIONS

HF	Hair follicle
EMT	Epithelial to mesenchymal transition
scRNA-Seq	Single cell RNA-Seq
EpdSCs	Epidermal stem cells
K14	Keratin 14
K5	Keratin 5
K10	Keratin 10
K1	Keratin 1
DP	Dermal papilla
HG	Hair germ
SHH	Sonic hedgehog
IRS	Inner root sheath
Bu-HFSCs	Bulge hair follicle stem cells
ICS	Intermediate cell states
TF	Transcription factor
EMT-TF	EMT transcription factor
ECM	Extracellular matrix
MET	Mesenchymal to epithelial transition
ER	Early response
GA	Growth arrested

ACKNOWLEDGMENTS

Throughout my tenure as a graduate student, I have been fortunate to work with fantastic colleagues both within my lab as well as throughout the UCI campus. Within the lab, I have to first and foremost thank my advisor, Xing Dai who was able to provide unparalleled support and motivation throughout my entire time in the lab. I'm so very fortunate to have joined her lab and I know that I have received excellent training which will allow me to be successful in my future endeavors. I want to thank all Dai lab members, past and present but especially Peng, Kazu, Alvaro, Yuan, Morgan, and Lupe for all of their training and assistance. I have to thank my thesis committee members, Peter, Max, Bogi, and Kai for all of their support, suggestions, and encouragement through my graduate work. I wanted to extend a special thanks to Qing Nie for both the funding support through NSF-Simons center as well as all of the collaborative support. In Qing's lab, I wanted to thank all of the fantastic computational collaborators, especially Suoqin, Adam, and Zixuan. Special thanks to all the members of UCI's Skin Club and especially its organizer, Scott Atwood for creating a collaborative environment to share our latest research.

CURRICULUM VITAE

Daniel W Haensel

Education:

2019 Ph.D. Biomedical Sciences, University of California, Irvine
2013 B.S. Biological Sciences, Cal Poly San Luis Obispo (Cum Laude)

Professional Experiences:

2013-19 Graduate Student Researcher
Xing Dai Laboratory, University of California, Irvine

2010-13 Undergraduate Student Researcher
Elena Keeling Laboratory, Cal Poly San Luis Obispo

2013 Medical/Scientific Affairs Intern
Roche Molecular Diagnostics, Pleasanton, CA

2012 Summer Intern
Genentech, South San Francisco, CA

Fellowships:

2018-19 NSF Simons Graduate Fellowship
NSF-Simons Center for Multiscale Cell Fate Research

Publications:

Haensel D, Jin S, Sun P, Dragan M, Cinco-Hedde R, MacLean A, Nguyen Q, Kessenbrock K, Gratton E, Nie Q, and Dai X (2019). "Molecular and metabolic heterogeneity of epidermal basal cells during skin wound healing." (In preparation).

Sun P, **Haensel D**, Dey P, Huang D, Watanabe K, de Feraudy S, Ganesan A, Pearlman E, and Dai X (2019). "Functional modulation of skin inflammatory responses by epidermally derived transcription factor *Ovol1*." (In preparation).

Sha Y*, **Haensel D***, Gutierrez G, Du H, Dai X, and Nie Q (2019). "Intermediate cell states in epithelial-to-mesenchymal transition." Physical Biology 16 (2).

* Denotes co-first authors

Haensel D, Sun P, MacLean AL, Ma X, Zhou Y, Stemmler M, Brabletz S, Berx G, Plikus M, Nie Q, Brabletz T, and Dai X (2019). "An *Ovol2*-*Zeb1* transcriptional circuit regulates epithelial directional migration and proliferation." EMBO Rep 20 (1): e46273.

Du H, Wang Y, **Haensel D**, Lee B, Dai X, and Nie Q (2018). "Multiscale modeling of layer formation in epidermis." PLoS Comput Biol 14 (2): e1006006.

Haensel D, McNeil MA, and Dai X (2018). "Ex Vivo Imaging and Genetic Manipulation of Mouse Hair Follicle Bulge Stem Cells." Methods Mol Biol 1879: 15-29.

Haensel D and X Dai (2018). "Epithelial-to-mesenchymal transition in cutaneous wound healing: Where we are and where we are heading." Dev Dyn 247 (3): 473-480.

Lee B, Watanabe K, **Haensel D**, Sui J, and Dai X (2017). "Overexpression of Transcription Factor *Ovol2* in Epidermal Progenitor Cells Results in Skin Blistering." J Invest Dermatol 137 (8): 1805-1808.

Presentations:

- Early-Career Researcher Symposium, NSF-Simons Center for Multiscale Cell Fate Research, Irvine, CA, March 2019 (talk and poster)
- Multiscale Modeling Consortium Meeting: Translation and Dissemination, NIH, March 2019 (poster)
- NSF-Simons Center for Multiscale Cell Fate Research Annual Symposium, October 2018 (poster)
- UC Irvine Skin Symposium, September 2018 (poster)
- Society for Investigative Dermatology, Orlando, FL, May 2018 (poster)
- Society for Investigative Dermatology, Portland, OR, April 2017 (poster)
- Gordon Research Conference: Tissue Niches & Resident Stem Cells in Adult Epithelia, Hong Kong, China, August 2016 (poster)
- International Society for Stem Cell Research, San Francisco, CA, June 2016 (poster)

ABSTRACT OF THE DISSERTATION

Molecular Regulation and Cellular Heterogeneity in Skin Repair and Hair Follicle
Regeneration

By

Daniel William Haensel

Doctor of Philosophy in Biomedical Sciences

University of California, Irvine, 2019

Professor Xing Dai, Chair

Epithelial tissues are groups of cells, typically tightly adherent to one another, organized as sheets, and lining various tissues. Maintenance of epithelial tissues such as the adult mouse epidermis and hair follicle is largely driven by epithelial stem cells, which have the ability to give rise to the various epithelial cell types that make up these tissues. At a broad level, the focus of this dissertation is multifaceted but aims to add to a better understanding of epithelial stem cell function, regulation, and how these stem cells alter their cellular dynamics (proliferation, differentiation, heterogeneity, and migration) in the context of wound healing.

Chapter 3 focuses on a continuation of previous work from the lab that aims to elucidate the function of *Ovol2* in the context of hair follicle (HF) regeneration and epidermal repair. Previous work had explored the function of *Ovol2*, a known transcriptional repressor of the epithelial to mesenchymal transition (EMT) in the context of mouse epidermal development, but whether *Ovol2* has critical functions during the dramatically distinct processes in the adult mouse isn't clear. As *Ovol2* regulates EMT, this work addresses larger questions associated with whether the EMT process itself

plays distinct roles in previously underexplored biological processes such as during HF regeneration, a process associated with dynamic epithelial stem cell cellular movements. Cellular movements during epidermal repair have been shown to be largely driven by transcriptional regulators that promote partial-EMT events. Understanding how these regulators both promote the necessary migratory abilities of epidermal cells to facilitate wound closure but maintain cellular adhesions throughout the repair process is not well understood. Beyond the migratory properties associated with epidermal cells during wound healing is their ability to exhibit directional migration. In this work, I show that loss of *Ovol2* leads to both defective HF regeneration and wound repair. These defects are associated with enhanced migratory behaviors and loss of directional type movements. I show that the *Ovol2*-*Zeb1* molecular circuit (through *Ovol2*'s transcriptional repression of *Zeb1*) is critical for regulating the directional migration of epithelial cells. Although this work provides detailed insight into a critical aspect of repair, wound healing involves many other cell types as well as many other cellular dynamics.

Chapter 4 takes a dramatically different approach, utilizing single cell RNA sequencing (scRNA-Seq) to ask questions at a more global level, directly comparing wounded and un-wounded skin. Isolating total skin during both normal homeostasis and during re-epithelialization, a stage of active wound repair where epidermal cells utilize partial-EMT events to facilitate wound closure, allowed for a whole skin wide characterization and comparison of the key differences between these two states. Here I addressed global changes in cellular heterogeneity, characterizing the major cell types that are present in normal skin and during active wound healing. I then computationally subset epidermal stem cells (or basal cells) for extensive analysis probing for presence

of basal cell heterogeneity represented by various cellular states during normal homeostasis. Lineage tracing studies have suggested that there exists some sort of hierarchy within the basal layer of the epidermis but there lacks a global perspective of basal cell heterogeneity. I identify four distinct basal cell states, which are subsequently confirmed in situ. Beyond identification of these different states, we arrange these different states in a lineage hierarchy, identifying a population enriched for *Col17a1* and *Trp63* as the most stem-like. I then ask a fundamental question of whether this heterogeneity I observed in normal skin during homeostasis is also present during active wound healing. I show that the same cellular states exist but in different proportions, with the expansion of a growth arrested (GA) population, which has distinct migratory, immune, and metabolic characteristics distinct from the other basal cell states.

Overall, this thesis work takes a multi-scale approach, understanding global changes in cellular processes such as epithelial homeostasis and repair as well as taking a more focused approach, elucidating transcriptional regulators that govern cellular dynamics in epithelial stem cells.

CHAPTER 1: INTRODCUTION

Incorporates components from published review articles:

Article #1

Epithelial-to-Mesenchymal Transition in Cutaneous Wound Healing: Where We Are and Where We Are Heading

Daniel Haensel and Xing Dai; Developmental Dynamics 2018

Article #2

Intermediate cell states in epithelial-to-mesenchymal transition

Yutong Sha*, Daniel Haensel*, Guadalupe Gutierrez, Huijing Du, Xing Dai, and Qing Nie; Physical Biology 2019 (“*” denotes co-first authors)

Epithelial tissues

Epithelial tissues such as the epidermis play a myriad of critical roles involving barrier functions, protecting the organism from the external environment. Epithelial cells are tightly adhered to one another and tend to be organized as sheets, which generally encapsulate a particular tissue providing an interface between the organ and the environment (Blanpain and Fuchs 2014). Although epithelial tissues are quite diverse, the development and subsequent maintenance of epithelial tissues are largely driven by epithelial stem cells (Blanpain and Fuchs 2014). The dynamics of epithelial stem cells vary among the different tissue types, but also vary temporally depending on the developmental status, whether the tissue has incurred damage, or the pathological status of the tissue (Blanpain and Fuchs 2014; Gonzales and Fuchs 2017). While epithelial development is characterized by the complete formation of the tissue, after formation, epithelial tissues typically still require inputs from resident epithelial stem cells to maintain tissue homeostasis. Even within adult epithelial tissues, there are a multitude of different epithelial stem cells, which depending on that particular tissue, can vary in characteristics such as their potency (unipotent vs. multipotent) and proliferation rate (Blanpain et al., 2007; Blanpain and Fuchs 2014). Intestinal stem cells for example are fast cycling as the tissues is rapidly and consistently regenerated (Blanpain and Fuchs 2014; Blanpain et al., 2007). These dynamics stand diametrically opposed to the proliferative dynamics observed in the hair follicle (HF), which spend long periods of time in stages of quiescence except at defined points where the stem cells receive cues to actively proliferate to give rise to a new HF (Blanpain and Fuchs 2014; Gonzales and Fuchs 2017). This cyclical behavior of stem cells is also observed in the mammary gland, where the mammary

epithelium undergoes dramatic hormone-induced changes during pregnancy to facilitate lactation before returning to a more static state (Blanpain and Fuchs 2014; Inman et al., 2015). Stem cell dynamics are sensitive to alterations induced by wounding, pathogenesis such as in cancer, or transplantation experiments (Blanpain and Fuchs 2014). During wounding, damage to the epithelial tissues is repaired because epithelial tissues have critical barrier functions such as in the epidermis (Gonzales and Fuchs 2017). Overall, epithelial stem cells maintain epithelial tissues, generating the various differentiated cells that make up the epithelial tissue but the exact mechanisms that govern epithelial stem cells and their specific cellular dynamics varies from tissue to tissue.

Mouse epidermis

The mouse skin represents a critical barrier tissue, protecting the organism from the external environment. The skin contains multiple epithelial components such as the epidermis and HF, which have their own sets (sometimes multiple) of epithelial stem cells. Both the epidermis and HF represent models to study the molecular and cellular mechanisms that control stem cell function. The epidermis and HF derive from a single layered epithelium called the surface ectoderm, which undergoes extensive morphogenic events at E14.5 and E15.5 to specify the HF and epidermis respectively (Gonzales and Fuchs 2017). At this stage, the epidermis stratifies when progenitor cells from the single layer begin to divide obliquely with respect to the basement membrane (Gonzales and Fuchs 2017). These progenitors, basal cells, or epidermal stem cells (EpdSCs) represent the stem cells of the interfollicular epidermis (Gonzales and Fuchs 2017). EpdSCs can

proliferate and have self-renewal capabilities, maintaining the pool of EpdSCs but giving rise to differentiated cell types. More than 50% of mitotic events in the EpdSCs are perpendicular to the basement membrane generating an EpdSC and differentiated suprabasal daughter cell. This process and determination of which cell will differentiate is regulated by Notch signaling where Notch levels are differentially elevated in the suprabasal daughter cell leading to generation of a differentiated spinous cell in suprabasal positions (Gonzales and Fuchs 2017). The different cells that make up the epidermis (EpdSCs and differentiated cells) express different keratins along with other markers allowing for fairly straightforward examination of the differentiation status of the epidermis. The EpdSCs express high levels keratin of 14 (K14) and 5 (K5), which can then differentiate into spinous cells, which express keratin 10 (K10) and 1 (K1). Subsequent differentiation events lead to generation of the granular layer and finally the stratum corneum, expressing structural molecules such as loricrin (Lor) or involucrin (Inv) (Hsu et al., 2014; Gonzales and Fuchs 2017).

Adult mouse epidermis is thinner than developing epidermis but is still dependent on the EpdSCs for the homeostatic maintenance, or proliferation and differentiation to replace differentiated cells which are lost. These proliferative progenitors alter their orientation of cellular divisions, switching to largely parallel divisions (Gonzales and Fuchs 2017). Multiple studies have examined the homeostatic maintenance of the epidermis, monitoring the proliferative dynamics of EpdSCs as well as their ability to differentiate. Beyond the technical complications involved in measuring these dynamics, different anatomical locations (i.e. epidermis from dorsal skin or mouse foot pad) have distinct proliferative dynamics. Within dorsal skin, the homeostatic flux and turnover of the

epidermis is about one week (Gonzales and Fuchs 2017). Complicating these intricate studies in the dorsal regions is the presence of the dense number of HFs, where proximity to a HF can influence and alter proliferative dynamics (Gonzales and Fuchs 2017) . As such, a number of studies have utilized other models such as ear, paw and tail epidermis. Although these studies provided a wealth of knowledge, they have produced at times, varied results. This is in large part due to varied proliferative dyanmics of EpdSCs in these different locations, making generalizable conclusions regarding basal cells complicated (Gonzales and Fuchs 2017).

Traditionally, lineage tracing strategies coupled with various *in vitro* and *in vivo* experiments such as transplantation studies are used to putatively define stem cell populations. Traditional lineage tracing techniques include methods to mark slow cycling cells (label retaining cells, or LRCs) or genetic labeling using promoter activity of reporter genes to drive marker (e.g. fluorescence protein) expression in the presumptive stem cells and all their daughter cells (Hsu 2015). Various lineage tracing experimental approaches have been utilized in the epidermis at all major locations (back skin, ear, paw, and tail) to better define epidermal dynamics. These studies have shown that there is are indeed cells that have greater potential relative to other cells (extensively reviewed in Gonzalez and Fuchs 2017). Initial key work utilized a lineage tracing approach to fluorescently labeled cells by the promoter activity of K14 (EpdSC marker) and involucrin (*Inv*, differentiated cell marker). With this labeling, both *K14*- and *Inv*-expressing basal cells within the epidermis were monitored and their fates traced (Mascré et al., 2012). These different cells were found to have different potentials; more specifically, cells targeted by *K14-Cre-ER* are longer lived epidermal stem cells relative to the cells were

labeled by *Inv-Cre-ER* (Mascré et al., 2012). Other recent work has attempted to exploit the notion that stem cells are slow cycling (LRCs) (Sada et al., 2016). A sophisticated sorting strategy was used to isolate and subsequently transcriptionally profile LRCs and non-LRCs from the epidermis in order to identify key differences between these cells. The genes *Dlx1* and *Slc1a3* were identified to be specific to the LRCs and non-LRCs respectively and their promoters were subsequently utilized for traditional lineage tracing approaches (Sada et al., 2016). These studies also identified that there is some hierarchy within the basal layer of the epidermis. Although this work provides interesting insight into the basal cell dynamics, in general, it is thought that the skin epidermis is replenished by long term, relatively fast-cycling undifferentiated progenitors (Gonzales and Fuchs 2017). With this notion, using a cells label retention ability as a functional readout of stemness might not be an ideal method to assess the potential of a generally actively cycling progenitor population (Gonzales and Fuchs 2017). It is possible that LRC-type do exist but whether they are major contributors to the normal homeostatic maintenance of the adult epidermis is not clear. In this work my studies set out to better address heterogeneity, using scRNA-Seq to transcriptionally profile all basal cells during normal homeostasis, which provides a global perspective.

Mouse hair follicle

The other major epithelial component of the skin is the HFs, representing a dynamic mini-organ skin appendage with their own specific resident stem cell populations (Gonzales and Fuchs 2017). HFs originate during embryogenesis from placodes, which are formed via congregation of WNT^{hi} cells within the single-layered surface ectoderm

(Gonzales and Fuchs 2017). Cells within the placode then begin to divide in a perpendicular manner relative to the basement membrane, releasing sonic hedgehog (SHH) signals into the mesenchyme, generating the dermal condensate, which can become dermal papilla (DP) (Gonzales and Fuchs 2017). Depending on the level of bone morphogenic protein (BMP) signaling produced by the dermal condensate, the cells in the placode can then be driven to either HF or sweat gland fate (Gonzales and Fuchs 2017). If designated for HF fate, WNT signaling in the region overlying the SHH-expressing cells begins to lessen, generating a WNT^{low} population that eventually become the outer root sheath (ORS) of the HF, which will lead to development of the bulge hair follicle stem cells (Bu-HFSCs). The remaining WNT^{hi} cells generate the inner root sheath (IRS) and hair shaft (Gonzales and Fuchs 2017).

After specification and initial development, the adult mouse hair follicle goes through cyclical stages of resting (termed telogen), growth (termed anagen), and regression (termed catagen). The regeneration of the HF is fueled by typically quiescent Bu-HFSCs and a primed population called the hair germ (HG) (Cotsarelis et al., 1990; Gonzales and Fuchs 2017). These stem cell populations are maintained in quiescence for extensive periods of time due in part to a number of mechanisms such as BMP4 signaling from dermal fibroblasts, BMP2 signaling from subcutaneous fat, as well as BMP6 and FGF-18 signaling originating from the K6+ inner bulge region (Hsu et al., 2014). To initiate anagen, signaling from the dermal papilla (DP) such as TGF β 2, FGF10, and WNT lead to HG activation (Hsu et al., 2014; Gonzales and Fuchs, 2017). Once activated, the HG population will begin to proliferate, generating a transient amplifying population known as matrix cells. Once these matrix cells begin to start expressing SHH,

the Bu-HFSCs will also begin to start proliferating (Hsu et al., 2014). Although the Bu-HFSCs do proliferate, the major contributor to HF regeneration are the HG cells, as they actively proliferate and differentiate into various cell types that make up the HF, such as the inner root sheath and the hair shaft (Hsu et al., 2014). At the completion of anagen, catagen begins, which is characterized by apoptosis of the lower portion of the HF leading to its subsequent regression and return to the quiescent telogen phase (Gonzales and Fuchs 2017). Due to the well characterized regenerative program, the HF represents an excellent model to study the various aspects of stem cell control (Muller-Rover et al., 2001). In the mouse back skin, HF cycling occurs in waves down the back of the mouse starting at regions around the neck and then progressing down the back (Plikus et al., 2008). This observation highlights that beyond the intricate molecular regulation of stem cell control within a HF, there is dynamic regulation and signaling between different HFs.

Epithelial to mesenchymal transition (EMT)

Overview

The transition from epithelial to mesenchymal cells, as well as the reverse (mesenchymal-to-epithelial transition or MET), are highly dynamic processes implicated in various biological processes. EMT is well studied in the context of embryogenesis, organ fibrosis, and cancer metastasis, which highlight the categorical subtypes of EMT (Kalluri and Weinberg 2009). As our understanding of how EMT is regulated expands, it has become clear that EMT exists on a spectrum or continuum with various possible cell states existing between epithelial and mesenchymal phenotypes (Nieto et al., 2016). Cells do not necessarily exist in 'pure' epithelial or mesenchymal states, but instead can be in intermediate cell states (ICS) or hybrid states that possess characteristics of both epithelial and mesenchymal cells (Nieto et al., 2016). Context and tissue specific functions of EMT exist, but a number of key features and phenotypes are shared amongst the different subtypes of EMT (Kalluri and Weinberg 2009; Nieto et al., 2016).

EMT involves the transient reduction and sometimes full loss of adhesion between epithelial cells. Hallmark changes include alterations in cytoskeleton architecture, changes in cell–cell and cell-matrix adhesions, and loss of apical-basal polarities (Lamouille et al., 2014). In the past EMT identification had been focused on the expression of a few markers such as E-cadherin (E-cad); however, as our understanding of EMT has progressed, an expanded view of EMT identification encompasses multiple layers of molecular changes including EMT transcription factors (EMT-TFs) and their gene regulatory networks that govern the transition (Nieto et al., 2016). A number of key EMT-TFs such as Snail1/Slug and Zeb1/2 have been identified in promoting the

mesenchymal phenotype while other TFs such as *Ovol1/2* and *Grhl2* have been shown to suppress the mesenchymal phenotype thus promoting the epithelial phenotype (Nieto et al., 2016; Lamouille et al., 2014). EMT regulation also occurs at the microRNA, long noncoding RNA, chromatin, and post-translational levels (Nieto et al., 2016).

EMT in normal and diseased epithelial tissues

The development and maintenance of epithelial tissues is largely driven by epithelial stem cells (Blanpain and Fuchs 2014). The dynamic activities of these stem cells such as proliferation and differentiation vary depending on the stage of the tissue such as during development, adult regeneration, or in pathological conditions such as cancer (Blanpain and Fuchs 2014). Increasing evidence implicates EMT (and its regulation) as being another cellular dynamic component that can promote stem cell function (Nieto et al., 2016). In general, stem cell function in adult epithelial tissues is largely focused on the homeostatic maintenance of the tissue where cells that are differentiated or lost need to be replaced (Blanpain and Fuchs 2014). In line with the notion that EMT exists in a spectrum of states and degrees, its role can vary depending on the epithelial tissue, stage of development, whether the tissue is undergoing regeneration or repair, and the pathological condition (Nieto et al., 2016). Below I highlight several instances of EMT function and regulation in committed epithelial tissues in different contexts such as normal development, adult regeneration and repair, and briefly discuss in the context of cancer (readers are referred to other comprehensive reviews on this topic, e.g. (Nieto et al., 2016)).

The normal and cancerous mammary epithelium has been utilized as a model to study the potential role and regulation of EMT in epithelial stem cell function. Experiments using immortalized human mammary epithelial cells provided *in vitro* evidence that ectopic expression of EMT-TFs Snail1 and Twist leads to acquisition of stem-like activities (Mani et al., 2008). A positive correlation between heightened EMT gene signature and stem cell fate has also been noted for normal and cancerous mammary epithelial cell types in culture or directly isolated from the human or mouse tissue (Morel et al., 2008; Wang et al., 2014). These data generated much interest in EMT as they suggest a link between EMT and the gain of stem-like features.

Further work in the mammary model *in vivo* found that Snai2 (Slug) is the major EMT-TF expressed in mouse mammary basal cells known to contain multipotent stem cells, and that ectopic expression of Snai2 leads to enhanced stem-like features (Nassour et al., 2012). Moreover, knockout or knockdown of Snai2 compromises mammary epithelial development and/or the ability of primary mammary epithelial cells to regenerate a mammary tree (Nassour et al., 2012; Guo et al., 2012). Zeb1 has also been found to be expressed in normal mouse and human mammary basal cells (Nguyen et al., 2018), with expression particularly enriched in the Procr⁺ stem cell subset (Wang et al., 2014). However, its functional significance remains to be elucidated. Interestingly, using a transgenic mammary tumor model, Snail1- but not Snai2-expressing cells appeared in the early hyperplastic lesions as well as more high-grade carcinomas (Ye et al., 2015). These cells lack E-cad expression and begin to express other EMT-TFs such as Zeb1, suggesting that Snail1 (but not Snai2) is responsible for governing the EMT program in cancer progression (Ye et al., 2015). These observations highlight the notion that different

EMT-TFs can have different, context-specific functions even in the same tissue, and the exact underlying molecular and cellular mechanisms may differ. Thus, I emphasize again the importance to now expand our view of EMT beyond a simple binary, linear or universally identical process with the end goal of generating mesenchymal cells. EMT can be thought of as a historical term that is redirected to describe the diverse and complex variant forms associated with epithelial-mesenchymal plasticity. Specifically, EMT may be considered a navigation through a rugged, highly nonlinear multidimensional landscape of different axes that cumulatively define EMT (Jolly et al., 2017; Saunders and McClay 2014). On this landscape, cell states other than epithelial and mesenchymal cells often exist, exhibiting mixed (or hybrid) features of epithelial and mesenchymal states. Such cell states, termed as intermediate cell states (ICSs) in this paper, may play important roles in regulating transitions between epithelial cells and mesenchymal cells.

Growing evidence also points to the importance of regulating EMT during physiological epithelial development and regeneration. Within the mammary epithelium, suppression of EMT by Elf5 and Ovol2 TFs appears to be an integral component of its normal development and regeneration (Chakrabarti et al., 2012; Watanabe et al., 2014). Loss of Ovol2 in the mammary epithelium results in an up-regulation of a large number of EMT/mesenchymal markers such as vimentin (Vim) and EMT-TFs such as Zeb1, as well as *in vivo* morphological transformation reminiscent of EMT (Watanabe et al., 2014). Importantly, many of these EMT genes are direct targets of Ovol2's transcriptional repressor activity and depletion of Zeb1 rescues the regenerative defect caused by Ovol2 deficiency (Watanabe et al., 2014), underscoring an EMT-centric function of Ovol2 in the mammary gland. Interestingly and adding to the clinical importance of EMT regulation,

incidence of metastasis-free survival increases in breast cancer patients with high levels of *Ovol2* (Watanabe et al., 2014).

Transcriptional inhibition of EMT by *Ovol2* and its homolog, *Ovol1*, is also critically important for normal skin epithelial development during embryogenesis. Loss of both *Ovol2* and *Ovol1* leads to defective epidermal and hair follicle morphogenesis (Lee et al., 2014). Similar to the observations in the mammary gland, loss of *Ovol* leads to up-regulated expression of EMT structural markers and EMT-TFs, as well as EMT-like phenotypes such as reduced adhesion between, and aberrant migration of, embryonic epidermal cells (Lee et al., 2014). In adult skin, loss of *Ovol2* alone results in defective wound healing (Haensel et al., 2018), a process that has been proposed to involve partial EMT of wound peripheral epidermal cells so they can efficiently migrate to close the wound (Nieto et al., 2016; Haensel and Dai 2018; Arnoux et al., 2005). *Ovol2*-deficient epidermal and hair follicle stem cells migrate faster than their normal counterparts, but with significantly reduced directionality (Haensel et al., 2018)—defects that are near-completely rescued when EMT-TF *Zeb1* is simultaneously lost. On the other hand, loss of EMT-TF *Snai2* compromises epidermal migration after wounding, and results in a thin epidermis and transient delay of hair growth during normal development (Arnoux et al., 2005; Shirley et al., 2010; Hudson et al., 2009). Together these data suggest that a delicate balance of EMT regulation exists to maintain both epithelial-like and mesenchymal-like states and this ability to toggle between the two states might be critical for skin epithelial development and regeneration.

The study of EMT in cancer has largely been focused on its role in promoting invasion and metastasis with an involvement in chemoresistance recently demonstrated

(Nieto et al., 2016); however many questions remain unanswered. Conflicting literature exists and the extent of EMT importance in patients' clinical outcomes remains unclear (Nieto et al., 2016). The roles of partial EMT and intermediate states in the context of cancer is still not well understood likely due to the transient nature of these events (Nieto et al., 2016; Chaffer et al., 2016). The variation of different EMT-TFs' expression together with the diverse cell types in the tissues of origin adds to the complexity.

Epidermal wound healing

Overview

The mammalian epidermis is a stratified epithelium with proliferative stem/progenitor cells residing in the basal layer maintaining epidermal homeostasis and fueling repair/regeneration (Gonzales and Fuchs, 2017). Cutaneous wounding presents a unique challenge whereby the epidermis must alter its proliferative, migratory, and differentiating dynamics to re-establish a functional permeability barrier. The overall process of adult wound healing occurs in multiple distinct but overlapping steps (Shaw and Martin 2009; Eming et al., 2014). Almost immediately following wounding, inflammation occurs characterized by a coagulation cascade to prevent any further blood loss through formation of a fibrin clot and recruitment of immune cells to the wound site to eliminate potential infections. Signals from keratinocytes, platelets, and other immune cells trigger major changes in both the epidermis and dermis. Multiple events including fibroblast proliferation and extracellular matrix (ECM) remodeling occur in the dermis with a goal of replacing the fibrin clot with granulation tissue.

Angiogenesis occurs in the wound granulation tissue, presumably due to increased metabolic needs of the repairing tissue. Re-epithelialization is characterized by the migration and proliferation of the epidermal cells over granulation tissue. Multiple distinct populations of epithelial stem cells contribute to re-epithelialization: those in the hair follicle bulge participate in the healing process transiently, whereas those in the interfollicular epidermis and isthmus/junctional zone participate in long term to generate new epidermis (Arwert et al., 2012; Plikus et al., 2012). Simultaneous and important to

the re-epithelialization process is the contraction of the wound, which is aided by fibroblasts and myofibroblasts in the dermis with contractile abilities.

Wound healing ends with a resolution phase, where the two migrating fronts of keratinocytes make contact with one another, halting migration and regenerating a stratified epithelium, and where remodeling and restructuring of the ECM occurs leading to scar formation. With the wound clear of debris and infections, a mass removal of immune cells (and fibroblasts) occurs either by apoptosis or returning to blood vessels. The current review will focus on existing literature that implicates the existence and regulation of a partial EMT in the re-epithelialization process of wound healing.

EMT and cutaneous wound healing

It has been long recognized that epithelial cells possess a range of inherent plasticity including the ability to become mesenchymal cells. The EMT process is known to produce migratory mesenchymal cell types, such as mesoderm and neural crest, during embryogenesis (Thiery et al., 2009). EMT is also extensively studied in cancer, as it is believed to play a crucial role in cancer invasion, metastasis, and chemoresistance (see recent comprehensive reviews on EMT that discuss advances in these areas; Lamouille et al., 2014; Nieto et al., 2016). Originally thought of as a transformation, suggesting a unidirectional and committed switch, EMT is now considered a transition suggesting a transient and reversible process (Lamouille et al., 2014; Nieto et al., 2016). The reverse process of EMT is termed mesenchymal-to-epithelial transition (MET).

During the process of EMT, epithelial cells undergo cytoskeleton rearrangement, lose their cell–cell junctions and apical–basal polarity, change their interaction with the ECM, and acquire mesenchymal features including enhanced motility and invasiveness

(Thiery et al., 2009; Lim and Thiery 2012; Lamouille et al., 2014; Nieto et al., 2016) (Table 1.2). To facilitate such cellular changes, EMting cells alter their gene expression program, such as down-regulating the expression of epithelial junctional components and up-regulating the expression of genes involved in promoting cytoskeletal changes and adhesion to mesenchymal cells (Lamouille et al., 2014) (Table 1.2). The extent of these cellular and molecular changes differs depending on cell/tissue type and on the extent of EMT.

Generally, EMT-related studies have examined the expression of epithelial (i.e., E-cadherin) and mesenchymal (i.e., N-cadherin or vimentin) markers to define the process, whereas definitive experimental evidence for true mesenchymal state as the end point is lacking in numerous cases where the EMT term is used. In such cases, epithelial-to-mesenchymal-like epithelial transition might be a more accurate term, but could generate additional confusion in an already controversial field. Instead, EMT has been most recently described as a “continuum” where metastable epithelial cells can exhibit different states along the EMT spectrum between the epithelial ‘E’ state and mesenchymal ‘M’ state (Nieto et al., 2016). Intermediate states, known as ‘EM’ states where cells exhibit partial E and M features, have been observed both experimentally and in mathematical modeling. Partial EMT has been used to describe several processes in contexts such as development, fibrosis, cancer, and wound healing (Nieto et al., 2016).

EMT “continuum” or partial EMT still suggests mesenchymal state as the obligatory destination of the process if it was to reach completion. An alternative, although purely hypothetical, scenario is that multiple destination states are possible. That said, broadening the underlying definition of EMT would accommodate a wide array of

observed variations of epithelial plasticity in both developmental and pathological contexts.

EMT is induced by a variety of signaling molecules, and is regulated by several transcription factors, microRNAs, as well as epigenetic factors (extensively reviewed in Lamouille et al., 2014). Growth factors and signaling cascades that induce EMT, some in a tissue- and context-dependent manner, include transforming growth factor beta (TGF β), epidermal growth factor (EGF), fibro- blast growth factor (FGF), hepatocyte growth factor (HGF), Wnt, Hedgehog (Hh), and Notch (Table 1.2). Transcriptional regulators include both EMT-promoting transcription factors, such as Snai1 (Snai1), Slug (Snai2), Zeb1, Zeb2, and Twist, and EMT-inhibiting transcription factors, such as Grhl2, Ovol1, and Ovol2 (Nieto et al., 2016) (Table 1.2).

Recently, our lab has shown that loss of Ovol1/Ovol2 results in developing mouse epidermal cells undergoing morphological, behavioral, and molecular changes reminiscent of EMT (Lee et al., 2014). These cells fail to execute a proper epidermal differentiation program, and functional rescue experiments suggest a causal relationship between the EMT-like phenotype and the terminal differentiation defect. This necessity to suppress EMT-like events during epidermal morphogenesis implicates the possible existence of partial EMT in embryonic epidermis. The notion that partial EMT occurs in adult epidermal wound healing to facilitate the migration of epidermal cells during re-epithelialization was proposed in 2005, and has been widely accepted (Arnoux et al., 2005; Nieto et al., 2016). However, whether this notion has received strong experimental support or remains an attractive hypothesis warrants a closer look.

Morphological Changes and Cellular Dynamics During Wound Re-epithelialization

Various organisms have been used as experimental models to elucidate and characterize the morphological and cellular changes that allow for the process of wound re-epithelialization during embryogenesis or adulthood. Variations in mechanisms have been identified and appear to be organism-, developmental stage-, and epithelial tissue-dependent, but collectively add to a better understanding that has the potential to be applied to improving wound healing in humans.

Studies in model organisms such as fly and chick embryos have provided insights into the role of the actin-based machinery in wound closure. Live imaging studies in fly embryos coupled with small GTPase perturbations underscore the formation of a “purse string” by the actin cable to help generate the necessary contractive forces, as well as suggest the existence of redundant mechanisms and highlight the importance of actin-based filopodia and lamellipodia for “kitting” of the epithelial cells at the terminal stages of wound repair (Wood et al., 2002). Interestingly, the “purse string” mechanism seems to be specific to embryonic stages, whereas adult flies have a lamellae-specific mechanism that involves epidermal polyploidization and cell fusion (Razzell et al., 2011; Losick, Fox, and Spradling 2013). Experiments carried out in chick embryos also illustrated how actin cables generate a contractile “purse string” around the wound, as opposed to adult wounds where cells migrate by lamellipodia (Martin and Lewis 1992).

Zebrafish has also been used as a model system for studying cutaneous wound healing, and its healing process in adult skin shares similar steps as that of mammals except for the formation of an external fibrin clot (Richardson et al., 2013). Adult zebrafish heal their wounds with minimal scarring, despite the presence of a strong inflammatory

response. Although the process of re-epithelialization in adult zebrafish has yet to be meticulously dissected, it is worth noting that the rate of re-epithelialization appears to be very rapid (Richardson et al., 2013).

Wound healing in mouse embryos is distinctly different from that in adult animals, particularly in that embryonic wounds heal perfectly without scarring (McCluskey and Martin 1995). Embryonic day 16 is the latest stage where mice can heal without visible scars (Ferguson and O’Kane 2004). A possible explanation for regeneration in embryos vs. scar formation in adults is the absence of inflammation during embryonic wound healing in mice (Redd et al., 2004). This said, recent studies have shown that when wounds are sufficiently large, proper regeneration including the formation of hair follicles can occur in the center of wounds in several mammalian models such mice, rabbits, and even humans (Ito et al., 2007; Plikus et al., 2012; Plikus et al., 2017).

Re-epithelialization During Mammalian Skin Wound Healing

Wound re-epithelialization in adult mammals involves collective migration, proliferation, and differentiation of keratinocytes around and/or within the damaged site (Shaw and Martin 2009). A combination of in vitro and in vivo studies has been used to characterize the re-epithelialization events. The in vitro methods include standard scratch assays with primary keratinocyte or epidermal cell lines. Previous in vivo evidence on wound healing studies in mice had been limited to static histological, immunostaining, and electron microscopic images, limiting our understanding of the spatiotemporal dynamics of cell proliferation and migration during re-epithelialization.

What was clear though is that migration of epidermal cells is restricted to the region that is proximal to the injury site whereas cells distal from the injury site proliferate (Coulombe 1997; Arnoux et al., 2005) (Figure 1.2). A recent study pioneered the use of intravital imaging of wound re-epithelialization in live mice to examine its spatiotemporal cellular dynamics (Park et al., 2017). This work not only re-enforced the accepted notion of spatially separated migratory and proliferative zones, but also discovered the existence of a so-called mixed zone where migration and proliferation co-exist.

Additionally, this work highlights several important points related to epidermal cell migration in the healing wounds: (1) both basal and differentiating suprabasal cells migrate toward the wound in a spatially organized manner, (2) the rate of local migration correlates with the rate of upward differentiation of migrating epidermal cells, (3) cell migration and elongation predict the directionality of cell divisions toward the wound center.

In both in vitro and in vivo experiments, a preparatory phase is found to exist before the onset of migration toward wound center, whereby neighboring keratinocytes are alerted to the trauma and undergo an activation process characterized by molecular, morphological, cytoskeletal, and adhesive changes (Grinnell 1992; Coulombe 1997; Arnoux et al., 2005). Some of these changes resemble those that occur during EMT, leading to the prevailing proposal that wound re-epithelialization is a partial EMT process (Arnoux et al., 2005). Below, I discuss the cellular and molecular changes during re-epithelialization that bear relevance to classical EMT (Table 1.2), focusing primarily on evidence from in vivo studies.

Directly around the wound, cell “ruffling” was initially used to describe the morphological changes at the early stages in human wounds (Odland and Ross 1968). More specifically, cells change their shape from being polarized cuboidal to being more flattened and elongated with extended cytoplasmic projections (Figure 1.2.A and 1.2.B). These cell shape changes are preceded and/or accompanied by alterations in gene expression including up-regulation of hyperproliferation-associated keratin 6 (K6) and K16, retraction of keratin filaments (which normally associates with desmosomes and hemidesmosomes) from the cell periphery, as well as major reorganization of the actin cytoskeletal network (which normally associates with adherens junctions) (Coulombe 1997; Coulombe 2003; Arnoux et al., 2005).

Cell–cell adhesion is altered, characterized by reduced desmosomal adhesion between cells as well as the reduced presence of adherens junction components such as E-cadherin, leading to appearance of intercellular gaps (Coulombe 1997; Arnoux et al., 2005; Garrod et al., 2005; Nunan et al., 2015) (Figure 1.2.B). Failure to down-regulate desmosomal adhesion, as in mice where protein kinase C α is deficient, is associated with delayed wound healing (Thomason et al., 2012). Down-regulation of adherens junctions and tight junctions, but not desmosomes, has been shown to be mediated by ephrin-B-EphB signaling, as epidermal-specific knockout of both ephrin-B1 and ephrin-B2 results in impaired wound closure, characterized by persistent adherens junctions between cells in the migrating front (Nunan et al., 2015).

Cell–matrix adhesion is also altered to facilitate migration from a normally collagen/laminin-rich basement membrane to and through a fibronectin/tenascin-rich provisional matrix of the clot (Shaw and Martin 2009; Nunan et al., 2015) (Figure 1.2.A

and 1.2.B). Specific changes include redistribution of $\alpha 2\beta 1$, $\alpha 3\beta 1$, and $\alpha 6\beta 4$ integrins (receptors for collagen or laminin) on keratinocyte surface, activated expression of $\alpha 5\beta 1$, $\alpha v\beta 6$, $\alpha 9\beta 1$, and $\alpha v\beta 5$ integrin (receptors for fibronectin, tenascin, or vitronectin), as well as increased metalloproteinase activity that facilitates keratinocyte migration by promoting ECM remodeling and hemi- desmosome breakdown (Arnoux et al., 2005).

While reducing epithelial traits is an integral part of keratinocyte activation and migration during wound re-epithelialization and is reminiscent of partial EMT, *in vivo* evidence for gain of mesenchymal features is sparse. Elevated expression of vimentin and fibroblast-specific protein 1 (FSP1) has been noted in the migrating epithelial tongues of acute wounds of thermal burn patients and in hypertrophic scars (Yan et al., 2010). In a recent study, the spatiotemporal profile of keratinocyte migration and proliferation during wound healing in mouse tail was carefully dissected, again showing that these cellular events can be uncoupled (Aragona et al., 2017). Gene expression analysis of the migrating leading edge revealed an enrichment of genes involved in cell migration (e.g., metalloproteinases) and cell adhesion (e.g., protocadherins, $\alpha 5$ -integrin, desmosome, and gap junction proteins). Genes controlling cytoskeleton and actin remodeling (e.g., actin regulators, myosin, and tubulin) are also part of the leading edge molecular signature, consistent with epidermal migration being driven by actin-myosin filaments that generate traction forces and actin polymerization that generates protrusions (Mitchison and Cramer 1993; Shaw and Martin 2009). Of interest, EMT genes were not noted as part of the leading edge signature (Aragona et al., 2017).

The down-regulation of proliferation in migrating epidermal cells of the healing wounds (Arnoux et al., 2005; Aragona et al., 2017; Park et al., 2017) is worth noting, as

an inverse correlation between EMT and cell proliferation has been noted in multiple contexts (Arnoux et al., 2005; Brabletz and Brabletz 2010; Lim and Thiery 2012). This said, EMT has also been suggested to promote cancer stem cell characteristics, which encompass the ability to self-renew and proliferate (Mani et al., 2008; Scheel et al., 2011). As such, complex and even unrelated mechanisms may underlie the observed parallel in proliferative activity between wound re-epithelialization and EMT.

Conceivably, the adhesive and cytoskeletal changes that occur in the leading edge must be kept in check so that migrating epidermal cells are able to eventually resume their full epithelial state (Figure 1.2.C) to execute a terminal differentiation program to regenerate a stratified epithelium. Indeed, E-cadherin returns to normal levels soon after the two migrating fronts meet (Kuwahara et al., 2001). Moreover, the expression of genes within the leading edge signature decreases as wound re-epithelialization progresses, and disappears upon fusion of the two edges whereas proliferation is resumed at the wound center (Aragona et al., 2017). Furthermore, loss of a desmosomal component Perp leads to impaired re-epithelialization due to enhanced keratinocyte migration while proliferation is unaffected (Beaudry et al., 2010). These findings implicate the transient and reversible nature of the molecular/cellular events that occur during wound re-epithelialization. However, a systematic comparison between the reverse events in the neoepidermis and MET has not yet been performed.

EMT Regulators in Cutaneous Wound Healing

Signaling in the wound bed is a complicated and intertwining affair involving epidermal, dermal, and immune cells, as well as both paracrine and autocrine

mechanisms. Platelets and neutrophils represent some of the key initial signaling sources that release factors to activate/recruit fibroblasts and keratinocytes (Shaw and Martin 2009). Important among the complex signaling milieu are EGF, FGF, HGF, keratinocyte growth factor (KGF), and TGF β (Arnoux et al., 2005; Eming et al., 2014) (Table 1.2). While these signaling molecules ultimately all influence the proliferation and/or migration of epidermal keratinocytes around the wound edge, their cellular origins and underlying mechanisms vary and do not necessarily indicate a direct involvement in regulating the EMT-like aspects of keratinocyte activation.

Particularly relevant to the regulation of partial EMT are EGF and TGF β (Figure 1.2.A and 1.2.B). EGF signaling, mediated through EGF receptor (EGFR) and particularly extracellular-signal-regulated kinase 5, is thought to control Slug expression and keratinocyte activation during wound healing (Arnoux et al., 2008). EGFR signaling is enhanced in N-acetylglucosaminyltransferase V transgenic mice, and is associated with EMT-like phenotypes (elevated levels of Snai1, Twist, and N-cadherin; lower level of E-cadherin) and enhanced re-epithelialization (Terao et al., 2011). TGF β signaling is well-known for its EMT-inducing activity in a myriad of tissue, developmental, and cancer contexts (Nieto et al., 2016; Stone et al., 2016). Its role in cutaneous wound healing has been demonstrated by several studies (extensively reviewed in Bielefeld et al., 2013), dating back to as early as the 1980s (Mustoe et al., 1987). However, complicating the interpretation of its net effect on wound re-epithelialization (Arnoux et al., 2005; Nieto et al., 2016; Stone et al., 2016) is the different and even opposite roles of the three TGF β ligand isoforms (TGF β 1, TGF β 2, and TGF β 3), its plethora of actions on multiple cellular

components in the wound bed, including its ability to promote a fibrotic response (TGF β 1) and induce epithelial cell growth arrest (Le et al., 2012; Bielefeld et al., 2013).

Other developmental signaling pathways such as Wnt, Hh, and Notch have also been implicated in wound healing (Bielefeld et al., 2013). A functional involvement of Wnt signaling has been shown for hair follicle regeneration in large wounds (Ito et al., 2007), whereas a specific effect on wound re-epithelialization in vivo remains elusive. Genetic or pharmacological perturbation of Notch signaling compromises wound closure, but the effects appear pleiotropic and are not limited to that on keratinocyte migration (Chigurupati et al., 2007).

EMT-Inducing Transcription Factor in Cutaneous Wound Healing: Slug

Existing evidence supports the in vivo functional involvement of Slug in cutaneous wound healing. Slug belongs to the Snail superfamily of well-conserved zinc finger transcriptional repressors first identified in *Drosophila melanogaster* and shown to induce EMT initiation (Nieto 2002). In the chick, Slug was identified as an important regulator of mesoderm and neural crest formation, two classical developmental processes that require EMT (Nieto et al., 1994). In the mouse, Snail is critical for mesoderm formation and Snai1 null mice die at gastrulation, whereas Slug is not required for mesoderm or neural crest formation (Jiang et al., 1998).

This said, early studies show that Slug overexpression in a rat urinary bladder carcinoma cell line is able to reduce desmosomal association between cells (Savagner et al., 1997), a notion that is later corroborated by other studies in other cell types including keratinocytes (Shirley et al., 2010). Whether Slug is normally expressed in skin epithelia is controversial, but its loss in mice results in a thinner epidermis and transient

delay of hair growth (Shirley et al., 2010). Slug expression is elevated in keratinocytes at the wound margins (Figure 1.2.B) both in vivo and in vitro, and Snai2 null mice display compromised epidermal migration as soon as 72 hr after wounding with cells at leading edge displaying blunted epithelial extensions (Arnoux et al., 2005; Hudson et al., 2009). Moreover, enhanced expression of E-cadherin and K8 is seen at the migrating front tips in these mice, whereas the rate of wound closure does not appear to be affected. Together, these studies portrait a modulatory, but nonessential function of Slug in wound re-epithelialization.

Other Potential In Vivo Regulators of EMT in Cutaneous Wound Healing

In vivo studies have identified other potential regulators of wound re-epithelialization. A recent study reported the co- expression of transcription factor Foxn1 with EMT markers Snai1, MMP9, and N-cadherin during wound re-epithelialization (Gawronska-Kozak et al., 2016). However, evidence for a functional involvement is lacking. Mice deficient in EMT marker vimentin show wound re-epithelialization defects that appear to be associated with defects in keratinocyte migration, decreased molecular features associated with EMT, as well as defects in maturation and stratification of the neoepidermis (Cheng et al., 2016). However, the predominant mode of action seems to involve fibroblasts by means of a paracrine mechanism. The expression of transcription factor Citp2 is activated in keratinocytes upon wounding, and epidermal-specific deletion of Citp2 results in delayed wound healing (Liang et al., 2012). Here defective re-epithelialization stems from delayed proliferation in the epidermis as well as inability of the keratinocytes to suppress E-cadherin expression in the migrating tongues. Lipocalin

2, which when overexpressed can down-regulate E-cadherin expression and up-regulate mesenchymal markers, has been shown to act downstream of transcription factor TCF3 to promote epidermal cell migration and wound healing (Miao et al., 2014). Despite tantalizing clues, the molecular mechanisms underlying the actions of these EMT-inducing factors are not fully understood.

Ovol2

Ovol2 is a known transcriptional repressor of EMT and is a member of the Ovol family of proteins (including Ovol1-3), which are Cys2/His2 zinc finger transcription factors. These transcription factors are evolutionarily conserved with the *Drosophila* homolog being *ovo/svb*, which is necessary for denticle formation, integrating *Wingless* (*Drosophila* Wnt homolog) and *Drosophila* epidermal growth factor receptor signaling (DER) (Payre et al., 1999). In the mouse, ablation of both *Ovol1* and *Ovol2* (double knockout, DKO) leads to defective differentiation during epidermal morphogenesis (Lee et al., 2014). These defects are associated with EMT-like characteristics such as large gaps between epidermal cells as well as presence of mesenchymal markers (Vim and Zeb1) in the basal layer of the epidermis (Lee et al., 2014). Beyond these phenotypes observed in the epidermis, HF development is severely compromised. Interestingly, overexpression of the transcription factor Ovol2 leads to severe phenotypes including premature differentiation and likely reduced numbers of stem/progenitor cells in both the epidermis and the HF. At a molecular level, Ovol2 was found to transcriptionally repress expression of *Zeb1*, a potent EMT-inducer (Lee et al., 2014). Loss of Ovol1 and Ovol2 led to the upregulation of *Zeb1*, and subsequent repression of *Ctnna1* (Lee et al., 2014). Overall this work points to the function of Ovol transcription factors as critical regulators of the epithelial phenotype.

Single cell RNA-Seq and initial studies in the skin epithelia

scRNA-Seq has become a very powerful tool to transcriptionally profile thousands of cells simultaneously from a single input sample. Taking advantage of ability to uniquely barcode all of the different transcripts within a single cell allows for a snapshot of the transcriptome profiles of individual cells. There are a number of different platforms and technologies that vary in number of cells captured, as well as the amount of transcript capture. There have been some initial studies that have utilized scRNA-Seq as a method to better characterize the epidermis (Joost et al., 2018, 2016). The first key study of its kind was a general characterization of the different epithelial components of the skin, including the epidermis and HF. Initial lineage and pseudotemporal analysis was also utilized to show the progression of EpdSCs to the differentiated suprabasal cells (Joost et al., 2016). The next work focused on making key observations during epidermal wound healing, isolating cells of either epidermal (Lgr6-based lineage tracing) or Bu-HFSC (Lgr5-based lineage tracing) identity (Joost et al., 2018). Both Lgr6- and Lgr5-traced cells have alterations in gene expression during wound healing but with dramatic changes associated with the Lgr5-traced cells as they adopt more epidermal-like (Lgr6-like) signatures (Joost et al., 2018). Interestingly, these activated Lgr5 traced cells alter their expression of key receptors likely to better interact with and receive signaling in the wound environment, highlighting the cellular potential and plasticity of Bu-HFSCs (Joost et al., 2018). In both these studies, a microfluidics chip-based approach was used to capture cells, limiting the overall number of cells that were captured and thus the scope of the analysis to epithelial cells. These studies have provided a new perspective in skin biology but a finer resolution of analysis (utilizing more cells) as well as the inclusion of non-

epithelial cell types will move towards a more encapsulating understanding of normal skin epithelial regeneration and repair.

Thesis work

Altogether, the work in this thesis was designed to utilize the adult epidermis and HF as model systems, in order to ask a number of fundamental questions about skin biology. First, I continued work to better understand the role of *Ovol2* but in the context of adult HF regeneration and epidermal wound healing. Here I ask questions regarding the fundamental role of *Ovol2* during both thesis processes but more broadly, I address the role of EMT in the context of these two processes. I show the importance and requirement of *Ovol2* for normal HF regeneration and epidermal repair. During epidermal repair, my findings indicate that migration needs to be intricately modulated beyond simply promoting the migration of epidermal cells. I show that even in circumstances where epidermal keratinocytes adopt more migratory behaviors, this does not necessarily translate to enhanced wound healing (Haensel et al., 2018).

Second, I aimed to broaden our understanding of global changes in molecular and cellular heterogeneity between normal and wounded skin. I use cutting edge scRNA-Seq technologies to effectively characterize the different cell types and molecular changes between these two states. I largely focus on EpdSCs and the dynamic changes that occur between EpdSCs during normal homeostasis and epidermal wound healing. I identify the existence of basal cell heterogeneity, with four key EpdSC populations, three of which are non-proliferative and one proliferative. I show the existence of these different states in situ and that they simultaneously exist in normal skin. Importantly, using computational tools, I show that there is a functional hierarchy among these EpdSCs. This heterogeneity is also present during wound healing and the lineage dynamics appear similar, but the cells exist at different proportions. Together this work takes a multiscale approach with

an ever-increasing resolution, starting at the whole skin level, further investigating EpdSCs.

Figure 1.1: EMT-associated cellular and molecular events during mammalian cutaneous wound re-epithelialization. **A:** Diagram of wound margins shortly after injury. **B:** Diagram showing migrating epidermal fronts. **C:** Diagram of wound neoepidermis at the resolution stage. B, basal cells; S, suprabasal cells; BM, basement membrane (green). TF denotes putative transcription factors that are important for maintenance of epithelial identity and/or resumption of a full epithelial state. Red, green, and purple bars between cells in the basal layer represent tight junctions, adherens junctions, and desmosomes, respectively. Black and orange bars between basal cells and basement membrane represent distinct cell–matrix interactions in wound periphery and migrating front. Solid and dashed arrows originating from the growth factors represent their known and potential roles, respectively, in inducing EMT-like changes of wound keratinocytes. Note that components in the diagrams are not drawn to scale.

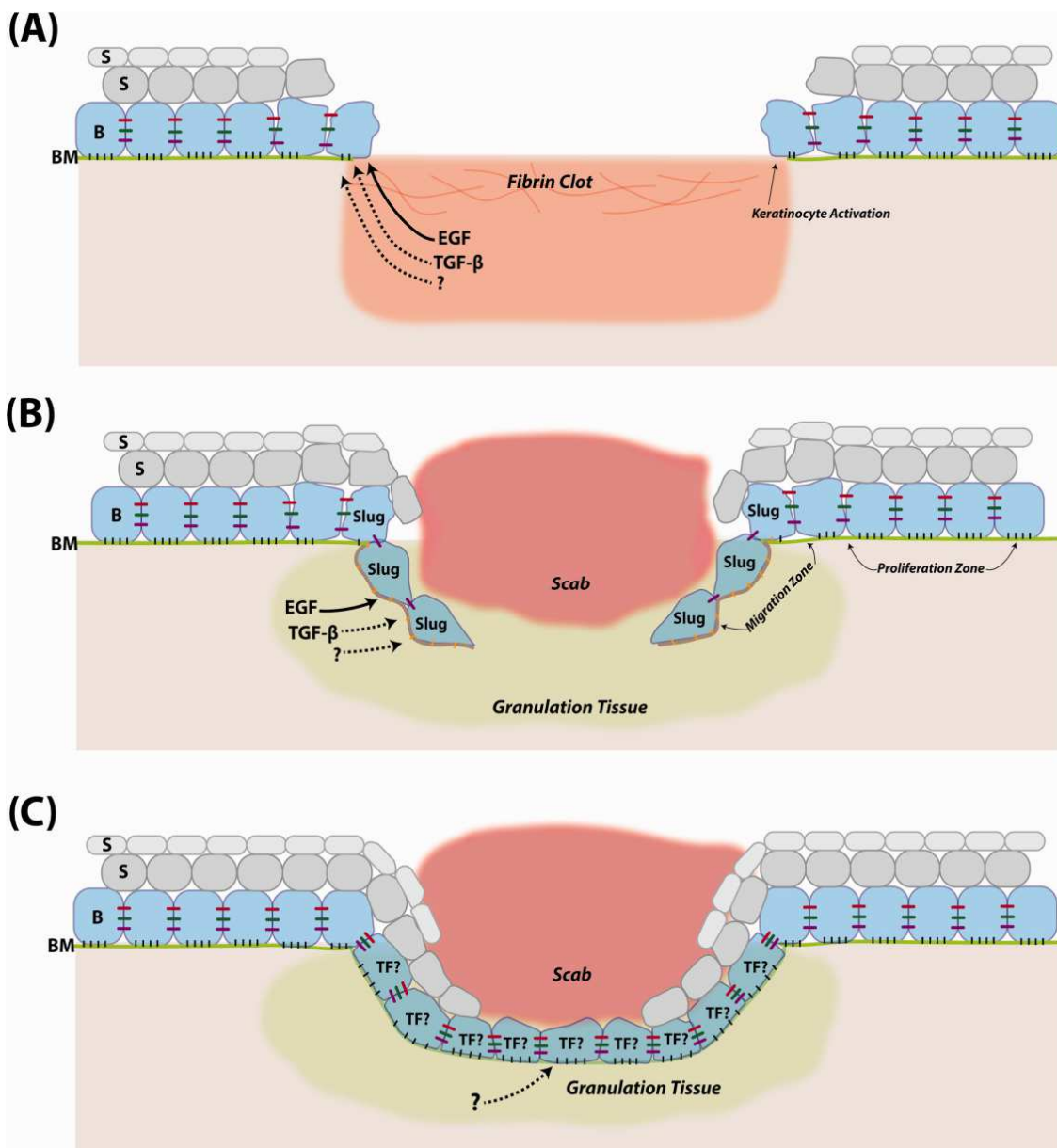


Table 1.2 Comparison of cellular and molecular changes between cutaneous wound re-epithelialization and EMT

TABLE 1. Comparison of Cellular and Molecular Changes Between Cutaneous Wound Re-epithelialization and EMT ^a			
	EMT	Wound re-epithelialization	References
Cell–cell adhesion	Destabilization of adherens junctions; down-regulating E-cadherin; up-regulating N-cadherin and NCAM; dissolution of apical tight junctions and desmosomes	Reduced desmosomal adhesion; reduced E-cadherin	Beaudry et al., 2010 Coulombe, 1997 Garrod et al., 2005 Kuwahara et al., 2001
Cell–matrix adhesion	Down-regulation of $\alpha 6 \beta 4$; requirement for $\alpha 3 \beta 1$; increased $\alpha 5 \beta 1$, $\alpha v \beta 6$, $\alpha 1 \beta 1$ and $\alpha 2 \beta 1$; increased MMPs	Redistribution of $\alpha 2 \beta 1$, $\alpha 3 \beta 1$, and $\alpha 6 \beta 4$; activated expression of $\alpha 5 \beta 1$, $\alpha v \beta 6$, $\alpha 9 \beta 1$, and $\alpha v \beta 5$; increased MMPs	Arnoux et al., 2005 Lamouille et al., 2014
Intermediate filaments	Decreased cytokeratin; increased vimentin	Altered cytokeratin; increased vimentin?	Arnoux et al., 2005 Lamouille et al., 2014
Mode of migration	Single cell migration or collective migration	Collective migration	Arnoux et al., 2005 Lim and Thiery, 2012 Nieto et al., 2016 Park et al., 2017
Growth factors and signaling cascades	TGF- β , EGF, FGF, HGF, Wnt, Hh, Notch	TGF- β , EGF, FGF, HGF, KGF, Wnt, Hh, Notch	Arnoux et al., 2005 Bielefeld et al., 2013 Eming et al., 2014 Lamouille et al., 2014
EMT–transcription factors	(+) Snail, Slug, Zeb1, Zeb2, Twist (–) Grhl2, Ovol1/2	Slug	Arnoux et al., 2005 Nieto et al., 2016 (1) Savagner et al., 1997 Shirley et al., 2010

^a(+) and (–) indicate positive and negative regulation of EMT, respectively.

CHAPTER 2: MATERIALS AND METHODS

Mice

K14-Cre transgenic mice, floxed (f) and null (-) alleles of *Ovol2*, as well as floxed (f) allele of *Zeb1* have been previously described (Andl 2004; Unezaki et al., 2007; Brabletz et al., 2017). ROSA^{mTmG}, ROSA26R, and Nu/J mice are from the Jackson Laboratory (Stock #s 007576, 003474, 002019, respectively). In all mutant analyses, same-sex control littermates were used for comparison. All experiments have been approved and abide by regulatory guidelines of the International Animal Care and Use Committee (IACUC) of the University of California, Irvine.

Morphology and immunostaining

For histological analysis, mouse back skin was shaved, removed, fixed in 4% paraformaldehyde (MP; 150146) in 1× PBS, embedded in paraffin, sectioned, and stained with hematoxylin and eosin (H/E). HF stage identification was based on (Muller-Rover et al., 2001). For whole-mount analysis, mice were shaved, their skin collected and fat carefully removed, and pigmented HFs were visualized from the dermal side. For indirect immunofluorescence, mouse back skin was freshly frozen in OCT (Fisher; 4585), sectioned at 5–8 μ m, and staining was performed using the appropriate antibodies and DAPI (Thermo Fisher; D1306: 1:1,000). The following primary antibodies were used for immunofluorescence: *Ovol2* (Mackay et al., 2006); (rabbit, 1:100), K14 (chicken, 1:1,000; rabbit, 1:1,000; gift of Julie Segre, National Institutes of Health, Bethesda), K15 (Covance, PCK-153P-100, 1:1,000), Ki67 (Cell Signaling, D3B5, 1:1,000), AE13 (Abcam, ab16113, 1:200), Fos (Santa Cruz Biotechnology, sc271243, 1:100), and *Snai2/Slug* (Cell

Signaling, C19G7, 1:100). For b-galactosidase histochemistry, mouse back skin wounds were fixed with 0.5% glutaraldehyde (Sigma; G6257), stained overnight at 37°C with X-gal (Denville; CX3000-3), and counterstained with Nuclear Fast Red (VWR; 1B1369). For epidermal sphere analysis in patch assays, injection sites were isolated and fixed in 4% paraformaldehyde, embedded in paraffin, and sectioned. Antigen retrieval was performed by incubating slides in 0.01 M citrate buffer (pH 6.0) in microwave at full power for 3– 5 min. For ROSA^{mTmG} analysis, mouse back skin wounds were freshly frozen in OCT, sectioned, and then stained with DAPI. For actin staining of cultured Bu-HFSCs, cells were fixed on plate in 4% paraformaldehyde and subsequently stained for K14 and actin (Phalloidin, Invitrogen A12379, 1:250). Thin section images were taken with an inverted fluorescence microscope (Eclipse E600; Nikon) using the Plan-Fluor 10X DIC L 0.30, Plan-Apo-chromat 20× N.A. 0.75, or Plan-Fluor 40× N.A. 0.75 objectives (Nikon) and a camera (RT Slider; Diagnostic Instruments) equipped with SPOT 4.0.9 software (Diagnostic Instruments). Thick section images were taken at room temperature with the Zeiss LSM700 confocal microscope using EC Plan-Neofluar 10×/0.30 objective. Analysis of Phalloidin staining intensity was done using the Plot Profile tool in Fiji.

Wound Healing

Mice were anesthetized using isoflurane (Primal Healthcare; NDC- 66794-017-25), backs shaved, and then 4-mm or 6-mm punches (Integra; 33-34 or 33-36) was used to generate a full-thickness wound on each side of the mouse. For re-epithelialization measurements, splints were fastened surrounding the punch. To generate splints, a 5-mm punch biopsy (Integra; 33–35) was used to generate a hole in 1.5- cm-diameter circular piece of silicone (Life; P18178) and then stitched over the wound. Wound

diameter was measured every 24 h. For expression analysis, 6-mm punch biopsies (Integra; 33– 36) were made, and then, a 12-mm-diameter portion was collected 4 days after wounding. An 8-mm-diameter portion was removed from the center and used as leading edge sample, while the remaining was used as the proliferative zone sample. For ex vivo explant assay, mouse back skin was shaved, removed, fat was scrapped away; remaining hair was removed with brief treatment with Nair and then thoroughly rinsed with 1× PBS. A 4-mm punch biopsy was collected as wound explants, which were then placed onto a well-containing 6 ll Matrigel (BD; 354230) in a 6-well tissue culture dish that was pre-coated with 10 μg/ml fibronectin (EMD Millipore; FC010) for 1 h. For FLIM based wounding experiments, mice were anesthetized using isoflurane, backs shaved, and Nair was applied to the backs of the shaved mice for complete hair removal. A 6-mm punch was used to generate a full-thickness wound on each side of the mouse. Four days after wounding, wound samples containing the wound and un-wounded skin regions surrounding were excised for analysis.

Isolation, culture, and/or infection of NBPKs and Bu-HFSCs

NBPKs were isolated as reported (Lichti, Anders, and Yuspa 2008) with minor modifications. Briefly, epidermal and dermal separation was achieved with an overnight dispase treatment (Stem Cell Technologies; 07913). Keratinocytes were then isolated from separated epidermis using 0.25% trypsin (Sigma; T4799). Dermal cells were isolated from separated dermis using a 0.25% collagenase (Sigma; C9091) digestion at 37°C for 2 h. For growth curve and clonal assays, freshly isolated NBPKs were cultured on tissue culture plastics without fibroblast feeders in low-Ca²⁺ keratinocyte E-media. For gene expression analysis, NBPKs were cultured on mitotically inactivated J2-3T3 fibroblasts in

low- Ca^{2+} keratinocyte E-media. Detailed instructions for J2-3T3 culture and mitotic inactivation can be found in [38]. For growth curve analysis, 10,000 NBPKs were plated per well onto 12-well plates in triplicate. Every 24 h, cells were harvested using 0.1% trypsin and then counted. For clonal growth analysis, NBPKs were plated at a concentration of 1,000 cells/ cm^2 onto 6-cm gridded plates. Two weeks later, a 0.5% crystal violet (Sigma; HT90132) solution made in 1:1 water: methanol was added to the plates to fix and stain the cells. Plates were then rinsed with DI water and imaged. Isolation and subsequent culture of Bu-HFSCs were as reported (Nowak and Fuchs 2009) with minor modifications. Briefly, back skin was cut into ~8 equal pieces and spread dermis side down in 0.25% trypsin and incubated at 37°C for 60 min. Subsequently, epidermis was gently scraped off and then mixed with low- Ca^{2+} keratinocyte E-media, filtered with 70- and 40- μm filters, spun down, and resuspended in low- Ca^{2+} keratinocyte E-media. Adult keratinocytes were stained for CD49f-PE (BD; 555736), CD34-Alexa700 (BD, 560518; clone RAM34), and 7AAD (BD; 559925), followed by sorting using a BD FACSAriaTM Fusion Sorter. Adenoviral infection of Bu-HFSCs was based on (Haensel et al., 2018), using Ade-Cre viruses at a multiplicity of infection of 50 (Vector Biolabs; 1772).

Cell cycle analysis

Cell cycle analysis was performed on Bu-HFSCs after 2 weeks of culture. Cells (Bu-HFSCs and feeders) were removed from plate using 0.1% trypsin and then fixed with cold 70% EtOH for 30 min at 4°C. Cells were washed twice in 1× PBS and then stained with CD49f-FITC (BD; 555735) for 30 min at room temperature in the dark. After two

washes in 1× PBS, cells were stained with FxCycle™ PI/RNase Staining Solution (Life; F10797) for 15 min and then immediately analyzed using ACEANovoCyte™ FlowCytometer.

Patch assay

Patch assay was performed according to published procedures (Zheng et al., 2005, 2016). Briefly, total adult epidermal cells (500,000) from 7- to 8- week-old mice were combined with dermal cells (1,000,000) freshly isolated from newborn C57BL/6J mice. The mixture was subcutaneously injected into 7-week-old Nu/J mice, which were examined 2 weeks later.

Live cell imaging

Wound explants and cells were cultured on either 6-cm or 6-well plates and incubated within a microscope chamber at 37°C with 5% CO₂. Imaging was performed using the Keyence BZ-X700 microscope for 18-h periods with images taken every 15 min. Images were then exported and analyzed in FIJI using the Manual Tracking plugin. Each initial cell position was set to coordinates of (0,0). Step lengths were calculated for each step for each cell track, and turning angles were calculated based on pairs of cell track segments, i.e., ((xt1, xt), (xt, xt+1)). The straightness was defined as D_w/L_w where D_w is the total displacement for a given number of steps (window size), and L_w is the total path length in this window. A window size of 70 steps was used.

RNA isolation, quantitative RT–PCR, and RNA-Seq

For RNA isolation, Trizol (Life; 15596018) was used as per manufacturer's instructions. One microgram of RNA was used to generate cDNA (Applied Biosystems;

4368814) as per manufacturer's instructions. qPCR was performed using a Bio-Rad CFX96 Real-Time System and SsoAdvanced Universal SYBR[®] Green Supermix (Bio-Rad; 172-5271). Primers sequences used for expression analysis are as follows: Ovol2 F: AGCTTCACGACGCCCAAGGC; Ovol2 R: GCCG CAGAAGGTGCACAGGT; Zeb1 F: ACCGCCGTCATTTATCCTGAG; Zeb1 R: CATCTGGTGTTCGTTTTTCATCA; Vim F: GGAGATGCTCCA GAGAGAGG; Vim R: ATTCCACTTTCCGTTCAAGG; Ki67 F: CATCAG CCCATGATTTTGCAAC; Ki67 R: CTGCGAAGAGAGCATCCATC; Cdk1 F: TTCCACGGCGACTCAGAGAT; Cdk1 R: AGCAAATCCAAGCCGTT CTC; Gapdh F: CCTGCCAAGTATGATGAC; Gapdh R: GGAGTTGCT GTTGAAGTC. For RNA-Seq, optimal-quality RNAs (RNA integrity numbers > 9) were used for cDNA library preparation. Full-length cDNA library amplification was performed as previously described (Picelli et al., 2014, 2013). Briefly, 1 ng of total RNA was reverse-transcribed and the resulting cDNA was preamplified for 17 cycles. Tagmentation of cDNA was carried out using the Nextera DNA Sample Preparation Kit (Illumina; FC-121-1031). The Tn6 tagmentation reaction was carried out at 55°C for 5 min and purified using a PCR Purification Kit (Qia- gen; 28104). Adapter-ligated fragments were amplified using limited cycle enrichment PCR with Nextera barcodes for seven continuous cycles. The resulting libraries were purified using AMPure XP beads (Beckman Coulter; A63880) and were multiplexed and sequenced as paired end on a HiSeq 2500 Illumina sequencing platform. Sequencing reads were mapped to the mm9 mouse genome using BowTie2 (Langmead and Salzberg 2012), and splice junctions between exons were mapped using Tophat2 (Kim et al., 2013). Analysis of differential gene expression was accomplished using CuffDiff (Trapnell et al., 2013). Differentially expressed genes were used for GO analysis.

Gene FPKM values were used for downstream analysis that included GSEA (Subramanian et al., 2005).

Single-cell isolation for scRNA-Seq

For un-wounded back skin, mice were shaved, skin removed, fat scrapped off, and then skin was minced into pieces less than 1 mm in diameter. For wounded back skin, skin was removed, large pieces of fat attached to underside of wound were carefully removed, a 10-mm punch (Acuderm; 0413) was then used to punch out both off the wounds (capturing the wound and a portion of un-wounded skin adjacent to the wound). The wounds were then minced into pieces less than 1 mm in diameter. For digestion, the minced samples were placed in 15-mL conical tubes and digested with 10 mL of collagenase mix (0.25% collagenase (Sigma; C9091), 0.01M HEPES (Fisher; BP310), 0.001M Sodium Pyruvate (Fisher; BP356), and 0.1 mg/mL DNase (Sigma; DN25)). Samples are incubated at 37 °C for 2 hours with rotation. Samples are then filtered with 70-µm and 40-µm filters, spun down, and resuspended in 2% FBS. Cells were stained with SytoxBlue (Thermo Fisher; S34857) as per manufacture instructions before sorting.

Single cell library generation

Flow cytometry sorted cells were washed in a PBS with 0.04% BSA solution and resuspended to a concentration of approximately 1,000 cell/µL. Library generation were performed following the Chromium Single Cell 3' Reagents Kits v2 User Guide: CG00052 Rev B. Targeting 10,000 cells per sample for capture. Each library was sequenced on the Illumina HiSeq4000 platform to achieve an average of approximately 50,000 reads per cell.

Processing and clustering analysis of scRNAseq data

FASTQ files were aligned utilizing 10x Genomics Cell Ranger 2.1.0. Each library was aligned to an indexed mm10 genome using Cell Ranger Count. Cell Ranger Aggr function was used to normalize the number of mapped reads per cells across the libraries. For downstream analyses, low-quality cells were further removed. Clustering of cells was performed using the Seurat R package (Satija et al., 2015). Briefly, initial bulk samples containing single cell data matrices were column-normalized and log-transformed. Quality control parameters were used to filter cells with 200-5000 genes with a percent.mito under 10%. Replicates for UW and WO samples were merged and then corrected using the MultiCCA function. To identify cell clusters, principle component analysis (PCA) was first performed and the top 10 PCs with a resolution = 0.6 were used to obtaining 15 and 14 clusters for the UW and WO samples respectively. For subclustering of epithelial cells, we first identified epithelial clusters in each total UW or WO replicate using the top 10 PCs with resolution = 0.6 and then subsetted out the appropriate epithelial clusters. These subsetted epithelial replicates clusters were then merged using MultiCCA function again using 10 PCs with resolution = 0.6. For the subclustering analysis of basal cells in UW and WO, we performed batch correction using the Bayesian-based method ComBat from the sva R package. The corrected data were used for further clustering analysis. Briefly, for UW samples, the top 23 PCs were used for clustering and 3 subclusters were obtained with resolution = 0.8. For WO samples, the top 26 PCs were used and 3 subclusters were obtained with resolution = 0.3. Marker genes were determined with $p\text{-value} < 0.01$ and $\log(\text{fold-change}) > 0.25$ by performing differential gene expression analysis between the clusters using Wilcoxon rank sum test. To present high dimensional data in two-

dimensional space, we performed t-SNE analysis using the results of PCA with significant PCs as input.

Gene Scoring

For gene scoring, a number of gene sets were acquired from the MSigDB database as well as some were homemade from published literature (Cheung and Rando 2013; Aragona et al., 2017). The function `AddModuleScore` was then used to score various cell clusters. The gene sets are listed in Supplemental Figure 8.

Random forest classifier

The function `ClassifyCells` was used with the UW basal cells as the training matrix.

Pseudotemporal ordering analysis

We performed pseudotemporal ordering of all epidermal cells (including proliferating and non-proliferating basal cells, and spinous cells) using two methods `scEpath` (Jin et al., 2018) and `Monocle 2` (Qiu et al., 2017). One of the unique features of our proposed method `scEpath` is that it can quantify the energy landscape using a measure 'single-cell energy (`scEnergy`)', which quantitatively measures developmental potency of single cells. Compared to the differentiated cells, the cycling stem cells exhibit higher `scEnergy` (Jin et al., 2018). In contrast to cycling stem cells, we found that quiescent stem cells exhibit lower `scEnergy`, as we shown that the bulge cells, which are quiescent stem cells, exhibit lower `scEnergy` compared to the spinous cells in our single cell data (Figure S4H). Thus, we can determine the initial state of pseudotemporal

ordering based on the calculated scEnergy. After inferring the lineage relationships between cell states based on the transition probabilities, scEpath also identifies pseudotime-dependent genes. To analyze pseudotime-dependent TFs, we used genes that are annotated in the Animal Transcription Factor Database (AnimalTFDB 2.0). We performed pseudotemporal ordering based on batch corrected data. Batch correction was performed for both UW and WO samples using Combat. The corrected data was used as an input for dimension reduction using PCA, followed by Uniform Manifold Approximation and Projection (UMAP). scEpath then infers the cell lineages based on the UMAP space. For Monocle 2 analysis, batch effects information was passed into the `residualModelFormulaStr` option in “`reduceDimension`” function. We also performed pseudotemporal ordering based on un-batch-corrected data, which showed similar results with those observed in batch-corrected data.

RNA velocity analysis

RNA velocity was calculated based on the spliced and unspliced count as previously reported (La Manno et al., 2018). Only cells that were part of the pseudotemporal ordering were considered in analyses. We used the standard R pipeline of `velocyto` with default settings to perform RNA velocity analysis. *La Manno et al., 2018* used a simple linear model to relate abundance of pre-mRNA $U(t)$ with abundance of mature mRNA $S(t)$ as:

$$\begin{cases} \frac{dU}{dt} = \alpha - \beta \cdot U(t) \\ \frac{dS}{dt} = \beta \cdot U(t) - \gamma S(t) \end{cases}$$

In this model, mRNA abundance over time (represented as dS/dt) is the velocity of gene expression. The molecular regulatory mechanisms between pre-mRNA and mature mRNA are complicated, we thus proposed a nonlinear RNA velocity by modeling the nonlinear dynamics based on Michaelis–Menten kinetics. The nonlinear RNA velocity model is formulated as

$$\begin{cases} \frac{dU}{dt} = \alpha - \beta \cdot U(t) \\ \frac{dS}{dt} = \beta \cdot \frac{U^n}{K^n + U^n} - \gamma S(t) \end{cases}$$

Here n is the Hill coefficient, describing cooperativity. K is a constant. We set n and K to be 1 and 0.5 in all the analyses.

In both linear and nonlinear RNA velocity analysis, RNA velocity was estimated using gene-relative model with k -nearest neighbor cell pooling ($k = 30$). Velocity fields were then projected onto the UMAP space or the low-dimensional space produced by Monocle 2. Parameter n sight, which defines the size of the neighborhood used for projecting the velocity, was 500.

Fluorescence lifetime imaging (FLIM) and data analysis

Freshly excised skin was placed in a glass bottom microwell dish (MatTek Corporation; PG-35g-1.5-14-C) and imaging was performed using a 63X Oil 1.4NA lens (Zeiss,) on a Zeiss LSM 880 microscope coupled to a Ti:Sapphire laser system (Spectra Physics, Santa Clara CA, USA, Mai Tai HP). External hybrid photomultiplier tubes (Becker&Hickl; HPM-100-40) and ISS A320 FastFLIM system (ISS, Urbana-Champaign, Illinois) were used for Phasor Fluorescence Lifetime Imaging Microscopy (Colyer et al., 2008; Stringari et al., 2015; Digman et al., 2008). A 690 nm internal dichroic filter (Zeiss)

was used to separate the fluorescence emission from the laser excitation. The fluorescence emission was reflected to onto a 495LP dichroic mirror and subsequently a 460/80 nm bandpass filter (Semrock; FF02-460/80-25) before the external detector to filter the NADH fluorescence emission. Images were acquired using unidirectional scan, 16.38 us pixel dwell time, 256 x 256 pixels per frame, and 58.67um field of view. All images were acquired within 1.5 hours of animal death.

The phasor plot method provides a fit-free, unbiased way of analyzing FLIM data quantitatively. FlimBox, developed by the Laboratory for Fluorescence Dynamics at UC Irvine, records the photon counts per pixel in a number of cross-correlation phase bins called the phase histogram used for the Digital Frequency Domain FLIM method. The phase histogram is processed by the fast Fourier transform to produce the phase delay ϕ and modulation ratio m of the emission relative to the excitation from which the G and S coordinates calculated at each pixel of the image are represented in the phasor plot.

$$G(\omega) = m(\omega) \cdot \cos(\phi), S(\omega) = m(\omega) \cdot \sin(\phi)$$

Data analysis was performed with Globals for Images (SIMFCS 4.0) software developed at the Laboratory for Fluorescence Dynamics. We used coumarin 6 (Sigma-Aldrich; 546283), with known lifetime of 2.5ns, for calibration of the instrument response function.

Quantification of the average NADH phasor per region of interest was calculated using the built-in masking feature in SimFCS 4.0. This masking feature averages the lifetime (τ) of all pixels included within a designated region of interest (ROI). SimFCS converts G and S coordinates of the phasor plot into the fraction of bound by calculating the distance of the ROI average τ to the theoretical lifetime τ of bound NADH ($\tau = 3.4$ ns),

divided by the total distance between free NADH ($\tau = 0.4$ ns) and bound NADH. An ROI within the boundary of each cell demarked by *K14-Cre;ROSA^{mTmG}* was drawn to estimate the free/bound NADH ratio for each cell within a field of view for all images. The fraction bound values obtained from SimFCS 4.0 were then converted to free/bound ratio NADH for each ROI as a measure of metabolism based on previous work (Stringari et al., 2015; Cinco et al., 2016; Mah et al., 2018; Stringari et al., 2012; S. M. Kim et al., 2016).

RNAScope

For RNAScope, we utilized the Multiplex Fluorescent v2 system (ACD; 323100). Mouse back skin or wounds were freshly frozen in OCT (Fisher; 4585) and sectioned at 10 μ m. We utilized probes for *Krt14* (ACD; 422521-C3), *Trp63* (ACD; 464591-C2), *Cdkn1a* (ACD; 408551-C1), and *Id1* (ACD; 312221-C3). Sections were fixed at room temperature for 1 hour with 4% paraformaldehyde (Electron Microscopy Sciences; 15715-S), which was diluted from stock with 1x DPBS (Corning Cellgro; 21-031-CM). After fixation, standard RNAScope protocols were used according to manufacturer's instructions. We quantified the fluorescence intensity of the basal cells (*Krt14*⁺ for antibody staining as well as adjacent to the basement membrane or wound bed) in both UW and WO samples. For the UW samples, we simply quantified each basal cell in frame sequentially to obtain relative spatial information. For the WO sample, we measured from the wound margin to the tip of the migrating front.

Gaussian process regression

A Gaussian process regression (GPR) is a non-parametric method to fit observations. We use GPR to visualize the major trends of data by controlling the smoothness of the model. GPR uses kernels to measure similarity between inputs based on their distances. Then, inputs with high similarity should have similar output from the fitted model. We used the implementation of GPR in scikit-learn package (Pedregosa et al., 2011; Rasmussen and Williams 2006). The Matérn kernel is used for similarity measurement and a white noise kernel is included to accommodate noise in the data.

Spatial autocorrelation

We use a commonly used index Moran's I to analyze spatial autocorrelation (the similarity/dissimilarity of a variable in spatial neighbors). The local Moran's I at location j is computed as:

$$I_i = \sum_j w_{ij} (x_i - \bar{x}) (x_j - \bar{x}).$$

The global Moran's I is simply the summation:

$$I = \sum_i I_i.$$

We computed the spatial autocorrelation for our sample with 2-nearest neighbors, in other words,

$$w_{ij} = \begin{cases} 1, & |i - j| = 1 \\ 0, & \text{otherwise.} \end{cases}$$

The sample is regarded as a series of cells aligned in one dimension and $|i - j| = 1$ means cell i and cell j are adjacent.

BASC package (Hopfensitz et al., 2012)

Given a collection of values, BASC method first sorts the values to obtain an initial step function representation. This step function is then iteratively refined until there are only two steps. It can be roughly understood as finding the strongest discontinuity point in data. The R implementation of this package “Binarize” is used with algorithm option B to determine thresholds for binarization of the markers.

Plotting

In the oncoplot, each column is a cell and each row is a marker. A dark box means the marker is observed to be on in the cell. The cells are sorted based on the on/off of the markers to show the mutually exclusive pattern of the markers.

CHAPTER 3: An Ovol2-Zeb1 transcriptional circuit regulates epithelial directional migration and proliferation

Daniel Haensel, Peng Sun, Adam L MacLean, Xianghui Ma, Yuan Zhou, Marc P
Stemmler, Simone Brabletz, Geert Berx, Maksim V Plikus, Qing Nie, Thomas Brabletz,
and Xing Dai; EMBO Reprots 2018

ABSTRACT

Directional migration is inherently important for epithelial tissue regeneration and repair, but how it is precisely controlled and coordinated with cell proliferation is unclear. Here, we report that *Ovol2*, a transcriptional repressor that inhibits epithelial-to-mesenchymal transition (EMT), plays a crucial role in adult skin epithelial regeneration and repair. *Ovol2*-deficient mice show compromised wound healing characterized by aberrant epidermal cell migration and proliferation, as well as delayed anagen progression characterized by defects in hair follicle matrix cell proliferation and subsequent differentiation. Epidermal keratinocytes and bulge hair follicle stem cells (Bu-HFSCs) lacking *Ovol2* fail to expand in culture and display molecular alterations consistent with enhanced EMT and reduced proliferation. Live imaging of wound explants and Bu-HFSCs reveals increased migration speed but reduced directionality, and post-mitotic cell cycle arrest. Remarkably, simultaneous deletion of *Zeb1* encoding an EMT-promoting factor restores directional migration to *Ovol2*-deficient Bu-HFSCs. Taken together, our findings highlight the important function of an *Ovol2*-*Zeb1* EMT-regulatory circuit in controlling the directional migration of epithelial stem and progenitor cells to facilitate adult skin epithelial regeneration and repair.

INTRODUCTION

Directional migration of epithelial cells is an integral component of tissue development, regeneration, and repair (Theveneau and Mayor 2013; Rorth 2009; Friedl and Gilmour 2009). While the cellular and molecular machineries responsible for cell movements are relatively well delineated, little is known about the transcriptional

mechanisms that regulate gene expression in epithelial stem and progenitor cells to ensure their directional and collective migration for efficient regeneration and repair. Moreover, how migration of epithelial stem and progenitor cells is coordinated with their proliferative activity during tissue expansion is unclear.

Mouse skin serves as a leading model to study the molecular and cellular mechanisms that control epithelial stem cell function and tissue regeneration (Hsu et al., 2014). During homeostasis, skin epidermis is maintained by epithelial stem cells in the innermost basal layer, which can either self-renew, or follow an upward path to differentiate into spinous and granular cells of the suprabasal layers culminating in the formation of a protective outer permeability barrier (Hsu et al., 2014). Upon skin injury and integral to the healing process, epidermal cells at the wound margin become activated to re-epithelialize the wound (Eming et al., 2014; Shaw and Martin 2009). Central to re-epithelialization are the collective migration of epidermal basal/spinous cells immediately adjacent the wound and the proliferation of basal cells further out on the wound periphery (Park et al., 2017). Migrating keratinocytes exhibit molecular, morphological, cytoskeletal, and adhesive changes that bear resemblance to those occurring during epithelial-to-mesenchymal transition (EMT) (Haensel and Dai 2018), leading to the prevailing notion that wound re-epithelialization is a partial EMT process (Arnoux et al., 2005). However, to date, the precise role of EMT-regulatory proteins in epidermal cell migration during wound healing remains to be elucidated.

Adult hair follicles (HFs) undergo cycles of regression (catagen), resting (telogen), and growth (anagen) (Schneider et al., 2009). Regeneration of a new HF is fueled by stem cells that reside in the bulge (Bu-HFSCs) and their early progenies in the secondary

hair germ (HG) (Hsu et al., 2014; Ito et al., 2004). During telogen-to-anagen transition, HG cells and Bu-HFSCs become sequentially activated, unleashing a coordinated program of active proliferation and differentiation to generate multiple cell types constituting the new HF (Greco et al., 2009). Tantalizing clues implicate the pro-migratory nature of Bu-HFSCs and their progenies in the HG and outer root sheath. Live cell imaging and lineage tracing have detected Bu-HFSC migration within and out of the niche (Rompolas et al., 2012; Zhang et al., 2009). During wound healing, Bu-HFSCs cells also travel toward the skin surface to transiently participate in repair of the interfollicular epidermis (IFE) (Gonzales and Fuchs 2017; Vagnozzi et al., 2015). HG cells also undergo dynamic movements to support the downward extension of the new HF, and contain a keratin 79-positive subset that becomes specified during early anagen and migrates upwards to initiate hair canal formation (Rompolas et al., 2012; Veniaminova et al., 2013). Furthermore, outer root sheath cells of the lower HF are capable of rapid and long-range migration during anagen progression (Rompolas et al., 2012; Rompolas et al., 2013). It has been reported that Bu-HFSC-specific transcription factor (TF) Sox9 activates other Bu-HFSC-TFs when ectopically expressed in epidermal keratinocytes (Adam et al., 2015) and confers enhanced invasive migration (Ge et al., 2017). However, at present very little is known about the transcriptional mechanisms that regulate Bu-HFSC migration and the importance of such control mechanisms in HF regeneration.

Ovol2, a member of the Ovo family of zinc finger TFs, has recently been identified as a critical EMT-inhibitory factor in developing skin and mammary epithelia (Lee et al., 2014; Watanabe et al., 2014). These studies prompted us to ask whether Ovol2 also regulates epidermal repair and HF regeneration in adult skin, and if yes whether this role

is mechanistically linked to the control of cell migration. We show that epithelia-specific loss of *Ovo/2* results in aberrant wound re-epithelialization, delayed anagen progression, and compromised HF regeneration. We provide *ex vivo* and *in vivo* evidence that *Ovo/2*-deficient epidermal cells and Bu-HFSCs migrate faster than their control counterparts, but with reduced directionality and proliferation. The migratory defects are near-completely rescued by simultaneous deletion of *Zeb1*, which encodes an EMT-inducing TF (Nieto et al., 2016). Together, our findings highlight an important role for EMT-regulatory factors in fine-tuning the migration and proliferation of skin epithelial stem cells to facilitate optimal tissue regeneration and repair.

RESULTS

***Ovo/2*-deficient newborn keratinocytes show compromised colony formation, and altered expression of EMT and cell cycle genes**

To probe a functional requirement for *Ovo/2* in skin, we first examined the *in vitro* behavior of newborn primary keratinocytes (NBPKs) derived from skin epithelia-specific *Ovo/2* knockout (*Ovo/2* SSKO: *K14-Cre*; *Ovo/2*^{fl/-}) mice. Despite lack of a remarkable embryonic epidermal phenotype *in vivo* (Lee et al., 2014), compared with control counterparts, *Ovo/2*-deficient NBPKs grew slower at a high density (Figure 3.1A) and formed fewer colonies at a clonal density (Figure 3.1B). Closer examination of individual colonies over time revealed that *Ovo/2* SSKO cells were capable of initial attachment and divisions, but failed to continuously expand and/or to maintain proper intercellular adhesion (Figures 3.1B and C, Supplemental Figures 3.1A and B).

To seek molecular insights, RNA sequencing (RNA-seq) was performed to examine global gene expression differences between control and *Ovo/2* SSKO NBPKs.

This analysis revealed 748 significantly upregulated and 740 significantly downregulated genes (greater than 2-fold difference, $P < 0.05$) in *Ovo/2*-deficient cells (Figure 3.1D and Supplemental Figure 3.1C). Gene Ontology (GO) analysis of the differentially expressed genes revealed EMT genes to be the most highly enriched, and cell cycle genes to be the most reduced, in *Ovo/2* SSKO NBPKs (Figure 3.1E). Gene Set Enrichment Analysis (GSEA) confirmed enrichment or de-enrichment of these GO-identified gene signatures (Figure 3.1F, Supplemental Figures 3.1D and E). Furthermore, the upregulated expression of select EMT genes, *Zeb1* and *Vim*, as well as the downregulated expression of select cell cycle genes, *Ki67* and *Cdk1*, was validated by RT-qPCR (Figure 3.1G). Together, these data uncover reduced proliferative expansion and increased EMT tendency as two major defects of *Ovo/2*-deficient epidermal cells in culture.

***Ovo/2* is expressed in the proliferative compartments of adult skin epithelia during homeostasis and repair**

Toward examining the *in vivo* function of *Ovo/2*, we determined its expression in adult skin. Indirect immunofluorescence revealed the presence of nuclear *Ovo/2* protein in IFE basal and some suprabasal cells (Figure 3.2A). In HFs, nuclear *Ovo/2* was detected at telogen in cells within the bulge and HG, and at early anagen in the presumptive matrix with the highest expression in cells directly abutting dermal papilla (DP; Figure 3.2B and C). During excisional wound healing, nuclear *Ovo/2* protein was abundant in epidermal cells of the highly proliferative zone just outside the wound margin, but completely absent in the migrating front that is known to be devoid of active proliferation (Park et al., 2017) (Figure 3.2D-I). Mixed nuclear (predominantly in suprabasal cells) and cytoplasmic (predominantly in basal cells) signals were detected in the intermediate regions (Figure

3.2F-H), which is curious and may implicate the possibility of previously undocumented nuclear-cytoplasmic shuttling of Ovol2, a notion that is outside the scope of this work. Consistent with regional protein distribution, *Ovo/2* mRNA expression was higher in the wound proliferative zone than the leading edge (Park et al., 2017) (Figure 3.2J). Overall, these data show that Ovol2 protein is present in stem and progenitor cells of the IFE and HF, with expression seemingly correlating with a more proliferative but less migratory cellular state.

***Ovo/2* is required for efficient wound repair and promotes directional migration of wound epidermal cells**

To investigate the role of Ovol2 in epidermal wound repair, we turned to an excisional wound splinting model (S. A. Park et al., 2014) to minimize myofibroblast-driven contraction and to enable measuring wound closure as a direct consequence of re-epithelialization (Supplemental Figure 3.2A). Compared to littermate controls, *Ovo/2* SSKO mice showed delayed wound closure during a 7-day period. By post-wounding day (PWD) 7, *Ovo/2* SSKO and control wounds were 30 and 15%, respectively, of the original wound area (Figure 3.3A and Supplemental Figure 3.2B). Interestingly, at the histological level on PWD 3, the migrating front in *Ovo/2* SSKO wounds had a significantly longer contour and showed apparently abnormal cellular adhesions compared to control counterparts (Figure 3.3B and C). When epidermal cells were genetically marked (mediated by *K14-Cre*) for β -galactosidase (β -gal) or GFP reporter expression to better visualize the neo-epidermis, it became obvious that the leading edges in *Ovo/2* SSKO mice had multiple spikes, rough edges, branches, and grooves (Figure 3.3C and Supplemental Figure 3.2C). Moreover, some *Ovo/2*-deficient

epidermal cells appeared to have disseminated away from the main body of the leading edges (Figure 3.3C).

Next, we compared cell proliferation in control and *Ovo/2* SSKO wounds. Consistent with previous reports (Park et al., 2017; Aragona et al., 2017) epidermal cells distal to the wound in control mice at PWD 3 exhibited a higher proliferative activity than epidermal cells proximal to the wound (Figure 3.3D). Compared to control mice, significantly reduced numbers of Ki67-positive cells were observed in both wound-distal and wound-proximal regions of the *Ovo/2* SSKO mice (Figure 3.3D and E).

Wound explant outgrowth is an established method to measure *ex vivo* wound epidermal cell migration (Keyes et al., 2016). Analysis of explant cultures of control and *Ovo/2* SSKO wounds revealed decreased overall outgrowth in the latter (Figure 3.3F and G). Live cell imaging analysis shows that even though individual cells from *Ovo/2*-deficient explants migrated greater distances within a given time period (18 h), their directionality was reduced as compared to the controls (Figure 3.3H-J). When the full step length and straightness distributions of the migrating cells were plotted, it was clear that *Ovo/2*-deficient keratinocytes took larger and more variable steps (Figure 3.3K), but with less straight paths (Figure 3.3L). Examination of the distribution of turning angles between steps corroborated the loss of persistence of *Ovo/2*-deficient cells (much lower density near 0 than for control cells; Supplemental Figure 3.2D). Decreased proliferation and aberrant migration of epidermal cells thus underlie the wound healing defect in *Ovo/2* SSKO mice.

Loss of *Ovo/2* compromises HF regeneration and Bu-HFSC expansion

Data in the preceding sections demonstrate a functional involvement of *Ovo/2* in regulating IFE cell proliferation, adhesion, and migration under culturing and wound healing conditions. Previously, we reported that *Ovo/2* overexpression results in hair loss and HF defects characterized by precocious telogen-to-anagen progression (Lee et al., 2014), prompting us to examine a physiological role of *Ovo/2* in HF regeneration during adult hair cycle. Indeed, a mild but reproducible delay in the progression of the first postnatal anagen was observed in *Ovo/2* SSKO mice (Figures 3.4A-C and Supplemental Figure 3.3A). Although Ki67-positive HG cells were observed in *Ovo/2* SSKO mice at P22, the presumptive matrix structures were less developed in the new mutant HFs than control counterparts (Figure 3.4D). Moreover, anagen HFs were generally less elongated in *Ovo/2* SSKO skin, their bulbs were smaller, and their differentiated lineages were poorly represented compared to control counterparts (Figure 3.4A-C and Supplemental Figure 3.3B and C). Even in residual mutant HFs with lengths comparable to control HFs, hair keratin expression was reduced as revealed by AE13 antibody staining (Figure 3.4E). It appears as if the outer root sheath cells are migrating downwards to extend the HF, but the matrix cells are not efficiently dividing and migrating upwards to produce the differentiated progenies. Despite these defects, HFs in *Ovo/2* SSKO mice were able to reach second telogen by P49 just as in the WT (Figure 3.4A) and were able to produce new hair shafts (Supplemental Figure 3.3D). There was no hair loss phenotype, and the epidermal thickness was not affected throughout these stages examined (Supplemental Figure 3.3E). Taken together, our data demonstrate a functional requirement for *Ovo/2* in the timely downgrowth of, and subsequent differentiation within, postnatal HFs.

Next, we asked if Bu-HFSCs are affected by *Ovo/2* loss. The percentage of CD49^{hi}CD34⁺ Bu-HFSCs of total epithelial cells (CD49⁺) was similar between control and *Ovo/2* SSKO mice at P23, but was significantly reduced at P49 (Supplemental Figures 3.3F and G) (C Blanpain et al., 2004). However, even at P23, gene expression differences were already evident, as freshly sorted SSKO Bu-HFSCs exhibited upregulated (more than 10-fold) expression of *Zeb1* but downregulated expression of *Ki67* and *Cdk1* compared to controls (Figure 3.4F). Subsequent functional characterizations focused on Bu-HFSCs isolated at P49, when control and SSKO HFSCs were both in telogen. When plated in culture at a clonal density, control Bu-HFSCs were able to produce colonies that continuously expanded over a period of 2 weeks. In sharp contrast, *Ovo/2*-deficient Bu-HFSCs, while able to form small colonies initially, failed to sustain clonal growth leading to dramatically reduced number and size of the colonies at the end of culture (Figures 3.4G-I and Supplemental Figure 3.4A). Furthermore, the few mutant colonies that reached large sizes exhibited abnormal morphology with enlarged intercellular gaps, increased levels of *Zeb1* and *Vim* mRNAs but reduced level of *Cdk1* mRNA, and a higher frequency of nuclear *Zeb1*-positive cells (Supplemental Figures 3.4B-E). Collectively, these data show that *Ovo/2* is required for maintaining the epithelial state and active expansion of Bu-HFSCs.

To investigate the *in vivo* consequence of defective clonal adhesion and expansion of *Ovo/2*-deficient cells, we turned to “patch” assay, a well-established transplantation model to examine the hair/HF regenerative capacity of isolated skin epithelial cells (Zheng et al., 2005). Control or *Ovo/2* SSKO epidermal cells in single-cell suspension were combined with wild-type newborn dermal cells and subcutaneously

injected into the backs of *Nu/J* mice. Two weeks later, significantly fewer hairs/HFs were observed in patches derived from *Ovo/2* SSKO epidermal cells than the littermate control cells (Figure 3.4J and K). Interestingly, at earlier time points when injected epidermal cells first aggregated and began to proliferate (Zheng et al., 2005), the K14⁺ spheres formed by *Ovo/2* SSKO cells were significantly smaller than those formed by control cells (Figure 3.4L and M). These data demonstrate that in the absence of *Ovo/2*, adult epidermal cells have a reduced capacity to regenerate HFs, which appears to stem from early defects in epithelial sphere formation.

Live cell imaging reveals an intimate link between aberrant migration and defective cell cycle progression of *Ovo/2*-deficient Bu-HFSCs

To probe the potential mechanism of *Ovo/2* deficiency-induced Bu-HFSC clonal expansion defects, we utilized live cell imaging to track individual colonies over time. Freshly sorted control Bu-HFSCs generated colonies after 7 days in culture and cells within these colonies exhibited a remarkably rapid doubling rate leading to a > 2-fold increase in cell number over an 18-h period, whereas the doubling rate of *Ovo/2* SSKO cells was significantly lower (Figure 3.5A). More than 80% of the dividing cells in control colonies rounded up slightly and transiently when undergoing mitosis—a phenomenon previously identified as mitotic cell rounding (Sorce et al., 2015), but they quickly reattached *in situ* after generating two daughter cells (Figures 3.5B and C; type-1 division). Less than 20% of the dividing cells, particularly those that reside in the periphery of the colonies, rose up significantly above the plane of the neighboring cells (Figures 3.5B and C; type-2 division). In stark contrast, the relative numbers of rounded-up cells and type-2 divisions were significantly higher for *Ovo/2*-deficient cells (Figures 3.5B and

C, Supplemental Figure 3.4A). Furthermore, these dividing mutant cells often migrated away from their original positions, failed to reattach, and the two daughter cell nuclei remained connected after an extensive period of time (Figure 3.5C).

The prolonged connection of daughter cell nuclei in *Ovo/2*-deficient colonies led us to wonder whether without *Ovo/2* cell cycle is arrested post-mitosis. Indeed, flow cytometry-mediated cell cycle analysis of actively growing Bu-HFSCs revealed a significantly increased number of G2/M cells accompanied by a decreased number of G1 cells in *Ovo/2* SSKO culture, whereas the percent of S-phase cells was unaffected (Figure 3.5D). As expected (Greco et al., 2009), flow cytometric analysis of freshly isolated Bu-HFSCs from telogen back skin revealed few cycling (G2/M/S phase) cells, and no difference was detected between control and *Ovo/2*-deficient cells (Supplemental Figure 3.4F). These data suggest that during active expansion, *Ovo/2*-deficient Bu-HFSCs cannot efficiently transition from G2/M to G1 phase of the cell cycle.

***Ovo/2* promotes directional migration of Bu-HFSCs through suppressing *Zeb1* expression**

The ability to track Bu-HFSC colonies over time enabled us to monitor the migratory behavior of single cells as colonies are expanding. While control Bu-HFSCs migrated outwards with relatively straight trajectories, *Ovo/2* SSKO cells followed less straight/persistent paths (Figure 3.6A). On average, mutant cells migrated greater overall distances with greater velocities than control cells, but the directionality of migration was severely compromised (Figure 3.6B). Moreover, *Ovo/2*-deficient cells took larger and more variable steps (Figure 3.6C) moved in less straight patterns (Figure 3.6D), and exhibited a decreased frequency of turning angles near 0 indicative of loss of persistence

(Supplemental Figure 3.5A). In keeping with this aberrant migratory behavior, phalloidin staining revealed a higher prevalence of stress fiber type of actin network in *Ovo/2* SSKO colonies than in controls, which displayed predominantly cortical type of actin organization (Figures 3.6E and F). Collectively, these data indicate that *Ovo/2* is required for directional migration of Bu-HFSCs *ex vivo*.

The upregulation of *Zeb1* expression in the absence of *Ovo/2* and a known role for EMT in conferring cell motility (Nieto et al., 2016) led us to ask whether loss of *Zeb1* might normalize the aberrant migratory behavior of *Ovo/2*-deficient Bu-HFSCs. To do this, we generated mice containing floxed alleles of both *Ovo/2* and *Zeb1* and acutely deleted the two genes, singly or in combination, in Bu-HFSCs using Cre-expressing adenoviruses (Ade-Cre; Supplemental Figures 3.5B-E). Distinct from *Ovo/2* SSKO Bu-HFSCs where *Ovo/2* deficiency is chronic, acute *Ovo/2* deletion did not result in any detectable difference in Bu-HFSC expansion (Supplemental Figure 3.5F). Live cell imaging revealed decreased directionality/persistence in the migration of Bu-HFSCs with acute *Ovo/2* deletion similar to that of *Ovo/2* SSKO cells, and that this defect was near-completely rescued by the simultaneous deletion of *Zeb1* (Figures 3.6G-I Supplemental Figure 3.5G). These data provide strong evidence for a key role of the *Ovo/2*-*Zeb1* regulatory axis in controlling the migratory behavior of adult Bu-HFSCs.

DISCUSSION

While our previous work describes the importance of *Ovo/1* and *Ovo/2* TFs in epidermal morphogenesis (Lee et al., 2014), the current study highlights *Ovo/2* as a crucial player in skin epithelial repair and regeneration in adult mice. Most notably, our

findings underscore a key role for the Ovol2-Zeb1 EMT-regulatory circuit in modulating the migratory behavior of skin epithelial cells, specifically by restricting migration speed and conferring optimal directionality.

To date, involvement of a classical EMT TF in mammalian cutaneous wound healing has only been shown for Slug (Snai2), the loss of which leads to compromised migration of epidermal cells at the wound leading edge (Arnoux et al., 2005; Hudson et al., 2009). Very little was known about the molecular mechanisms that keep migrating epidermal cells in check so that they are able to maintain or resume epithelial traits. We now find that Ovol2, likely by virtue of its ability to inhibit the expression of EMT-inducing Zeb1, enables wound epidermal cells to migrate slower but with improved directionality and persistence. Thus, counteracting molecular pathways that normally promote and restrict EMT are both active during epidermal wound healing. Conceivably, EMT-promoting TFs such as Slug and possibly Zeb1 can temporarily and mildly relax epithelial rigidity to initiate and facilitate the migration of epidermal cells around the wound, whereas EMT-inhibitory TFs such as Ovol2 restrict this form of epithelial plasticity to ensure that migration is collective and directional toward the wound center for efficient re-epithelialization to occur.

The molecular regulation of epithelial cell migration during HF regeneration remains an even less charted area. Our data reveal for the first time that EMT-regulatory TFs play critical roles in controlling the migratory behavior of Bu-HFSCs and that HF regeneration is inefficient when such mechanisms go awry. Compared to adult IFE stem cells during normal tissue homeostasis, Bu-HFSCs and their early progenies have to travel much further as they embark on the journey to differentiate into specialized cell

types during HF regeneration, much like wound margin epidermal cells during re-epithelialization. It is tempting to speculate that epithelial plasticity, specifically partial, reversible EMT-like changes in cell adhesion and cytoskeleton, is an integral part of Bu-HFSC/progeny migration that drives the formation of a new HF. Indeed, as the HF extends downwards, the nuclei of HG cells are more separated from each other than those in the bulge, and they realign as the HG cells reach the epithelial-DP interface (Rompolas et al., 2012), implicating dynamic but reversible changes in cell–cell associations. Additional work such as intravital imaging of the *Ovo/2* mutant skin is needed to determine whether and how such dynamic cellular events are affected *in vivo*.

Interestingly, coupled to aberrant cell migration, *Ovo/2*-deficient IFE cells, HF matrix cells, and Bu-HFSCs also display significantly reduced proliferation potential. In particular, the aberrant migration and inefficient reattachment of post-mitotic *Ovo/2*-deficient Bu-HFSCs along with an inability to transition into the next cell cycle (G2/M->G1) provide correlative evidence for a potential mechanistic link between aberrant migration/adhesion and cell proliferation. However, the lack of a proliferation defect in Bu-HFSCs following acute *Ovo/2* deletion precluded us from using our established assay to ask whether simultaneous deletion of *Zeb1* is able to normalize the cell cycle arrest. Along a similar line, we note that while previous studies identified distinct proliferative and migratory epidermal zones in the healing wound, a recent study found a third epidermal region where migration and proliferation co-exist and where tissue expansion peaks (Park et al., 2017). Intriguingly, here migration regulates the directionality of the cell division plane, providing yet another case of coordinated control of epidermal cell migration and proliferation. Molecular and signaling pathways are known to regulate both migration and

proliferation during wound healing (Haensel and Dai 2018). This said, the distinct mode of regulation by *Ovol2* vs. known examples such as in the case of BMP signaling (Lewis et al., 2014) is worth noting. It is also important to note that Bu-HFSCs and epidermal cells are two distinct cell types with unique identities and functions; thus, future work is needed to elucidate the potential differences and similarities in mechanism of *Ovol2* function in these two cell types in *in vivo* settings.

In *Ovol2* SSKO mice, *K14-Cre*-mediated *Ovol2* deletion occurs during embryogenesis (Lee et al., 2014). It is possible that some *Ovol2* deficiency-induced cellular aberrancies take longer time to develop than allowed by the *Ade-Cre* acute deletion system. A context-dependent notion receives further support from our finding that the migratory and proliferative defects of *Ovol2*-deficient IFE cells and Bu-HFSCs appeared much more pronounced when cells were experiencing non-physiological and/or stressful conditions, such as in culture, upon transplantation, or during wound repair. Perhaps under such conditions, microenvironmental cues such as elevated growth factor concentration and immune cell infiltration cause greater epithelial plasticity, thereby creating a higher demand for molecular mechanisms that maintain epithelial traits such as cell–cell and cell–matrix associations during migration.

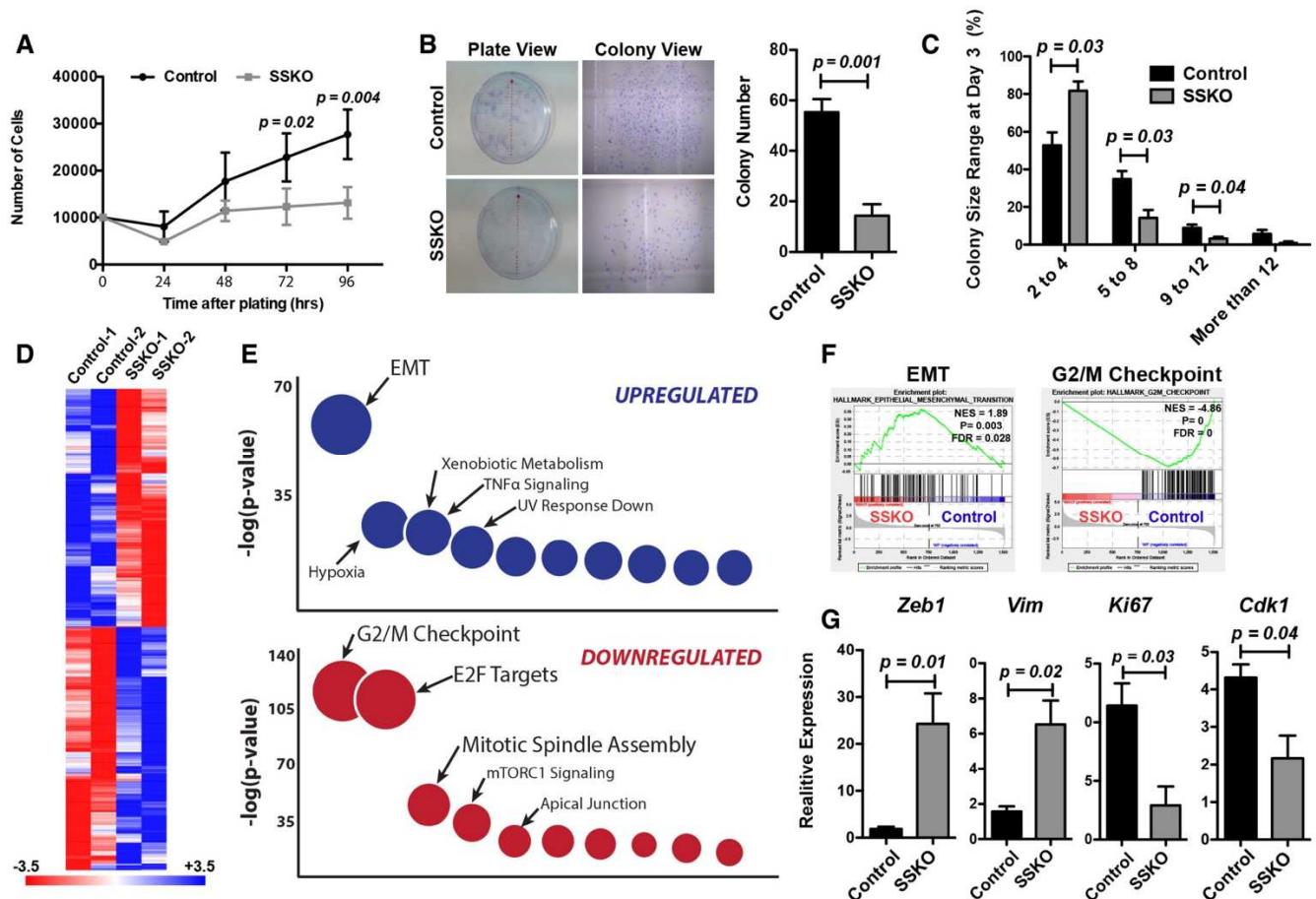
Lack of keratinocyte migration is observed in chronic wounds such as those in diabetic patients and is apparently associated with epidermal hyperproliferation (Eming et al., 2014). Our animal model studies raise the intriguing possibility that aberrantly increased cell migration at the cost of directionality can be accompanied by epidermal hypoproliferation and together they may underlie some non-healing wounds in human patients. As the current treatment strategies emphasize the promotion of epidermal

migration (Eming et al., 2014), caution should be exercised to create an optimal wound healing tissue microenvironment that enables migration but in a persistent and directional manner.

Figure 3.1. Growth and gene expression defects in *Ovo/2*-deficient NBPKs

- Growth curve of cells cultured at high densities ($n = 3$ pairs).
- Results of clonal assays at 14 days after plating. Representative images are shown on the left, and quantification of multiple assays on the right ($n = 3$ pairs).
- Distribution of colony size (i.e., number of cells per colony) at 3 days after plating ($n = 3$ pairs).
- Heat map of genes differentially expressed ($P < 0.05$) in control and *Ovo/2* SSKO NBPKs. Plotted values are \log_{10} (FPKM).
- GO analysis of the top up- or downregulated gene sets.
- GSEA analysis of RNA-seq data. NES, normalized enrichment score. FDR, false discovery rate.
- RT-qPCR of the indicated genes normalized to *Gapdh* ($n = 3$ pairs).

Data information: For statistical analysis in (A), (B), (C), and (G), we used an unpaired two-tailed Student's *t*-test. Error bars in (A), (B), (C), and (G) represent mean \pm SEM.



Supplemental Figure 3.1. Supplemental data on NBPK analysis

- Tracking individual colonies starting at 3 days after plating.
- Fold increase in cell number per colony.
- Linear regression analysis of RNA-Seq replicate samples.
- GSEA analysis of control and *Ovo/2* SSKO NBPKs with the indicated gene sets.
- List of enriched/de-enriched GO terms identified in GSEA.

Data information: Scale bar, 100 μ m in (A). For statistical analysis in (B), we used an unpaired two-tailed Student's *t*-test. Error bars in (B) represent mean \pm SEM.

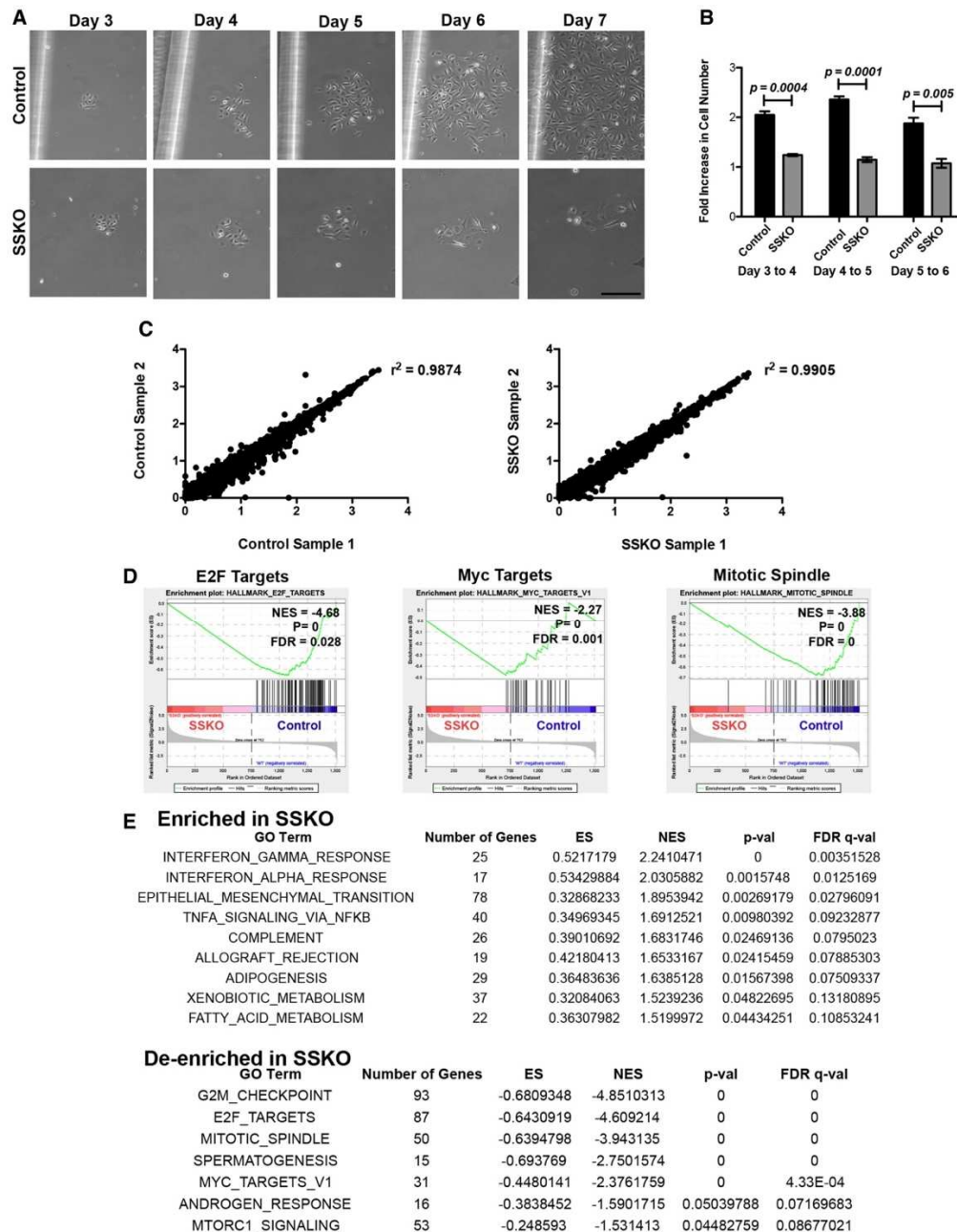
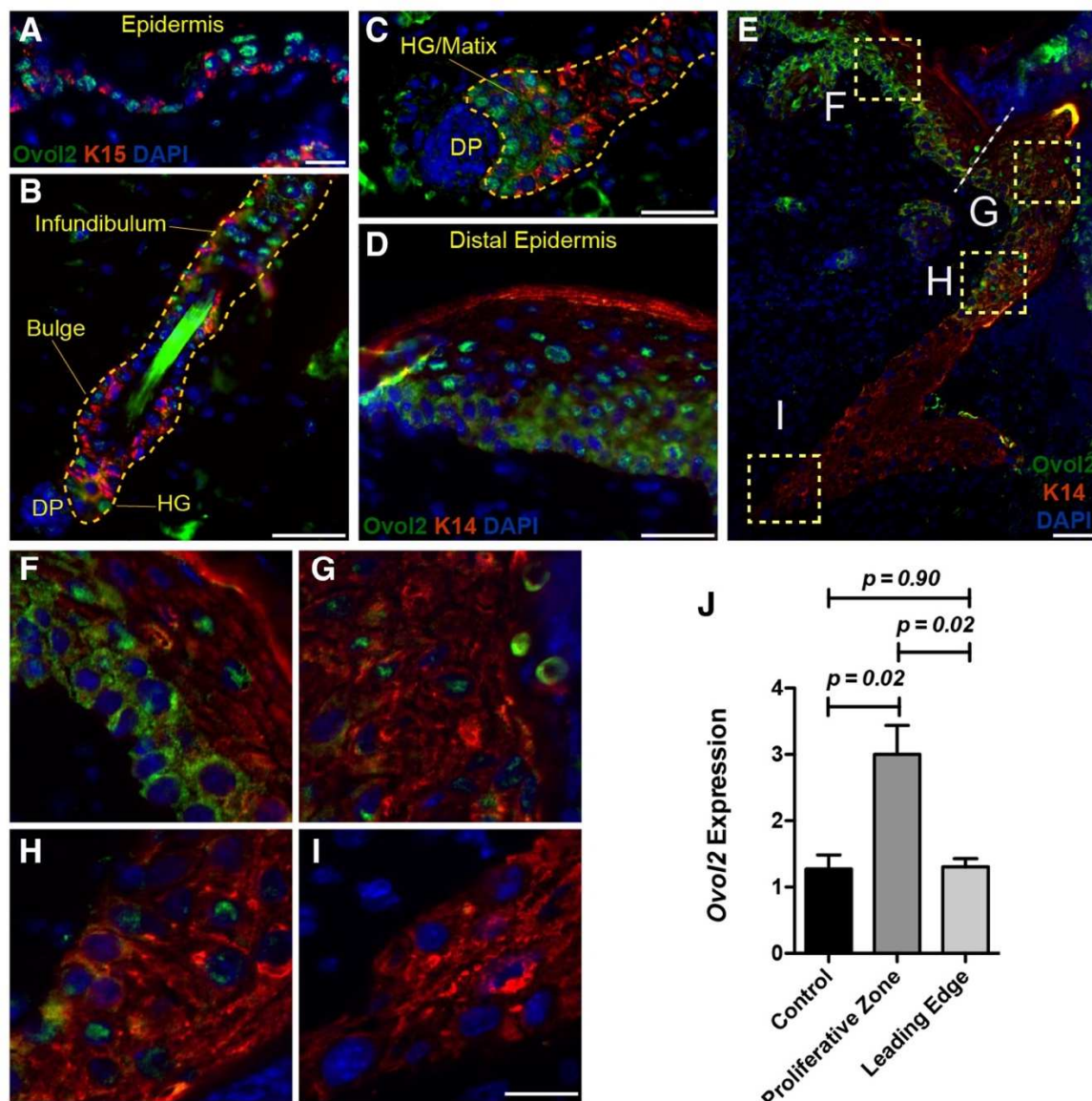


Figure 3.2. Ovol2 expression in normal and wounded adult skin

- A. (A-I) Ovol2 protein expression revealed by indirect immunofluorescence. Enlarged images of the boxed areas in (E) are shown as (F-I) to indicate Ovol2 protein distribution in the intermediate regions (F-H) between the proliferative zone (D) and the migrating front (I). White dashed line in (E) indicates the wound margin. DAPI stains the nuclei.
- B. (J) RT-qPCR analysis of unwounded skin (control) and microdissected wound regions ($n = 3$ mice).

Data information: Scale bar, 50 μm in (A-D and F-I); 100 μm in (E). For statistical analysis in (J), we used an unpaired two-tailed Student's t -test. Error bars in (J) represent mean \pm SEM.



Supplemental Figure 3.2. Supplemental data on wound healing analysis

- Diagram of wound splint model and measurement strategy.
- H/E analysis at 7 days after wounding. Control wounds had completed re-epithelialization and the wound bed had become flush with the epidermis, whereas *Ovo2* SSKO mice had the distinctive “U” shape morphology suggesting a delay in the overall wound healing process.
- Confocal Z-stack of 30- μ m sections from control (*Ovo2^{fl/+};K14-Cre;ROSA^{mTmG}*) and *Ovo2*SSKO (*Ovo2^{fl/-};K14-Cre;ROSA^{mTmG}*) mice at 3 days after wounding.
- Comparison of the distribution of turning angles between steps for cells in control and *Ovo2* SSKO wound explants.

Data information: Scale bar, 500 μ m in (B), 100 μ m in (C)

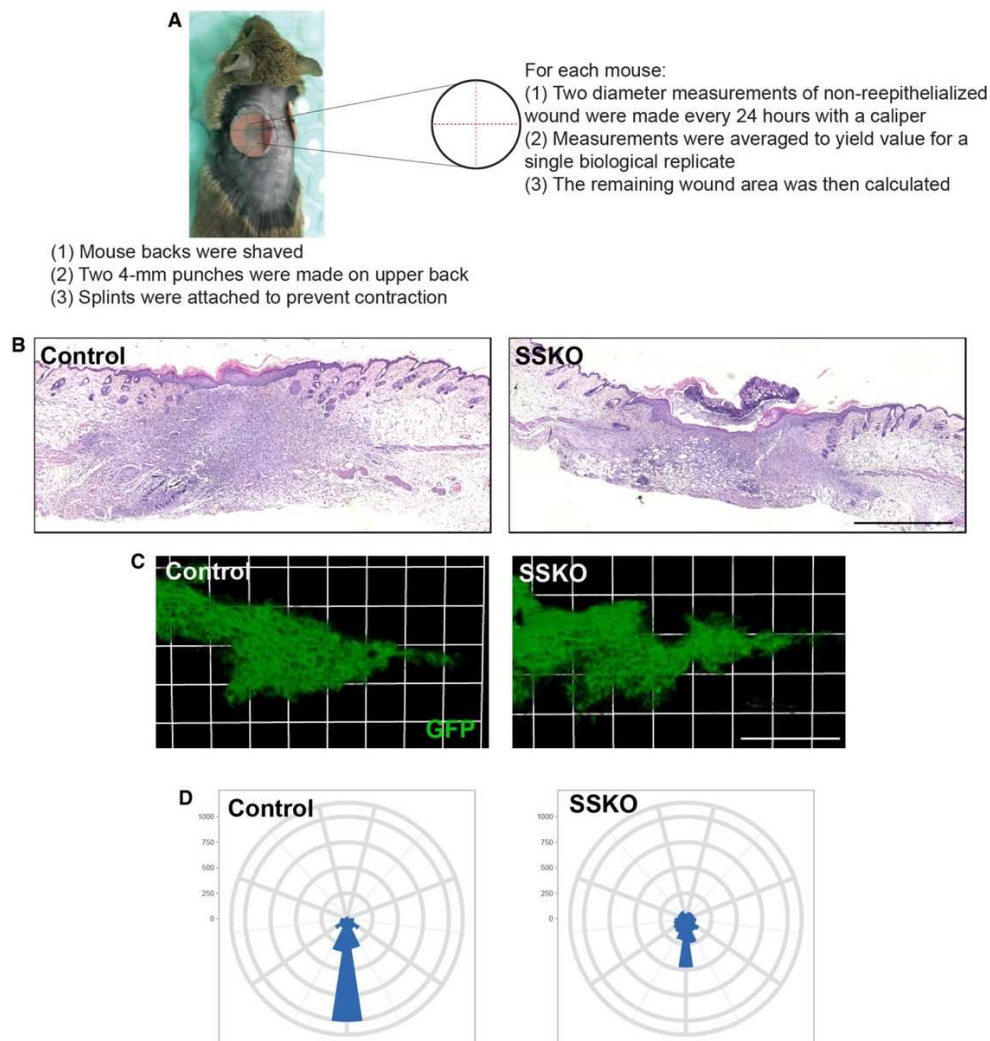


Figure 3.3. *In vivo* and *ex vivo* evidence for skin wound healing defects in *Ovo/2* SSKO mice

- A. Percent of original wound area over 7 days after wounding ($n = 3$ pairs; $*P < 0.05$; $**P < 0.005$).
- B. Length of the neo-epidermis (outer contour of the migrating front up to the wound margin) at PWD 3 ($n = 3$ pairs).
- C. Morphology of the leading edges in control (*Ovo/2*^{fl/+}; *K14-Cre*; *ROSA26R*) and *Ovo/2* SSKO (*Ovo/2*^{fl/-}; *K14-Cre*; *ROSA26R*) wounds. Yellow arrow points to disseminating cells.
- D. Proliferation analysis by Ki67 immunostaining.
- E. Percent Ki67⁺ cells were calculated as the number of Ki67⁺ cells within the neo-epidermis over the total number of DAPI-stained nuclei ($n = 3$ pairs).
- F. Representative wound explants stained with crystal violet.
- G. Quantification of the outgrowth distance of multiple explants from (F) ($n = 3$ pairs).
- H. Movement tracks of individual cells in control and *Ovo/2* SSKO explants over 18 h of live imaging.
- I. (I-L) Quantitative analysis of total distance traveled (I), directionality (J), full step length (K), and straightness distribution (L) of multiple cells in control and SSKO explants ($n = 3$ pairs).

Data information: Scale bar, 100 μm in (E) and (D), 1,000 μm in (F). For statistical analysis in (A), (B), (E), (G), (I), and (J), we used an unpaired two-tailed Student's *t*-test. For statistical analysis in (K) and (L), we used Kolmogorov–Smirnov test with $P = 0.005$ and $P = 0.0001$, respectively. Error bars in (A), (B), (E), (G), (I), and (J) represent mean \pm SEM.

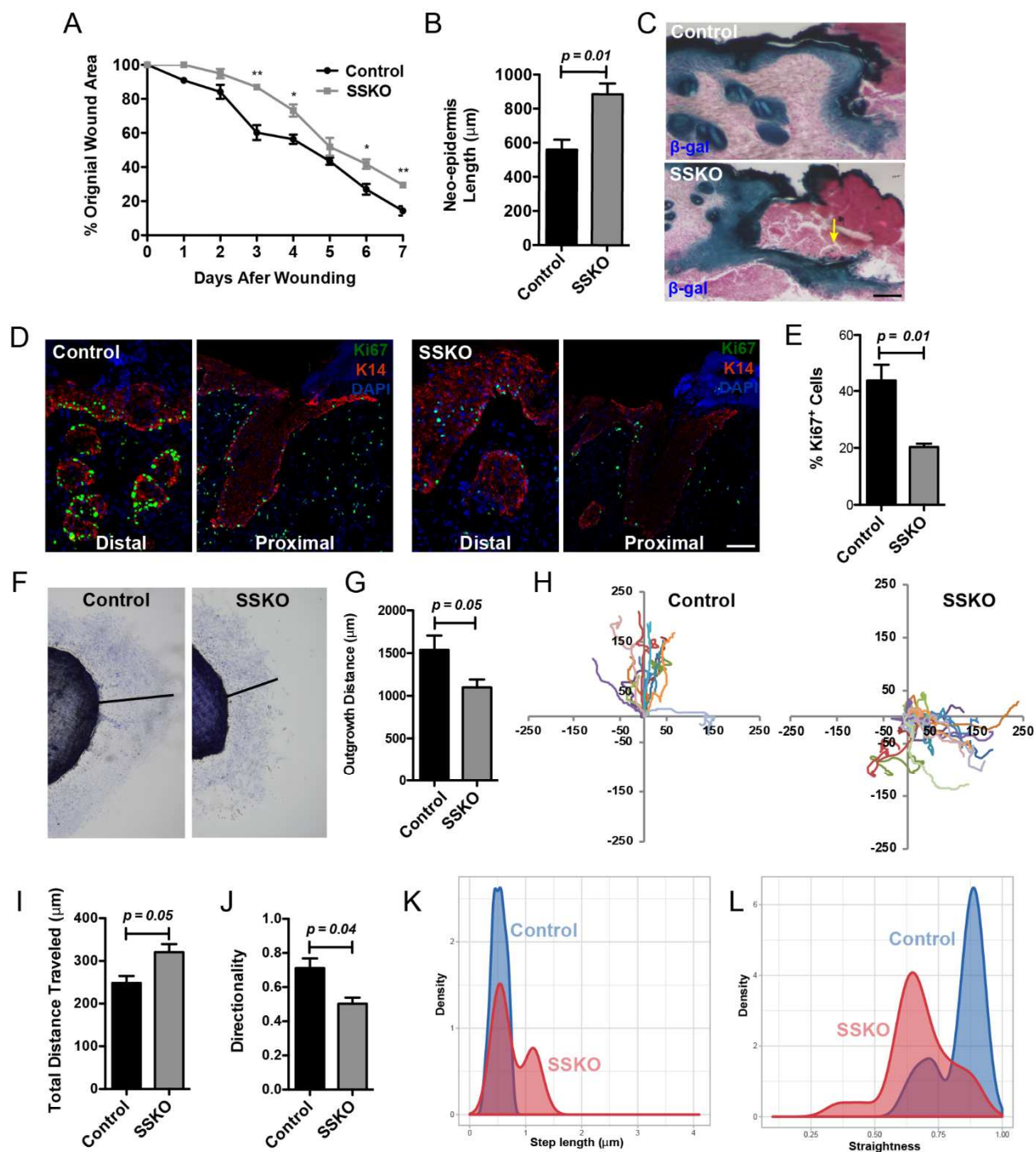
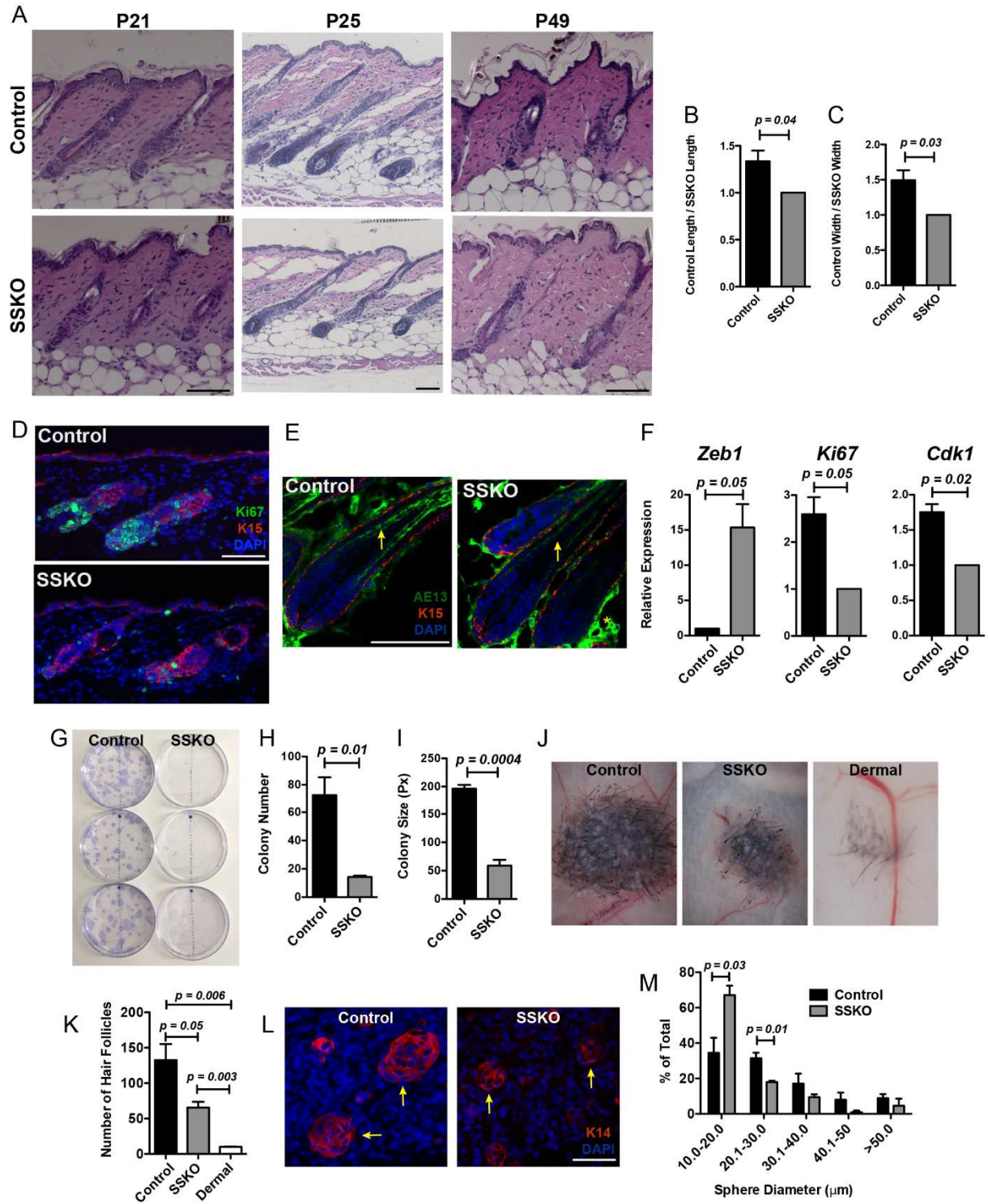


Figure 3.4. *In vivo* and *ex vivo* evidence for *Ovo/2* loss-induced HF defects

- A. H/E analysis of control and *Ovo/2* SSKO skin at the indicated ages.
- B. Fold difference in HF length between control and *Ovo/2* SSKO mice at the ages of P22-P26 ($n = 5$ pairs).
- C. Fold difference in bulb width between control and *Ovo/2* SSKO mice at the ages of P22-P26 ($n = 5$ pairs).
- D. Ki67 immunostaining in control and *Ovo/2* SSKO skin. K15 stains the bulge/HG cells.
- E. AE13 immunostaining. Arrows and “*” indicate specific and background signals, respectively.
- F. RNA expression of the indicated genes normalized to *Gapdh* in freshly sorted P23-Bu-HFSCs ($n = 3$ pairs).
- G. Clonal analysis of control and *Ovo/2* SSKO Bu-HFSCs.
- H. Number of Bu-HFSC colonies from (G) ($n = 3$ pairs).
- I. Average size of Bu-HFSC colonies from (G) ($n = 3$ pairs).
- J. Representative images of patch assay results using control and *Ovo/2* SSKO epidermal cells along with dermal-only control.
- K. Quantification of number of HFs ($n = 3$ pairs; each biological replicate is an average of three injections).
- L. K14 immunostaining of skin from the injection site at 3 days after injection. Arrow points to epidermal spheres.
- M. Quantification of epidermal sphere diameter (three independent experiments using three pairs of control and *Ovo/2* SSKO mice) at 3 days after injection.

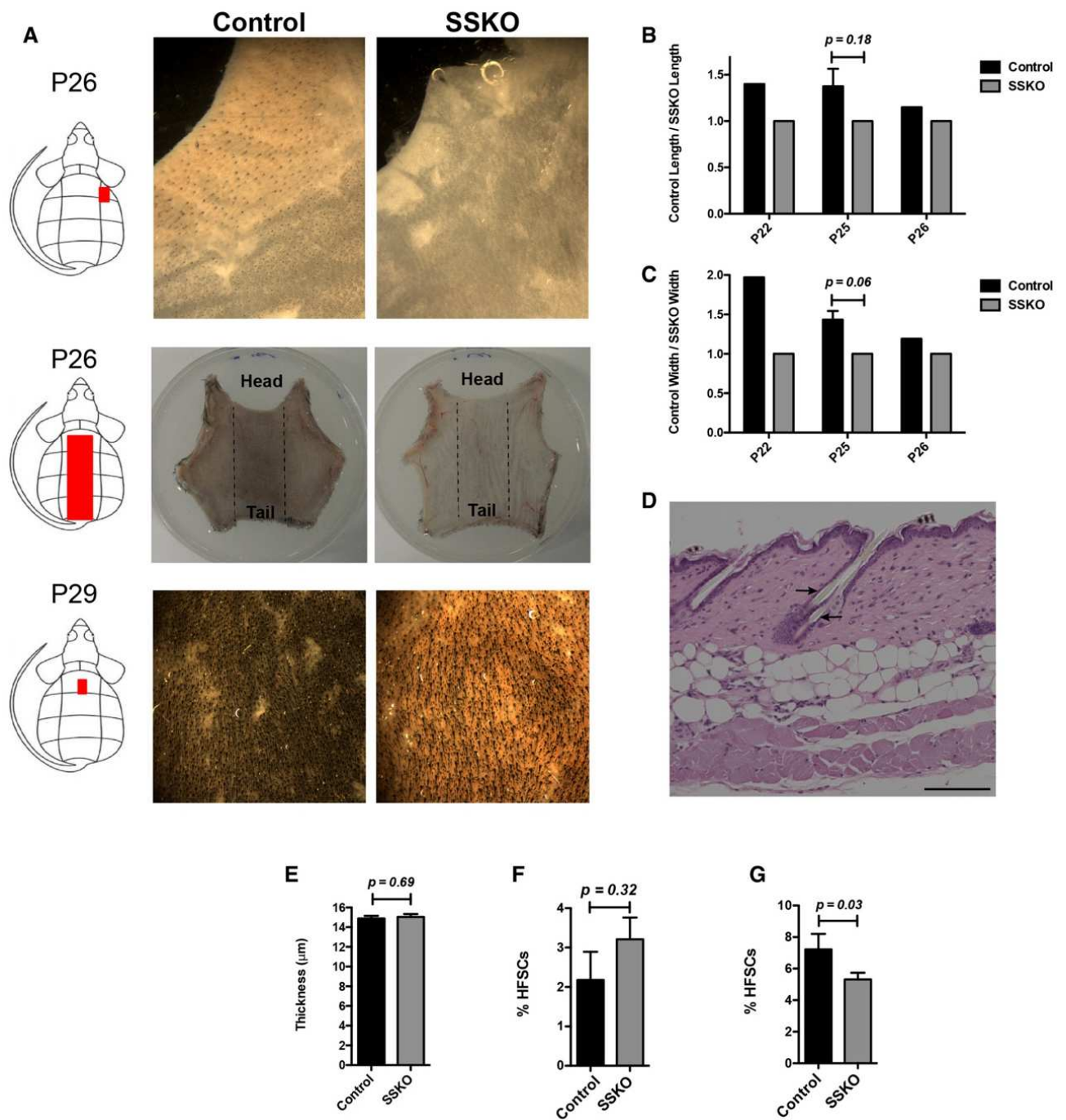
Data information: Scale bar, 50 μm in (A), (D), (E), and (L), 250 μm in (J). For statistical analysis in (B), (C), (H), (I), (K), and (M), we used an unpaired two-tailed Student's *t*-test. For statistical analysis in (F), we used a paired two-tailed Student's *t*-test. Error bars in (B), (C), (F), (H), (I), (K), and (M) represent mean \pm SEM.



Supplemental Figure 3.3. Supplemental data on HF analysis

- A. Whole-mount back skin images of same-sex littermates at different stages of the hair cycle. The particular underside region that is being examined in each row was indicated on the mouse diagrams on the left.
- B. Fold difference in HF length between control and *Ovo/2* SSKO mice at the indicated ages ($n = 1$ pair at P22, 3 pairs at P25, and 1 pair at P26).
- C. Fold difference in bulb width between control and *Ovo/2* SSKO mice at the indicated ages ($n = 1$ pair at P22, 3 pairs at P25, and 1 pair at P26).
- D. H/E analysis of P49 *Ovo/2* SSKO skin indicating new hair shaft formation. Arrows indicate old and new hair shafts from the same follicle.
- E. Epidermal thickness of skin of the indicated genotypes ($n = 6$ pairs: 2 at P21, 2 at P25, and 2 at P49).
- F. Percentage of CD49^{hi}CD34⁺ Bu-HFSC at P23.
- G. Percentage of CD49^{hi}CD34⁺ Bu-HFSC at P49.

Data information: Scale bar, 100 μm in (D). For statistical analysis in (B), (C), (E), (F), and (G), we used an unpaired two-tailed Student's *t*-test. Error bars in (B), (C), (E), (F), and (G) represent mean \pm SEM.



Supplemental Figure 3.4. Supplemental data on Bu-HFSC analysis

- Tracking individual Bu-HFSC colonies from day 7 to day 10 in culture. Yellow dashed lines indicate colony outline at the indicated times, whereas red dashed lines indicate colony outline at day 7.
- High magnification images of single Bu-HFSC colonies at 14 days after plating.
- Expression analysis of the indicated genes in cultured Bu-HFSCs ($n = 3$ pairs).
- Zeb1 immunostaining in control and *Ovo12* SSKO Bu-HFSCs.
- Quantification of percent Zeb1⁺ cells per total cells in each colony ($n = 2$ pairs).
- Cell cycle analysis of P49 Bu-HFSCs freshly sorted from control and *Ovo12* SSKO littermates.

Data information: Scale bar, 100 μ m in (A), (B), and (D). For statistical analysis in (C), we used an unpaired two-tailed Student's *t*-test. Error bars in (C) represent mean \pm SEM.

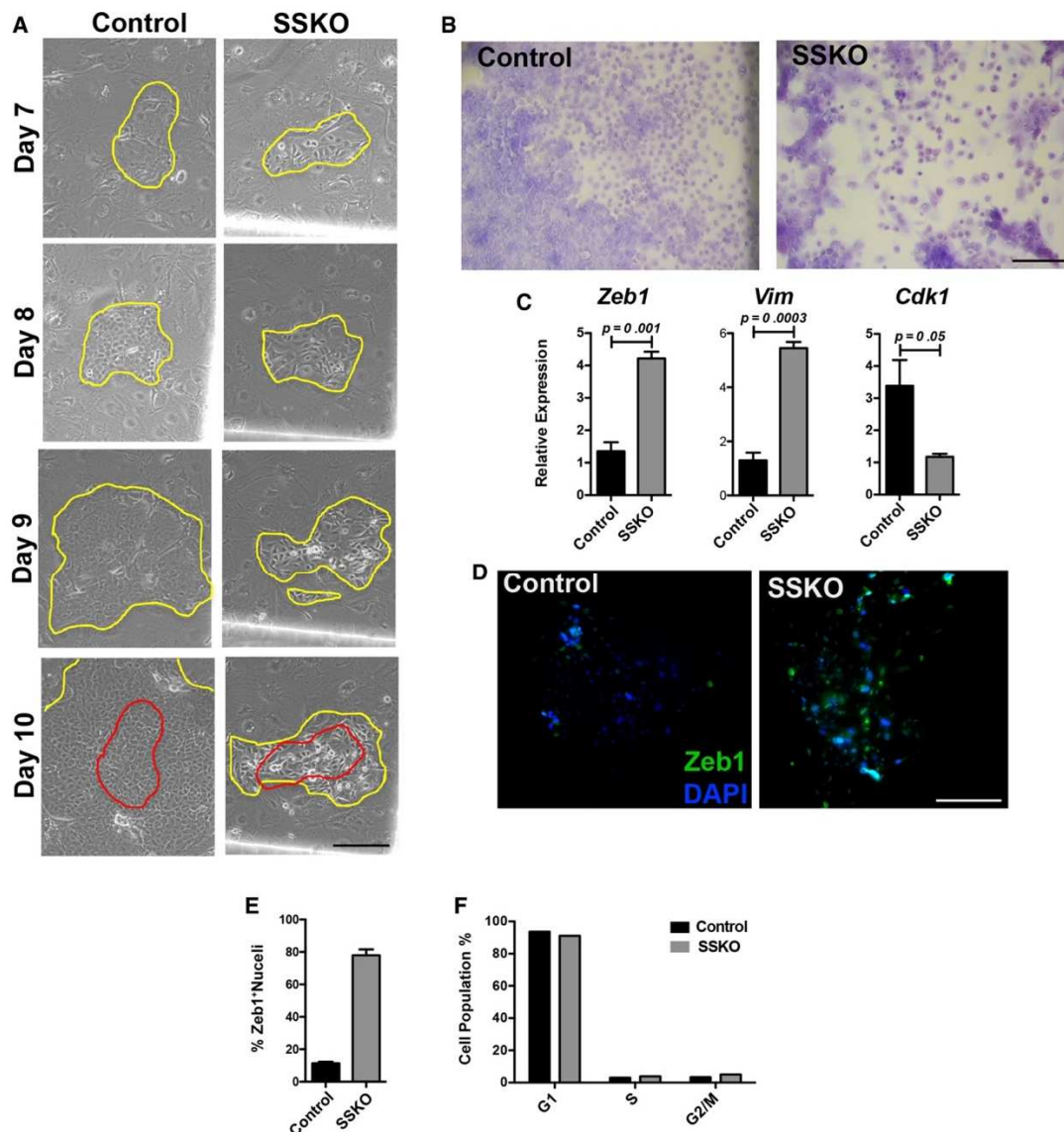


Figure 3.5. *Ovo/2*-deficient Bu-HFSCs display aberrant cell division behavior and arrest in G2/M→G1 transition

- Fold change in cell number per colony in an 18-h period ($n = 3$ pairs; each biological replicate is an average of three different colonies).
- Live imaging reveals an increased frequency of type-II divisions in SSKO culture, as quantified in ($n = 3$ pairs; each biological replicate is an average of three different colonies).
- Representative images from a single live cell imaging experiment. Red and blue arrows in mark two individual cells and their division products during time-lapse.
- Cell cycle analysis of cultured Bu-HFSCs from control and *Ovo/2* SSKO mice ($n = 3$ pairs).

Data information: Scale bar, 100 μm in (E). For statistical analysis in (A), (B), and (D), we used an unpaired two-tailed Student's *t*-test. Error bars in (A), (B), and (D) represent mean \pm SEM.

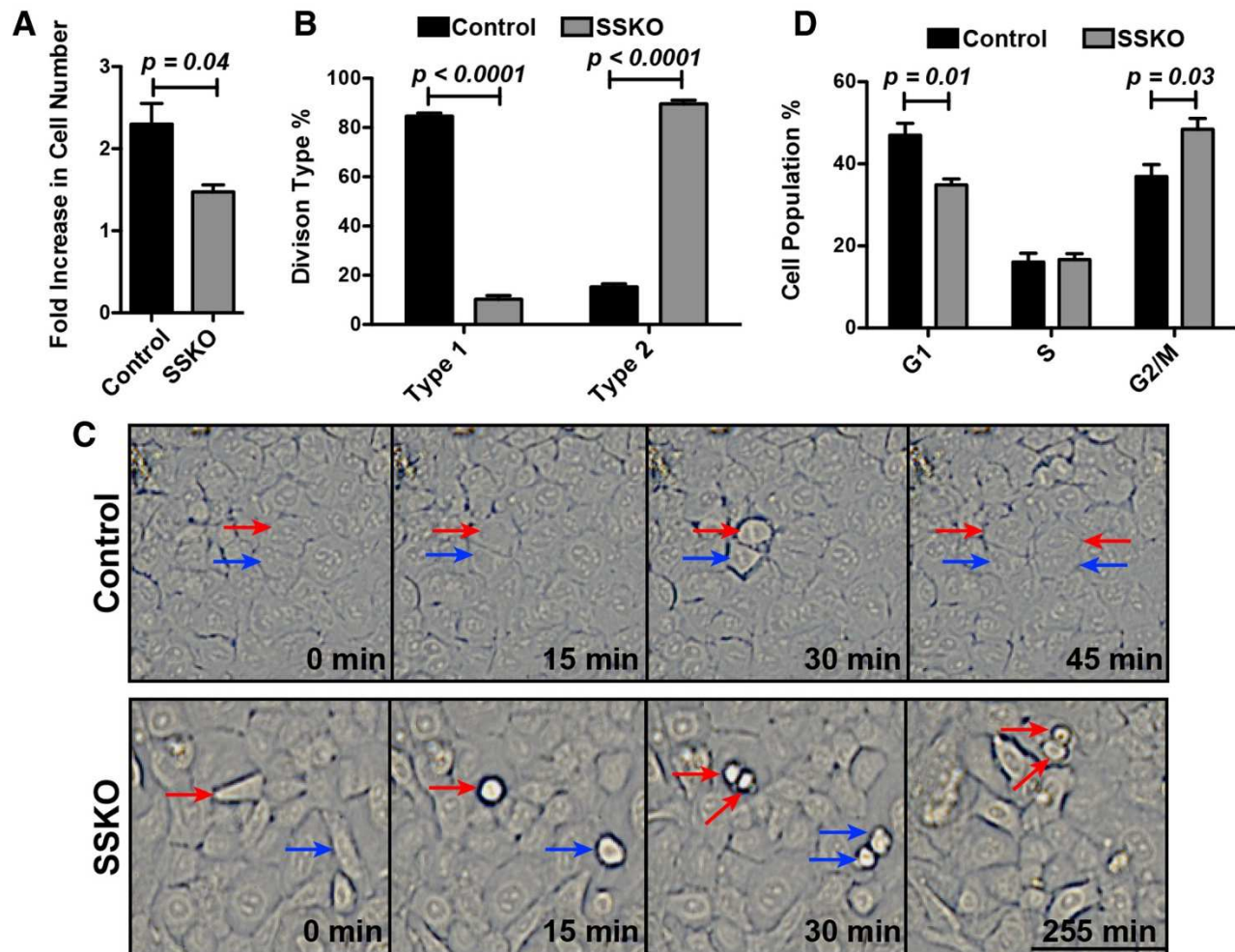
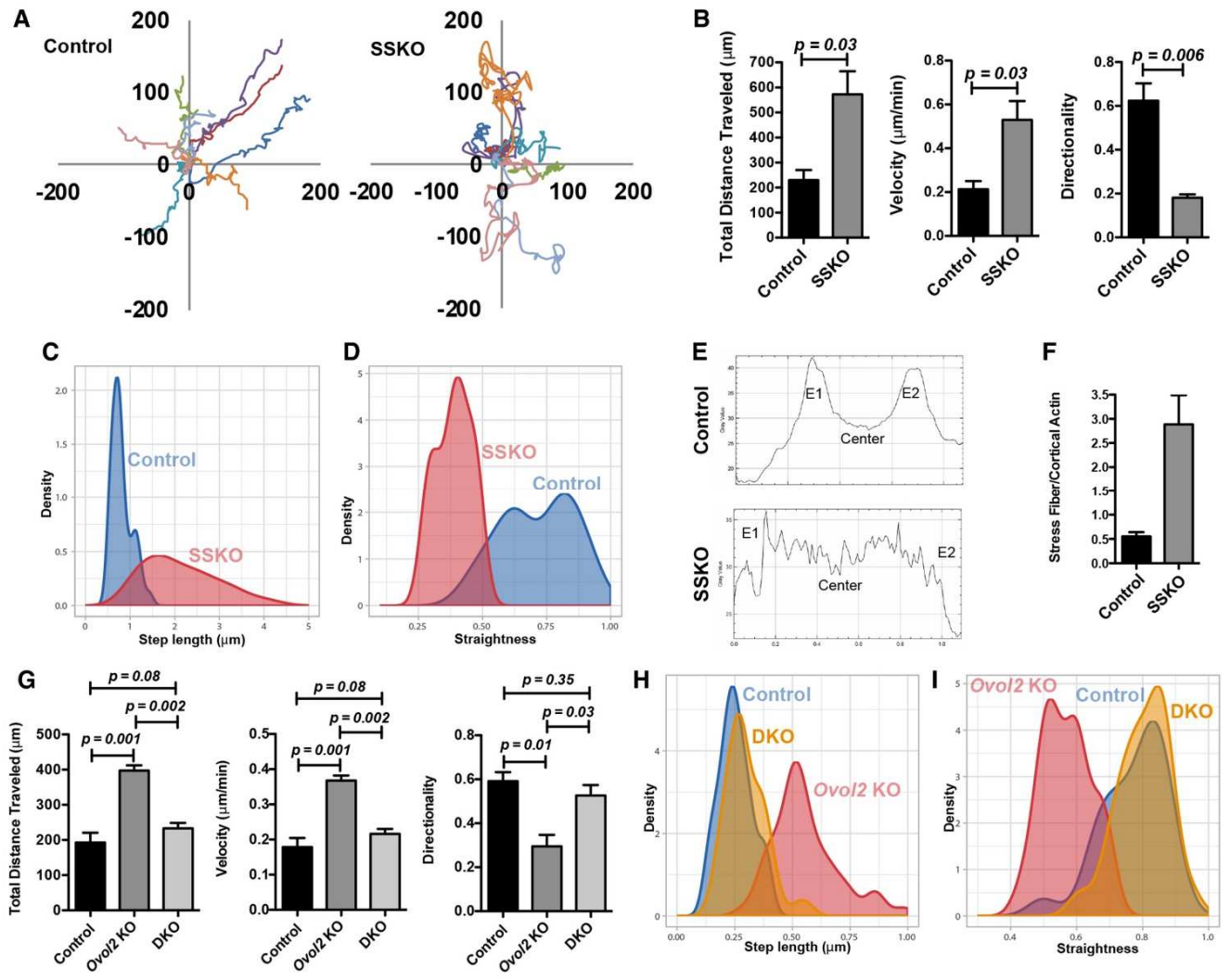


Figure 3.6. Compromised directional migration of *Ovo/2*-deficient Bu-HFSCs is rescued by *Zeb1* deletion

- A. Representative movement tracks of individual cells over an 18-h period.
- B. (B, G) Quantitative analysis of migration distance, velocity, and directionality of Bu-HFSCs with the indicated genotypes ($n = 3$ pairs; each biological replicate is an average of three different colonies with eight cells tracked per colony). *Ovo/2* KO, *Ovo/2*-deficient; DKO, *Ovo/2*- and *Zeb1*-deficient. (C, H) Step-length comparison among the indicated genotypes. Kolmogorov–Smirnov test: CTL vs. SSKO (E) or *Ovo/2* KO (H), $P < 10^{-10}$; CTL vs. DKO (H), $P = 0.06$. (D, I) Straightness distribution comparison among the indicated genotypes. Kolmogorov–Smirnov test: Control vs. SSKO (D) or *Ovo/2* KO (I), $P < 10^{-10}$, $P < 10^{-5}$; Control vs. DKO (I), $P = 0.45$. (E) Representative plots that show distribution of fluorescence intensity of actin staining in control and *Ovo/2* SSKO Bu-HFSCs. E1 (Edge-1) and E2 (Edge-2) signals correspond to cortical actin near the cell border, whereas center signals correspond to stress fiber actin. (F) Quantification of the ratio between E1 + 2 and center signals (E) in control and *Ovo/2* SSKO mice ($n = 2$ pairs).

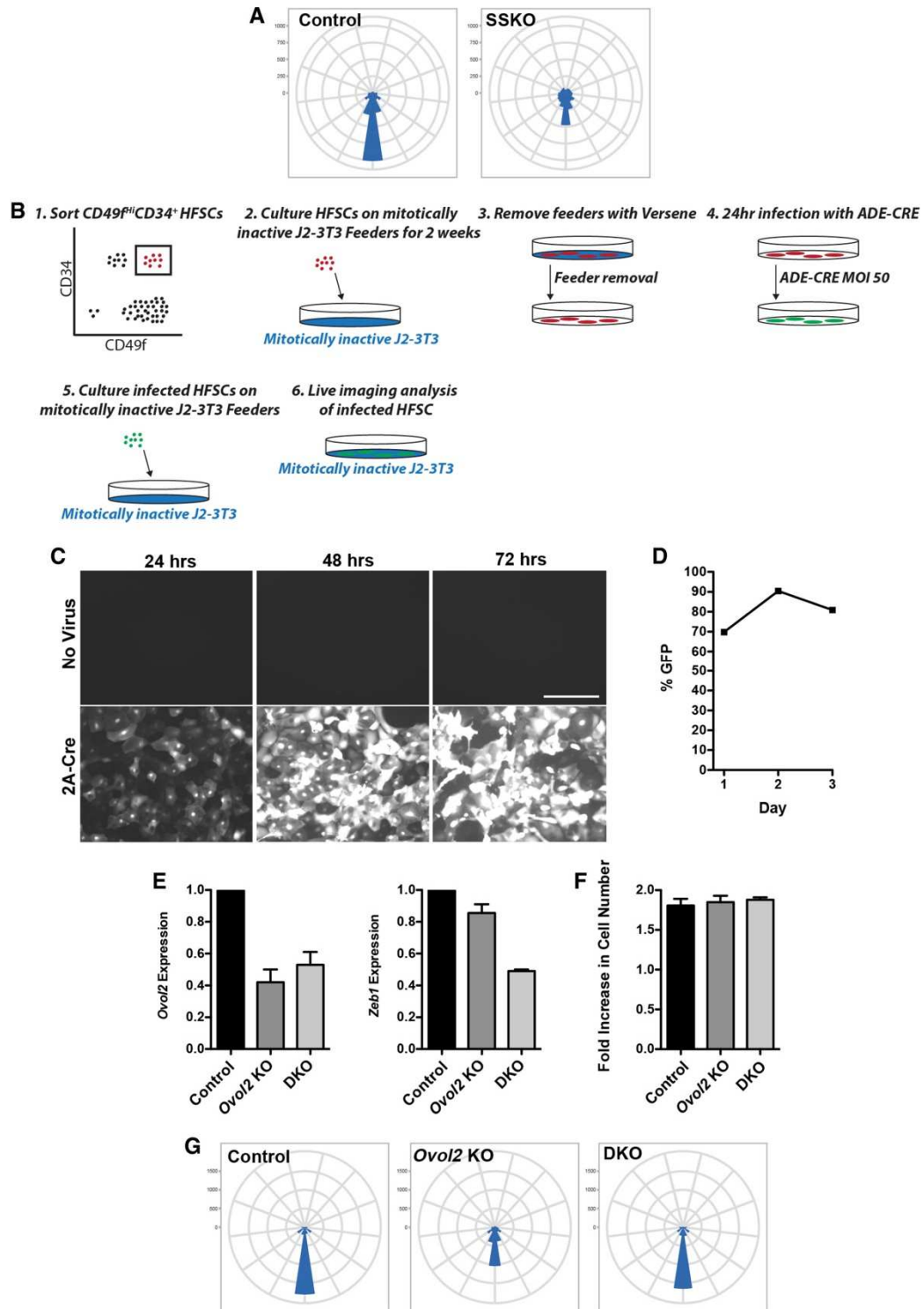
Data information: For statistical analysis in (B) and (G), we used an unpaired two-tailed Student's *t*-test. Error bars in (B), (F), and (G) represent mean \pm SEM.



Supplemental Figure 3.5. Supplemental data on Bu-HFSC migration

- A. Comparison of the distribution of turning angles between steps for control and *Ovo/2*SSKO Bu-HFSCs.
- B. Diagram of strategy for adenoviral infection of cultured Bu-HFSCs.
- C. GFP expression in infected Bu-HFSCs analyzed by epifluorescence
- D. GFP expression in infected Bu-HFSCs analyzed flow cytometry (2A-CRE-infected).
- E. RT-qPCR analysis confirming decreased expression of *Ovo/2* and/or *Zeb1* at 2 weeks after 2A-CRE infection of Bu-HFSCs ($n = 2$ pairs).
- F. Fold increase in cell number in control, *Ovo/2* KO, and DKO Bu-HFSC cultures as measured by live cell imaging over an 18-h period ($n = 2$ pairs).
- G. Comparison of the distribution of turning angles between steps for control, *Ovo/2* KO, and DKO Bu-HFSCs.

Data information: Scale bar, 100 μm in (E). Error bars in (E) and (F) represent mean \pm SEM.



**CHAPTER 4: Single-cell transcriptomics reveals molecular and
metabolic heterogeneity of epidermal basal cells during skin
homeostasis and wound healing**

Daniel Haensel, Suoqin Jin, Rachel Cinco, Peng Sun, Quy Nguyen, Zixuan Cang,
Morgan Dragan, Adam L MacLean, Kai Kessenbrock, Enrico Gratton, Qing Nie, Xing
Dai; To be submitted to Nature Communications

ABSTRACT

Basal cells promote epidermal tissue maintenance and contribute to repair following cutaneous wounding. Studies have indicated the existence of basal cell heterogeneity, but the extent and contributions during both normal homeostatic maintenance and repair is not well understood. Utilizing scRNA-Seq, we profile thousands of cells from total un-wounded (UW) and wounded (WO) skin. We identify major gene expression differences including immune- and EMT-related changes between epidermal basal cells from UW and WO skin. Computational and in vivo validation identifies four distinct basal cell states in UW skin, which are also present in WO skin but at different proportions. Gene expression analysis identifies metabolic heterogeneity in basal cells from WO samples, which is subsequently confirmed and found to be spatially localized around regions of the wound. Finally, we show this basal cell heterogeneity corresponds to sequential steps in lineage differentiation programs but with more fluid and plastic changes in the WO.

INTRODUCTION

Adult mouse skin is a self-renewing tissue composed of multi-cellular structural components including the epidermis, hair follicle (HF), and underlying dermis (Gonzales and Fuchs 2017). The epidermis is a stratified epithelium, organized into a differentiation hierarchy with proliferative stem/progenitor cells residing in the basal layer and differentiating cells in the suprabasal layers. Immediately above the basal cells are spinous cells, which differentiate into granular cells that subsequently give rise to stratum

corneum which constitutes an outer permeability barrier essential for animal survival and optimal health.

In general, epidermal stem cells (EpdSCs) in the basal layer represent a pool of fast cycling cells responsible for the homeostatic maintenance of the epidermis (Gonzales and Fuchs 2017; Dekoninck and Blanpain 2019). Some studies have suggested that bulk basal cells have equal potency and their decision to stay a proliferating stem cell or to initiate differentiation is stochastic (Gonzales and Fuchs 2017). Contrastingly, studies using sophisticated lineage tracing techniques have identified two spatially segregated populations of basal cells that divide at different rates (Sada et al., 2016), as well as rare cells in the basal layer that are already committed to terminal differentiation (Mascre et al., 2012). While these findings implicate the existence of heterogeneity within the epidermal basal compartment, a comprehensive picture of basal cell subsets and their molecular distinctions at a global level is currently lacking.

Upon cutaneous wounding, the skin alters its cellular dynamics to facilitate efficient healing in order to restore the protective barrier. Wound healing represents a coordinated process with several distinct but overlapping stages: inflammation, re-epithelialization, and resolution (Gurtner et al., 2008). The inflammation stage is characterized by the infiltration of a large number of immune cells in order to clear pathogens. Re-epithelialization is driven by proliferation and migration of epidermal cells at the wound periphery (Park et al., 2017; Haensel and Dai 2018). Concurrently, there is a large influx of fibroblasts into the wound bed that can proliferate and differentiate into contractile myofibroblasts (Gurtner et al., 2008). Much remains to be learned about precisely how

cellular and molecular heterogeneities are restructured during wound healing, particularly within the epidermal basal cells that are the major drivers of re-epithelialization.

Single-cell RNA-sequencing (scRNA-Seq) is a powerful technique that enables the transcriptomic analysis of large numbers of cells simultaneously. In this work, we sequenced thousands of cells that constitute the normal mouse back skin, and wounded skin at the re-epithelialization stage, to characterize the general changes in cellular makeups as well as alterations in basal cell heterogeneity between homeostasis and repair. Our analysis confirms the significant increases in immune cells and fibroblasts in wounded skin. More importantly, we identify four distinct states of basal cells in normal back skin that shift proportions and gene expression during wound healing. Using RNAScope and fluorescence lifetime imaging microscopy (FLIM), we validate the molecular and metabolic heterogeneities at a single-level in normal skin *in situ*, and report a significant shift in the relative level between glycolysis and oxidative phosphorylation in the neo-epidermis of wounded skin. Using standard and custom tools to predict cell trajectories and lineage relationships, we are able to place the different basal cell subsets temporally onto a differentiation hierarchy and identify remarkable plasticity of epidermal basal and spinous cells in their differentiation trajectories during wound healing.

RESULTS

scRNA-seq reveals global changes in cellular makeup during wound healing

To examine major cellular differences between skin homeostasis and repair, we performed scRNA-seq on samples isolated from unwounded (UW) and wounded (WO) mouse back skin (Figure 4.1A). The wound samples were taken at 4 days after the

introduction of 6-mm wounds, corresponding to a stage of active re-epithelialization (Figure 4.1B and Supplemental Figure 4.1A). We performed read depth normalization, visualized control metrics (Supplemental Figure 4.1B and see Methods section), and obtained a total of 10,615 (from 2 UW biological replicates) and 16,164 (from 3 WO biological replicates) cells for downstream analyses.

We first analyzed the UW and WO sample types separately, surveying major cellular compositions and changes from homeostasis to repair. Biological replicates were aggregated together, and batch corrected using Canonical Correlation Analysis (CCA) implemented in the Seurat R package (Butler et al., 2018). t-distributed stochastic neighbor embedding (tSNE) of cells from UW and WO samples showed that there was good mixing between the replicate samples; however, unsurprisingly some residual batch effects still persisted after CCA correction due to individual variations (Supplemental Figure 4.2A and B). Marker genes were found for each individual tSNE cluster and used in tandem with known cell type markers (Joost et al., 2016, 2018; Han et al., 2018; Meador et al., 2014) to determine the identity of each cluster (Figure 4.1C, D; Supplemental Figure 4.2C, D). Using identical parameters for UW and WO samples, we observed 15 and 14 cell clusters, respectively (Figure 4.1C and D). Immediately obvious were the 1) emergence of new distinct cell type clusters including macrophages, dendritic cells (which also includes the Cd207⁺ Langerhans cells), myofibroblasts, and endothelial cells in the latter; and 2) a reduced number of distinct epidermal and HF cell clusters, implicating wound-induced alterations in skin epithelial composition. Feature plots of key cell type markers revealed population-level changes in epidermal basal cells (*Krt14*), epidermal

spinous cells (*Krt1*), HF-associated cells (*Krt17*), immune cells (*Cd45*), and fibroblasts (*Col1a2*) (Figure 4.1E and F).

Next, we combined data from all 5 samples above to facilitate direct comparison between UW and WO skin (Figure 4.1G). In the overall tSNE plot, similar-cell types from UW and WO skin – i.e., the three major cell type clusters, epithelial cells, fibroblasts, and immune cells segregate together (Figure 4.1G and Supplemental Figure 3). When cells were visualized for their sample/replicate identity, the immune cells showed greater degree of cellular diversity between UW and WO samples than fibroblasts and epithelial cells (Figure 4.1H). Quantitative analysis revealed that the relative percentages of both immune cells and fibroblasts were increased in the WO samples at the expense of epithelial cells (Figure 4.1I), which is consistent with what is expected for cutaneous wound healing (Shaw and Martin 2009). Overall, these data provide a general overview of the major changes in cellular heterogeneity from homeostasis to a wound healing state.

We next subset out all the epithelial cells for further analysis. With reduced cellular complexity (e.g., excluding immune cells and fibroblasts), we detected comparable numbers of epidermal and HF cell clusters in the UW and WO samples (Supplemental Figure 4.4 and 4.5). We found that both UW and WO samples contain four basal cell subpopulations, two spinous cell subpopulations, and four HF subpopulations, which are generally consistent with the reported scRNA-seq data using Fluidigm C1 platform (Joost et al., 2016). Of note, we observed a distinct cluster of proliferating basal cells in both UW and WO skin (Figure 4.1C, D and Supplemental Figure 4.4A, B, E, F), which has not been reported in the previous single-cell study of adult mouse skin. Although loricrin⁺ granular cells were reported as a minor population in the previous study, the presence of a similar

population was negligible in both UW and WO samples. Overall, the relative proportions of the various epithelial cell types did not dramatically change (Supplemental Figure 4G).

Wound epidermal basal cells show upregulated expression of inflammation-and migration-related genes

Epidermal basal cells are major players in wound re-epithelialization (Shaw and Martin 2009). We therefore subset for the K14⁺ cell populations from the epithelial cells but excluded the clusters that express HF markers K17 (Supplemental Figure 4.4E and F). We also excluded the proliferative K14⁺ basal cell cluster in this analysis, reasoning that the highly expressed proliferation-associated genes in these cells might overshadow the subtler but potentially interesting differences between UW and WO K14⁺ basal cells (Supplemental Figure 4.6A-C). A total of 53 and 99 genes were particularly enriched in bulk basal cells of UW and WO samples, respectively. The expression levels of the top 10 enriched genes in UW or WO basal cells were not uniform across all single cells, implicating basal cell heterogeneity within each of the samples (Figure 4.2A). For example, some basal cells from the UW samples displayed a WO-like signature but not vice versa (Figure 4.2A). Gene Ontology (GO) analysis using all differentially expressed genes revealed enrichment of different GO terms in UW and WO basal cells, featuring prominently molecular signatures associated with inflammation (e.g., TNF α signaling, Interferon Gamma Response) and the epithelial to mesenchymal transition (EMT) in the latter (Figure 4.2B). Individual inflammatory genes (such as *Cxcl2*, *Ccl2*, and *Ccl7*) and EMT-related genes (such as *Snai2* and *Vim*) showed clear enrichment in the WO basal cells (Figure 4.2C). Not surprisingly, *Krt16* - previously shown to be upregulated upon

wound healing (Wawersik et al., 2013), was also enriched in the WO basal cells (Figure 4.2C).

We next used gene scoring, defined by a gene set such as from a GO term, to generate an enrichment score based on the expression of a set of genes (see Methods section). This analysis not only validated the known GO terms enriched in the basal cells from the WO population, but also revealed the overall changes in basal cell heterogeneity from UW to WO samples (Figure 4.2D). Specifically, the UW basal cells encompassed two subsets of cells with low or high score for TNF α signaling, a generic inflammatory response gene signature, but the WO basal cells seemed to be predominantly high-scoring for these terms (Figure 4.2D). Furthermore, both a generic wound healing gene signature and a custom gene set including those that are up-regulated in the migratory front of wound neo-epidermis (i.e., α 5 integrin-expressing cells) (Aragona et al., 2017) showed considerable enrichment in the basal cells from the WO samples (Figure 4.2D). Together, these data demonstrate that epidermal basal cells upregulate inflammatory and migratory gene signatures during wound healing, and their inflammation-associated gene expression switches from the initially heterogeneous states to a more homogeneous, inflammation-high state.

Three distinct non-proliferative basal cell subsets exist in un-wounded skin

To better delineate unknown heterogeneity within the non-proliferative basal cells of normal epidermis in an unbiased fashion, we next clustered and visualized UW basal cells, again excluding the proliferative subset (see Figure 4.2). Indeed, three distinct clusters were found (Figure 4.3A), and each was identified by specific marker genes

(Figure 4.3B). Cluster 1 was defined by top markers such as *Trp63* and *Col17a1* and was therefore named the *Col17a1*^{Hi} cluster (Figure 4.3C; Supplemental Figure 4.7A). *Trp63* encodes a transcription factor well-characterized for its master-regulatory role in epidermal development and adult epidermal homeostasis (Truong et al., 2006; Sano et al., 2007), and its expression is enriched in quiescent bulge hair follicle stem cells (Bu-HFSCs) compared to activated counterparts (Lien et al., 2011). *Col17a1* encodes a component of the hemidesmosome and a negative regulator of proliferation in both developing and adult epidermis (Watanabe et al., 2017). Recent work has also suggested that *Col17a1*-expressing cells undergo symmetric divisions, produce clones in the epidermis that eventually dominate (Liu et al., 2019). Cluster 2 was named as the Early Response (ER) subpopulation due to enrichment for a number of immediate early genes (Figure 4.3C; Supplemental Figure 4.7A) (Herschman 1991). Top markers of this cluster also include those associated with activated Bu-HFSCs relative to quiescent Bu-HFSCs (Lien et al., 2011) or with known function in regulating proliferation (Zenz and Wagner 2006; Briso et al., 2013; Rotzer et al., 2006; Florin et al., 2006; Zhu et al., 2008; Andrianne et al., 2017) (Figure 4.3C; Supplemental Figure 4.7A). Cluster 3 showed enriched expression of genes with known functions in promoting cell cycle arrest, such as *Cdkn1a*, *Irf6*, *Ovol1*, and *Sfn* (Topley et al., 1999; Nair et al., 2006; Ingraham et al., 2006; Hammond et al., 2012) (Figure 4.3C; Supplemental Figure 4.7A), and was therefore designated the Growth Arrested (GA) cluster. Interestingly, genes enriched in *Col17a1*^{Hi} cells and those in GA cells presented a trend of inverse correlation among the three clusters (Figure 4.3C). GO analysis of the Hallmark gene sets for each cluster revealed a specific enrichment of TNF α signaling and hypoxia signatures in the ER and even more

so in the GA basal cells, and an enrichment of EMT signature in GA basal cells (Supplemental Figure 4.7C). Gene scoring confirmed that the GA population has the highest inflammatory and EMT signatures (Figure 4.3D). We also noted that the Col17a1^{Hi} cells had the highest quiescence score as well as the lowest epidermal differentiation score (Figure 4.3D), which suggests that these cells may represent the most primitive epidermal stem/progenitor cells. As a means to compare to other published studies, we noted that the GA basal cluster was enriched for genes associated with the LRC (Supplemental Figure 4.7B).

To validate the existence of these different basal cell states *in vivo*, we utilized RNAScope as a highly sensitive and semi-quantitative means to examine RNA expression *in situ*. Co-analysis of *Cdkn1a* and *Krt14* transcripts with K14 protein revealed several interesting points: 1) the levels of *Krt14* transcript and K14 protein fluctuated along the basal layer of the epidermis; 2) the degree of cell-cell variation was far more dramatic for *Krt14* transcript than for K14 protein, and the location of such variation did not always coincide; 3) *Cdkn1a* transcripts were indeed present in some but not all of the K14-positive basal cells, but the highest expression was detected in a subset of the suprabasal cells (Figure 4.3E and G). Co-analysis of *Cdkn1a* with markers of the Col17a1^{Hi} (*Trp63*) and ER (*Id1*) basal cell clusters indeed revealed cells in the basal layer that uniquely express each of these markers (Figure 4.3F, H-J and Supplemental Figure 4.7D-F). Few cells were found to express 2 of the 3 markers, whereas none expressed all 3 markers (Figure 4.3I and J). The inverse relationship between *Trp63* and *Cdkn1a* expression in basal cells is also evident (Figure 4.3H-J). Taken together, these results validate the

existence of molecular heterogeneity within the epidermal basal cell compartment in the intact tissue.

Alteration and spatial partitioning of basal cell subsets in wounded skin

We next turned to the WO samples to ask whether distinct basal cell states also exist during wound healing, and whether there is any alteration from the UW skin. Similar to the UW basal cells, unsupervised analysis revealed the presence of three distinct non-proliferative basal cell subsets (Figure 4.4A). Comparison of marker genes revealed significant overlaps between the WO-associated clusters and those present in the UW sample (Figure 4.4B and C; Supplemental Figure 4.8A). More specifically, we found that each basal cell subset in the WO sample shared a large portion of marker genes with a single basal cell subset in the UW sample (Supplemental Figure 4.8A). Using marker genes from the UW basal cell subsets, we scored the basal clusters from the WO sample and found that the WO clusters can be identified similarly to the UW samples as belonging to Col17a1^{Hi}, ER and GA clusters (Supplemental Figure 4.8B). Random Forest classification confirmed the validity of this assignment (Supplemental Figure 4.8C, see Methods section). However, it is important to note that distinct molecular differences still existed between the different WO clusters and their UW counterparts.

Having established the correlations between the basal cell subsets in WO and UW skin, it was clear that the GA cluster is expanded in the WO skin at the expense of the Col17a1^{Hi} cluster (Figure 4.4A and D). Similar to the UW skin, the WO GA cells are particularly enriched for genes associated with α 5-integrin-positive migrating front, inflammation, hypoxia, and have the lowest quiescence score but the largest epidermal

differentiation score (Figure 4.4E and Supplemental Figure 4.9A). Interestingly, the Col17a1^{Hi} cluster displayed no enrichment for GO terms in the UW skin, but showed a significant enrichment for oxidative phosphorylation genes in the WO skin (Supplemental Figure 4.9A). We will return to this point later.

We noted that individual genes that are previously known to be enriched in the migratory front, such as *Krt16*, *Hbegf*, and *Snai2*, were enriched, whereas *Cd9* that is known to be downregulated in the migratory front, was de-enriched in the GA population (Supplemental Figure 4.9B and C) (Haensel and Dai 2018; Shirakata 2005; Jiang et al., 2013). Immunofluorescence confirmed the enrichment of nuclear Snai2 protein in basal cells at the migrating front relative to those in the hyperproliferative zone or distal to the wound (Figure 4.4F and Supplemental Figure 4.9D). On the other hand, Fos – a marker of the ER population, was enriched in the proliferative zone, but as the wound transitions to the migratory zone or non-wounded area, its expression dissipated (Figure 4.4G and Supplemental Figure 4.9E). We also performed RNAScope to examine the expression of GA marker *Cdkn1a* in the WO skin. While strong *Cdkn1a* expression was seen in numerous superbasal cells of the hyperproliferative zone but was scattered in the basal layer, both the basal and suprabasal cells of the migrating front showed prominent *Cdkn1a* signals (Figure 4.4H-J and Supplemental Figure 9F). Quantification of *Cdkn1a* signals along the entire basal layer of the wounded area revealed a clear increase in the migrating front (Figure 4J).

Collectively, our observations show that an inflammation^{high}/EMT^{high} basal cell subset exists in normal skin as a growth-arrested (GA) state, and that this subset is dramatically expanded during wound healing. Moreover, our data reveal that this

epidermal basal cell subset is largely enriched in the migrating front of the wound. These results are supported by previous studies using independent methodologies such as intravital imaging (Park et al., 2017), and that those in the wound proliferative zone are enriched for the ER subset.

Metabolic heterogeneity in basal cells of the normal and wounded skin

Intrigued by the enrichment of an oxidative phosphorylation GO term in the Col17a1^{Hi} population of the WO skin (Supplemental Figure 4.9A), we performed gene scoring analysis using an oxidative phosphorylation gene signature to compare all 4 basal cell subsets in UW and WO skin. This analysis revealed that under both conditions, the Col17a1^{Hi} and the proliferative basal cell subsets had the highest, whereas the GA cluster had the lowest, oxidative phosphorylation score (Figure 4.5A and Supplemental Figure 4.10A). In keeping with a low oxidative phosphorylation state, the GA subset also showed enhanced expression of *Hif1a*, which encodes a master transcriptional regulator of hypoxia response (Supplemental Figure 4.10B).

The exaggerated spatial partition of the different basal cell subsets in the WO skin enabled us to map the metabolic states in different regions of the wound. Specifically, we performed two-photon excitation (TPE) and FLIM to examine the autofluorescence of NADH as a readout of the relative level of oxidative phosphorylation and glycolysis in individual cells (Stringari et al., 2015). Using *K14-Cre/mTmG* mice to visualize epidermal cells (GFP-positive), we probed areas outside of the wound, portions of the proliferative zone, and regions of the migratory front deep within the wound, focusing specifically on the basal layer (Figure 4.5B and C). TPE NADH intensities and lifetimes were captured

and displayed in phasor plots (Figure 4.5D and E). Free-to-bound NADH ratios, indicative of the relative level of oxidative phosphorylation (Stringari et al., 2015, 2012), were calculated from each individual basal cell in each region of the wound. The ratios were indeed highest in basal cells of the neo-epidermis and lowest in those of the regions outside the wound (Figure 4.5F and G). Interestingly, cell-cell variation was observed in all the different regions of the wound and even in regions far from the wound (Figure 4.5F), indicating metabolic heterogeneity within the basal layer. Overall, these data support our scRNA-seq analysis and show that basal cells in the wound neo-epidermis are generally more prone to utilizing glycolysis as their metabolic pathway, whereas those in the wound periphery are more prone to undergoing oxidative phosphorylation.

Pseudotemporal ordering and trajectory analysis revealed transition dynamics and cellular plasticity during epidermal differentiation

To determine lineage relationships among the four basal cell subsets in the context of epidermal differentiation, we performed pseudotemporal ordering of all interfollicular epidermal cells, which include proliferating and non-proliferating basal cells as well as spinous cells, using Monocle 2 for trajectory analysis (Trapnell et al., 2014; Qiu et al., 2017; Qiu et al., 2017) (Supplemental Figure 4.11). Monocle 2 is unable to determine the initial cell of the trajectory without prior knowledge: we predicted the Col17a1^{Hi} state to be the initial state due to it having the highest quiescence score and lowest epidermal differentiation score (Figure 4.3D). In both UW and WO skin, we observed three branches from the Col17a1^{Hi} cells leading to three cell state endpoints: proliferating basal cells, GA basal cells (transitioning through ER basal cells), and spinous cells (Supplemental Figure

4.11). Col17a1^{Hi} cells are distributed along the start of each of these branches, exacerbating the challenge of identifying the initial cell state in pseudotime (Supplemental Figure 4.11A and D).

To identify an initial state in pseudotime a priori, we used our method scEpath, which quantifies the developmental potency of single cells and can infer transition probabilities and lineage relationships between cell states (see Methods section) (Jin et al., 2018). Using UMAP for dimensional reduction, we visualized the cells by sample identity and noted clear batch effects (Supplemental Figure 4.12A and D), which we corrected for (Supplemental Figure 4.12G, J, and see Methods section). In both the UW and WO samples, Col17a1^{Hi} basal cells displayed the lowest energies (Supplemental Figure 4.12H and K). We found that lower energies, while typically associated with committed/differentiated cell states (Jin et al., 2018; Teschendorff and Enver 2017), also associate with quiescent cell states. When we consider the known quiescent Bu-HFSC population, we see that it has the lowest scEnergy of the cell states (Figure 4.3D, 4.4E; Supplemental Figure 4.4H, 4.12H, 4.12K; see Methods section). We thus predicted that Col17a1^{Hi} basal cells – which have the lowest scEnergies of the basal cell states – represent the initial state in pseudotime.

scEpath identified three branches in the UW sample (as for Monocle): proliferative basal, non-proliferative basal, and spinous, each with distinct marker gene expression changes during pseudotime (Figure 4.6A and B). The non-proliferative basal cell branch originated from the Col17a1^{Hi} cells and transitioned through ER to GA cells (Figure 4.6A). Similar branching trajectories and gene expression changes were found for the WO

sample, but with less distinction between the non-proliferating basal and the spinous cell branch on the UMAP projection (Figure 4.6D and E).

To analyze the epidermal differentiation dynamics in UW and WO skin further, we performed RNA velocity analysis, a computational tool to predict short-term changes in cell differentiation, taking advantage of the ability to discriminate between spliced and unspliced mRNA (La Manno et al., 2018). These dynamics are visualized by vectors (arrows) on the UMAP projection that predict both the direction of the transition (e.g. Col17a1^{Hi} to GA) and its rate (the arrow length). We developed a non-linear model of RNA velocity that used Hill functions to describe the effects of pre-mRNA on the abundance of mature mRNA (see Methods section). RNA velocity predicted three branches in both the UW and WO samples (Figure 4.6C and F), in agreement with the both the Monocle and the scEpath analyses above. It also found the Col17a1^{Hi} basal cells in both UW and WO samples to be changing most slowly (represented by short arrows), an independent prediction that this population represents a quiescent state. As cells left the Col17a1^{Hi} state they did so rapidly (represented by long arrows), transitioning quickly towards other basal or spinous cell states (Figure 4.6C and F). Remarkably, the UW proliferating basal cells followed a cyclical trajectory that originated from the Col17a1^{Hi} cells, branched off during the ER state, passed through the proliferative state, and then returned to the Col17a1^{Hi} state (Figure 4.6C and F). These intriguing cyclical (i.e. transitory) cell dynamics were faithfully recapitulated in the WO sample. RNA velocity also provided evidence of the additional cell state plasticity observed in the WO sample relative to UW cells. Bidirectional transitions between the two main branches (non-proliferating basal and spinous) are found in the WO sample that are not present between the same

branches in the UW sample. We also observe larger vectors (longer arrows) overall in the WO case, indicating faster changes in gene expression programs and perhaps more abrupt transitions between cell states (Figure 4.6C and F).

Investigating gene expression dynamics over pseudotime, we found that genes such as *Trp63*, *Fos*, and *Cdkn1a* followed dynamic expression levels as they transitioned from the Col17a1^{Hi} to GA populations (Supplemental Figure 4.13A). We then looked at the global gene expression changes over pseudotime in both the UW and WO samples (Figure 4.6G and Supplemental Figure 4.13C). scEpath identified 3699 pseudotime-dependent genes (genes that change significantly over pseudotime) for the UW sample. These changes appeared gradually during pseudotemporal progression but studying the same gene set applied to the WO sample, we see abrupt temporal changes (Figure 4.6G). When these genes are visualized along the proliferative basal branch, similar patterns with slight shifts are observed, perhaps reflecting an activated wound-induced state (Supplemental Figure 4.13C).

The pseudotime-dependent genes can be grouped into four clusters. Gene Cluster I in the UW sample is high early in pseudotime and subsequently downregulated. This cluster is enriched for genes associated with translation-related processes (Figure 4.6G). Gene Cluster II is associated specifically with the proliferative basal cells and is enriched for cell cycle-related processes (Figure 4.6G and Supplemental Figure 4.13A). Gene Cluster III represents a transitory state enriched for cell cycle genes as well as mRNA transcription and processing-related genes (Figure 4.6G). Gene Cluster IV, which appears at the end of pseudotime, is associated with mRNA processing and the initiation of translation (Figure 4.6G). All of these gene clusters shifts in the WO sample compared

to the UW sample. We also took a curated approach, specifically studying transcription factors and EMT-related genes pulled out from the total 3699 pseudotime dependent genes. We found that the UW pseudotime-dependent transcription factors displayed similar patterns as the WO sample, suggesting that core transcriptional machinery remains in place (Figure 4.6H). Finally, we examined UW pseudotime-dependent EMT-related genes, which displayed at times, major shifts when comparing these genes in the WO sample (Supplemental Figure 4.13B). We noted both forward and reverse, and even at times displayed bimodal distributions (Supplemental Figure 4.13B).

Together, these analyses of cell trajectories revealed multiple distinct programs of epidermal differentiation and highlight the following key points: 1) Col17a1^{Hi} cells likely represent the most primitive cell state in the epidermal basal compartment; 2) one possible fate of these cells is to become “activated” (ER, an early response-like stage) and subsequently undergo growth arrest (GA); 3) proliferating basal cells are integrated into the overall basal cell dynamics: proliferation is initiated from the ER state and cells return to the Col17a1^{Hi} state after replication; 4) wound healing enhances cell fate plasticity in epidermal cells such that bidirectional conversions between basal and spinous cells are possible; and 5) the pseudotemporal dynamics shifts upon wound healing.

DISCUSSION

EpdSCs in the epidermal basal layer of mouse adult skin maintain epidermal homeostasis by constantly replacing differentiated cells (Gonzales and Fuchs 2017). Basal cells also must be able to alter their proliferative and migratory dynamics in the

context of wound healing to facilitate re-epithelialization (Haensel and Dai 2018). Published scRNA-Seq works provide a comprehensive characterization of the epithelial components of adult mouse skin during homeostasis, regeneration and repair, with a large focus on the contribution of Bu-HFSCs during wound healing (Joost et al., 2016, 2018). Our study has combined scRNA-Seq with *in situ* validation methods to uncover previously unknown molecular and metabolic heterogeneities of the epidermal basal cells in normal skin and during the re-epithelization stage of wound healing. We have identified 4 distinct basal cell states, namely Col17a1^{Hi}, early response (ER), growth arrested (GA), and proliferative, in mouse back skin that alter gene expression as well as shift in relative proportions during wound healing. Using established and novel computational pipelines, we order these distinct stages into a differentiation hierarchy, revealing cyclical transitions of basal cells through the proliferative state, as well as faster cell state dynamics and greater plasticity during wound healing.

Col17a1 is well characterized for its master regulatory role in various aspects of epidermal development, including the initial specification from simple epithelia, promotion of stratification, proliferation, as well as terminal differentiation (Yang et al., 1999; Mills et al., 1999; Truong et al., 2006; Pattison et al., 2018; L. Li et al., 2019). Consistent with such broad-spectrum involvement in multiple cellular processes, we detected its mRNA expression in not only basal cells but also spinous cells. A Col17a1-high basal cell state is apparently a cellular state with high quiescence signature (note that this signature is distinct from that of growth arrest/cell cycle exit), high oxidative phosphorylation, but low EMT, low differentiation and low hypoxia/inflammation. Notably, the Col17a1^{Hi} cluster is enriched for *Col17a1*, which in recent lineage tracing studies has shown that cells that

express high levels of *Col17a1* have potential to give rise to long term epidermal stem cells, which can outcompete other cells (Liu *et al.*, 2019). These molecular characteristics are suggestive of a relatively inert, primitive stem/progenitor cell state, a notion supported by its placement as the initial state in the epidermal lineage using several different computational methods, as well as the apparent mobilization of these cells in case of increased demands for cellular outputs during wound healing. Future lineage tracing experiments outside the scope of the current work will be able to test this intriguing possibility.

ER genes such as *Fos* and *Jun* are known to be upregulated by flow cytometry (van den Brink *et al.*, 2017), casting doubts on whether an ER basal cell state truly exists *in vivo*. This said, we were able to detect epidermal basal cells that express Fos protein or *Id1* mRNA (albeit at a low level) *in situ*. In all gene expression and lineage prediction analyses, these cells occupy an intermediate position between *Col17a1*^{Hi} and GA cells, raising the possibility that ER is an obligatory transition state when dormant cells become activated to proliferate or migrate.

Also of interest is the GA cell population that can be detected via *Cdkn1a* expression in the basal layer. The enrichment of a gene signature derived from a label-retaining basal cell (LRC) population reported by Sada *et al.*, 2016 in these GA cells as compared to the *Col17a1*^{Hi} and ER basal cells (Supplemental Figure 4.7B) is in keeping with a predicted growth arrested state. In the future, it will be interesting to further examine the spatial and temporal correlations between the functionally defined LRC and molecularly defined GA cells to seek a holistic picture of basal cell dynamics during homeostasis and repair.

It is well known that epidermal cells in wounded skin upregulate the expression of EMT- and immune-related genes (Aragona et al., 2017). Our findings confirm this notion, but also show that such gene expression program is an inherent feature of a subset of the basal cells (i.e., GA cells) in normal epidermis during homeostasis that is significantly expanded in size during wound repair. Both our scRNA-seq and RNAscope data point to an intimate connection between the GA cells and wound migrating front. As such, our results offer an independent validation of the previous finding that migration and proliferation are spatially separated in the healing wound, with migrating cells at the tips of the growing neo-epidermis being generally devoid of proliferative activity (Park et al., 2017). Moreover, these data suggest that the wound repair process capitalizes on the existing heterogeneity within the normal skin epidermis but redirects it towards a spatially coordinated program of proliferation and differentiation to facilitate efficient re-epithelialization. Although involucrin expression in these cells was not detectable in our scRNA-seq data, it is tempting to speculate that the GA basal cells in normal epidermis represent a subset of basal cells that are post-mitotic, most committed to differentiation, and most prone to migrate upward. The high expression of EMT, hypoxia, inflammation genes in these GA cells implicate them as the most ready to respond to the extracellular signals of the everchanging tissue microenvironment. Their low oxidative phosphorylation score (Figure 4.5A and Supplemental Figure 4.10A), high *Hif1a* expression (Supplemental Figure 4.10B and C), and enrichment in the wound migrating front are consistent with the wound bed being a hypoxic environment and implicate the potential existence of “mini-hypoxic pockets” in normal epidermis during homeostasis. In this context, it is interesting to note that *Hif1a* has known wound healing functions such as

promoting a metabolic switch to glycolysis, EMT, as well as the return to normoxic conditions within the wound, a state that is difficult to achieve in diabetic wounds (Hong et al., 2014).

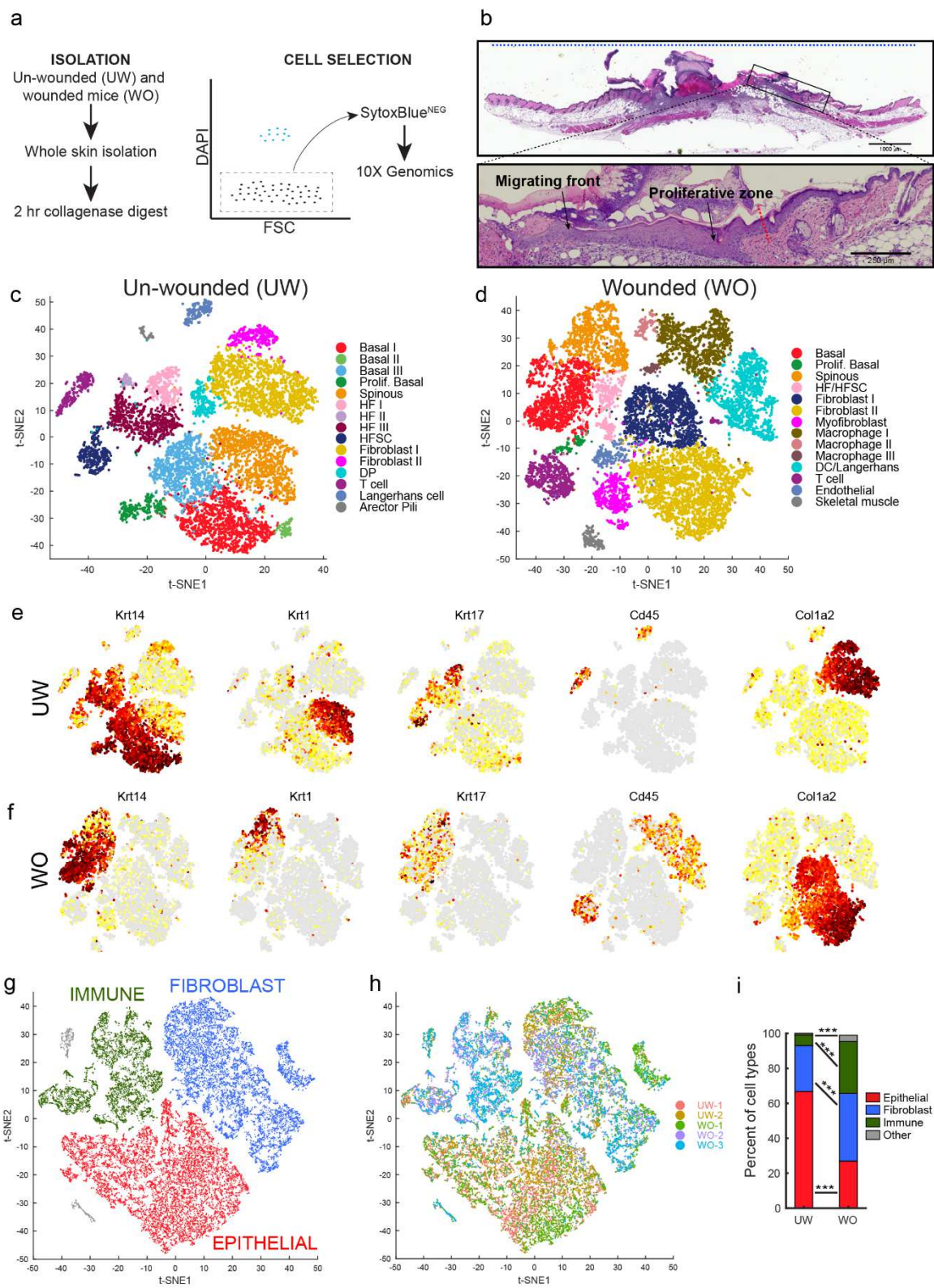
Perhaps the most surprising finding in our study is the lack of consistent evidence pointing to efficient conversion of basal cells into the spinous cells in normal skin. The prediction by all computational methods that Col17a1^{Hi} cells can transition into spinous cells without going through an obligatory step of growth arrest is also puzzling. While we cannot formally exclude the possibility that in adult mouse back skin, non-proliferating Col17a1^{Hi} basal cells can undergo direct differentiation to become spinous cells, it is likely that this prediction is biased by the presence of Col17a1^{Hi} spinous cells. Overall, our lineage predictions are probably more in line with a scenario in which basal cell differentiation into spinous cells is a rare and slow event not readily captured by the methodologies we used. In contrast, we would expect a linear and continuous differentiation pathway linking basal and spinous cells in embryonic epidermis, where active morphogenesis occurs. RNA velocity greatly assisted in our understanding of the cellular dynamics of the proliferating cells as it made it clear that these cells do not represent a terminal branch but rather a loop. The large vector sizes in both the GA and the SP2 populations suggest that many of these cells are in transitional states: it remains a challenge to decompose the lineages of such transitional states with current computational methods.

Cellular plasticity was detected in the wounded skin using RNA velocity: several vector paths were observed to bridge the different basal and spinous populations (Figure 6f). This interchange between the non-differentiated and differentiated cell types suggests

greater fluidity between cell states relative to normal adult skin. Supporting this notion, in RNAScope experiments we observed several suprabasal cells that express basal marker K14 in wound neoepidermis especially at the migrating front (Figure 4.5H and I). In addition, the cells that bridge the non-proliferative basal branch and the spinous branch are indeed double positive for K14 and K1 (see arrows in Figure 4.6E). If we consider adult repair and regeneration to be reminiscent (or a re-activation) of developmental programs (Blanpain and Fuchs 2014), increased cell state fluidity is clearly a desirable feature of epidermal cells during wound healing. Collectively, our findings provide new insights into the cellular and molecular dynamics of normal and wounded skin and lay a solid foundation for future dissection of impaired wound healing processes in various disease states in order to facilitate precise therapeutic intervention.

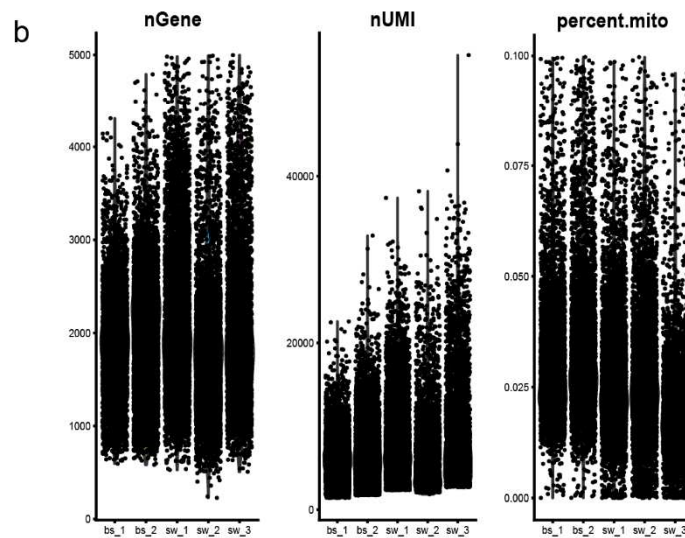
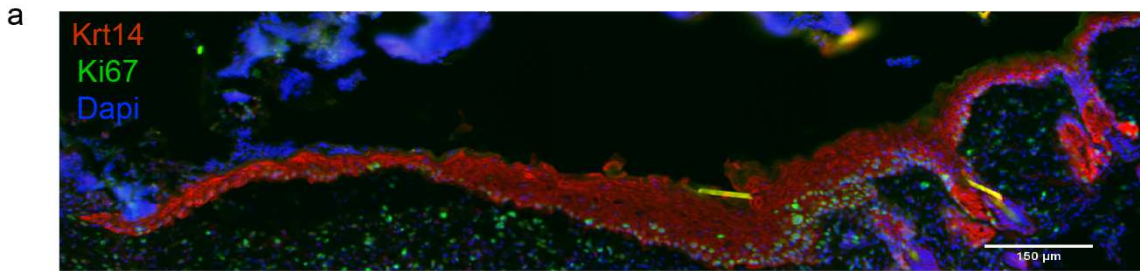
Figure 4.1: scRNA-Seq reveals global changes in cellular makeup during wound healing

- (A) Schematic diagram detailing the single cell isolation methods of UW and WO sample as well as the cell selection before processing for 10X Genomics pipeline.
- (B) H/E analysis of equivalent WO sample. Above: Yellow dashed line indicates representative 10 mm region isolated for single cell suspension. Below: Zoomed in region of neo-epidermis containing migrating front and proliferative zone. Red dashed line indicates wound margin.
- (C) tSNE plot containing 2 samples from un-wounded skin that were aggregated and then batch corrected using CCA.
- (D) tSNE plot containing 3 samples from wounded skin that were aggregated and then batch corrected using CCA. Principle components and resolution parameters utilized in (C) were also utilized in (D).
- (E) Feature plots highlighting genes from major cell types in UW sample.
- (F) Feature plots highlighting genes from major cell types in the WO sample.
- (G) tSNE plot containing all samples (2 UW and 3 WO) with the major cell type populations (epithelial, fibroblast, and immune) highlighted.
- (H) tSNE plot containing all samples (2 UW and 3 WO) with each replicate sample identified by a unique color identifier.
- (I) Bar graph representing the major cell type populations in the UW and WO samples. For statistical analysis, Chi-squared test was used ($p < 0.0005$).



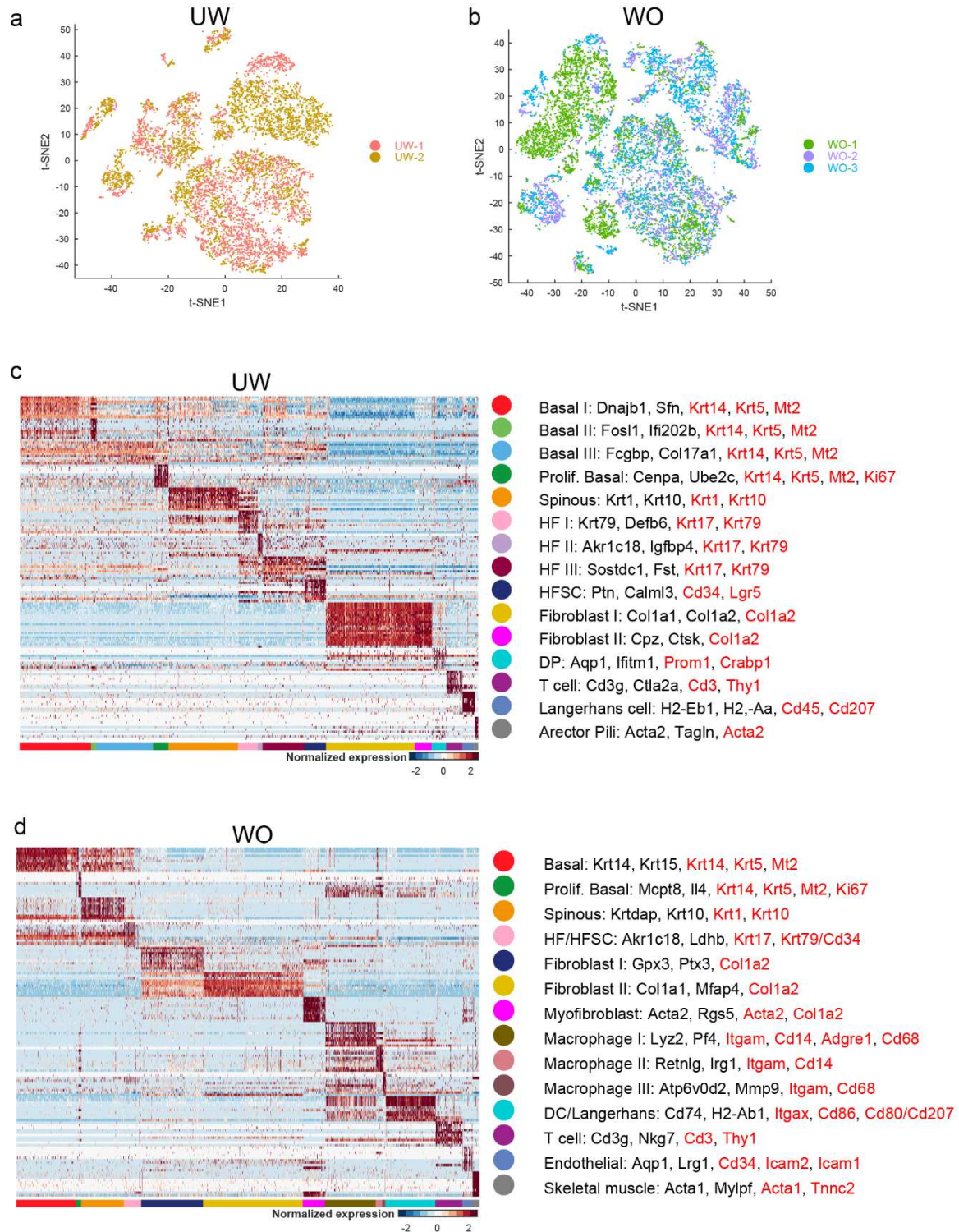
Supplemental Figure 4.1: Proliferation dynamics and quality control metrics

- (A) Proliferation dynamics in equivalent sample taken for scRNA-Seq. Yellow dashed line indicates wound margin.
- (B) Quality control metrics of UW and WO samples indicating the number of genes (nGene with 200-5000 range), number of UMIs (nUMI), and the percent mitochondrial genes (percent.mito under 10%).

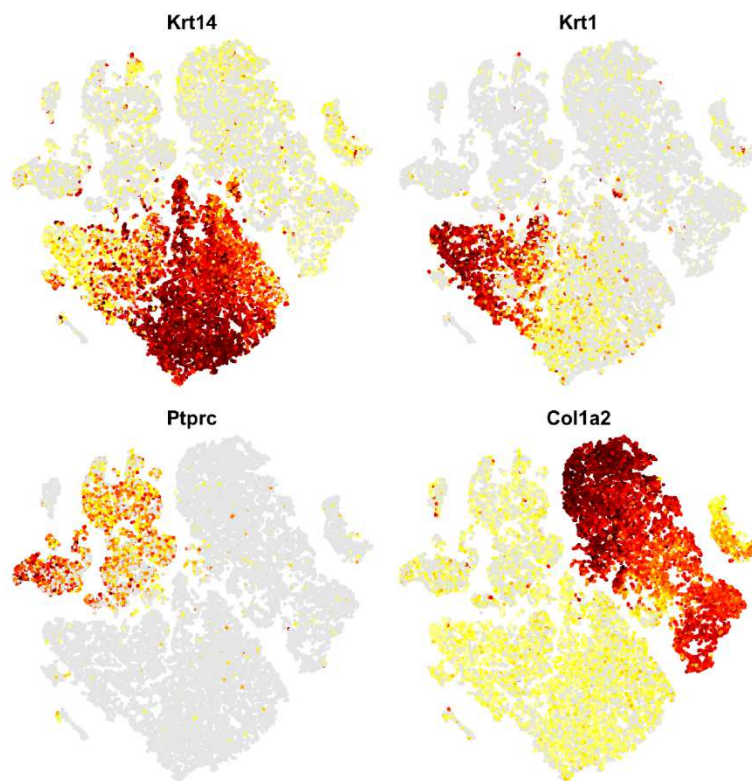


Supplemental Figure 4.2: Replicate IDs and associated marker genes with heatmaps

- (A) tSNE plot containing 2 samples from un-wounded skin that were aggregated and then batch corrected using CCA. Colors correspond to each replicate sample identified by a unique color identifier.
- (B) tSNE plot containing 2 samples from un-wounded skin that were aggregated and then batch corrected using CCA. Colors correspond to each replicate sample identified by a unique color identifier.
- (C) Heatmap for the top 10 genes enriched in each of the unique clusters from un-wounded skin. Genes listed in black represent the top 2 marker genes from each cluster where the genes listed in red represent the genes used in the final identification of the cluster cell type.
- (D) Heatmap for the top 10 genes enriched in each of the unique clusters from wounded skin. Genes listed in black represent the top 2 marker genes from each cluster where the genes listed in red represent the genes used in the final identification of the cluster cell type.

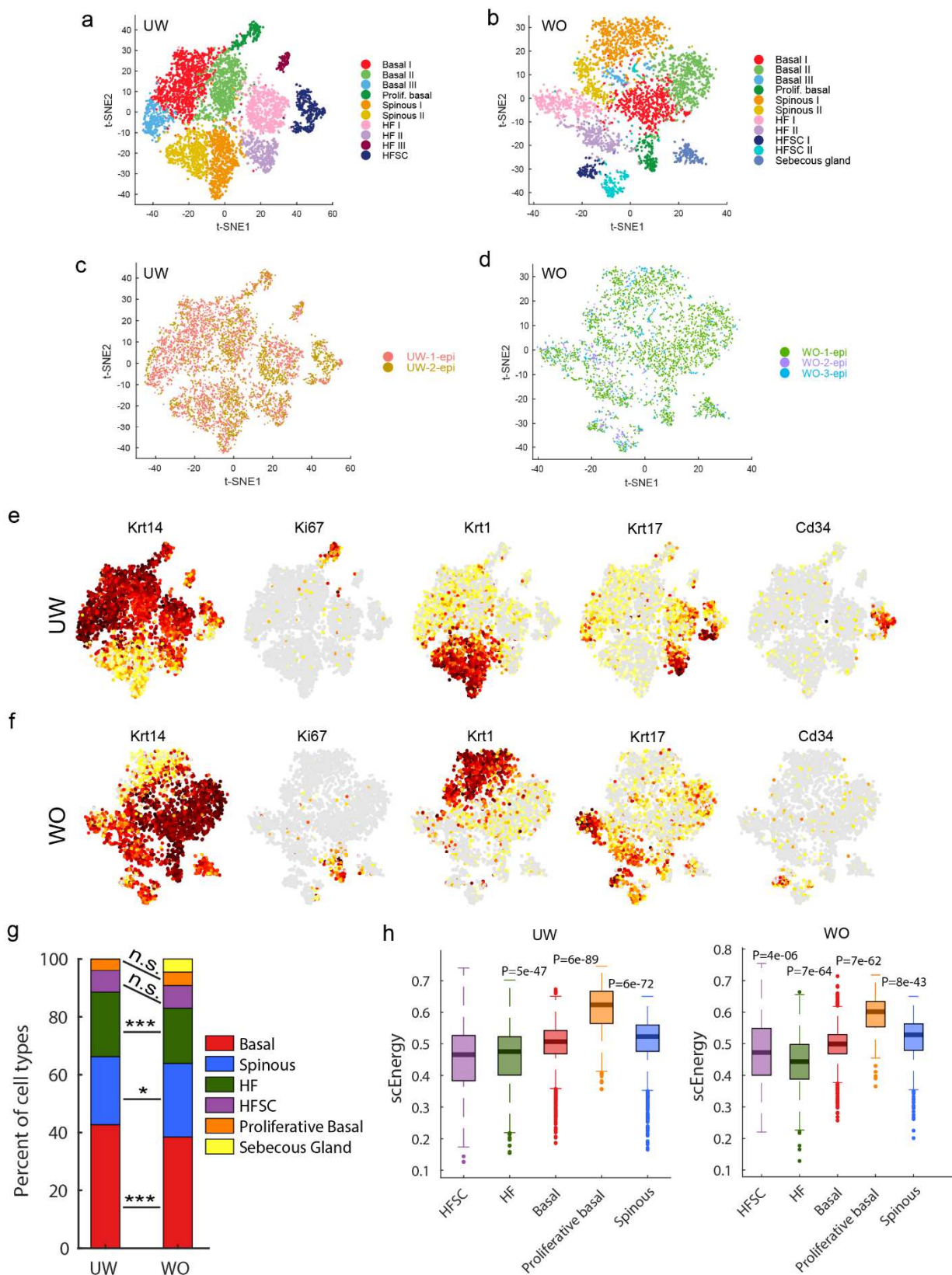


Supplemental Figure 4.3: Feature plots of major cell type populations containing all samples (2 UW and 3 WO)



Supplemental Figure 4.4: scRNA-Seq reveals minor changes in epithelial cellular makeup during wound healing

- (A) tSNE plot containing epithelial cells from 2 samples from un-wounded skin that were aggregated and then batch corrected using CCA.
- (B) tSNE plot containing epithelial cells from 3 samples from wounded skin that were aggregated and then batch corrected using CCA.
- (C) tSNE plot from (A) where colors correspond to each replicate sample identified by a unique color identifier.
- (D) tSNE plot from (B) where colors correspond to each replicate sample identified by a unique color identifier.
- (E) Feature plots highlighting genes from major epithelial cell types in UW sample.
- (F) Feature plots highlighting genes from major epithelial cell types in WO sample.
- (G) Bar graph representing the major epithelial cell type populations in the UW and WO samples. For statistical analysis, Chi-squared test was used ('*' = $p < 0.05$; '***' = $p < 0.0005$).
- (H) Boxplot indicating scEnergy values for clusters of cells from UW and WO samples containing epithelial cells from S4A and S4B, respectively (see Methods section).



Supplemental Figure 4.5: Associated marker genes with heatmaps for epithelial cells from UW and WO samples

- (A) Heatmap for the top 10 genes enriched in each of the unique epithelial clusters from un-wounded skin. Genes listed in black represent the top 2 marker genes from each cluster where the genes listed in red represent the genes used in the final identification of the cluster cell type.
- (B) Heatmap for the top 10 genes enriched in each of the unique epithelial clusters from wounded skin. Genes listed in black represent the top 2 marker genes from each cluster where the genes listed in red represent the genes used in the final identification of the cluster cell type.

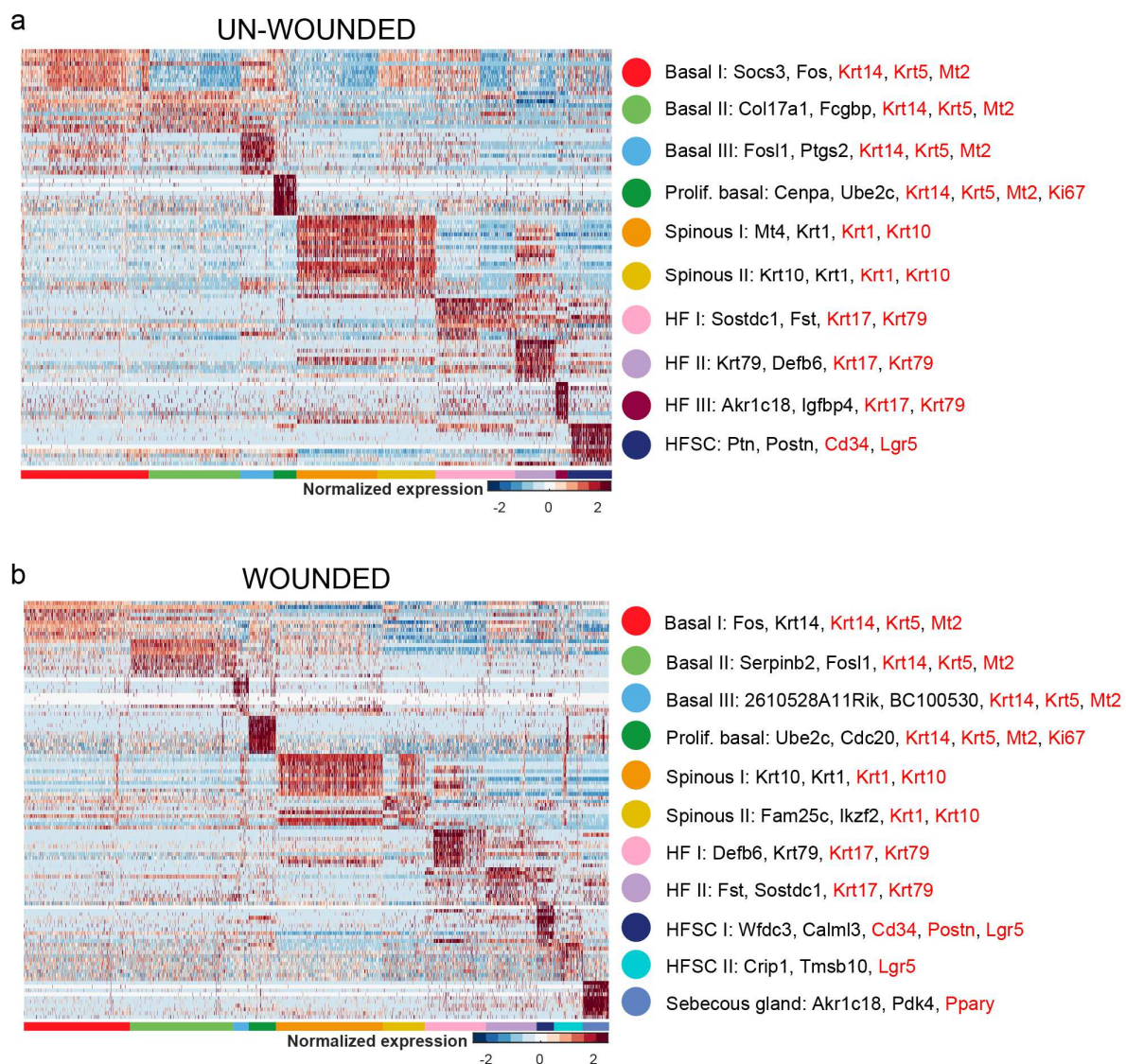
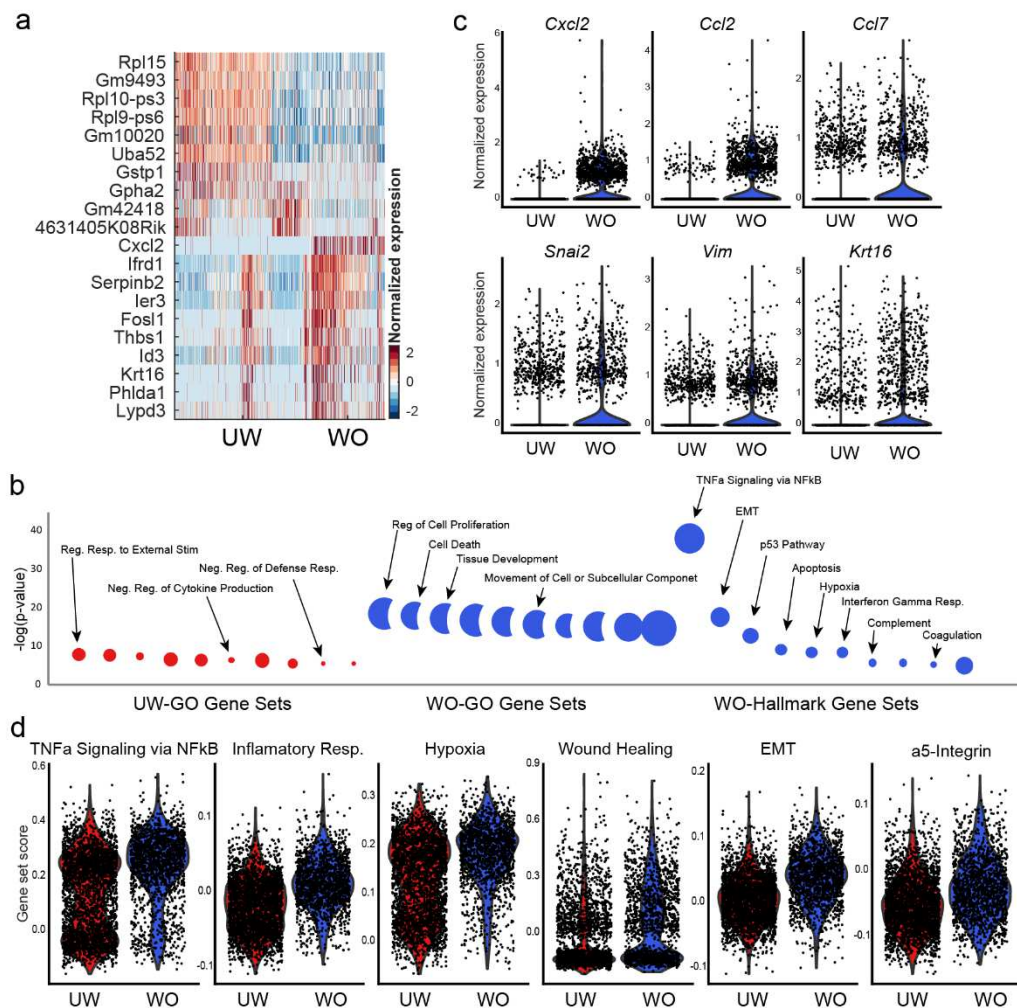


Figure 4.2: Wound epidermal basal cells show upregulated expression of inflammation-and migration-related genes

- (A) Heatmap showing the top 10 markers for basal cells from the UW and WO samples.
- (B) GO analysis of basal cells from UW and WO sample. GO Gene Sets and Hallmark Gene Sets represent two different gene sets where Hallmark Gene Sets are defined by fewer genes.
- (C) Violin plots showing expression of select genes from UW and WO basal cells.
- (D) Gene scoring analysis for various terms between UW and WO basal cells.



Supplemental Figure 4.6: Proliferative basal cells have dramatically distinct gene expression patterns compared to non-proliferative basal cells

- (A) PCA analysis of total basal cells (proliferative and non-proliferative) from UW and WO samples.
- (B) Feature plot utilizing PCA plot in (A) indicating the expression of proliferative marker Mki67 in a subset of cells.
- (C) PCA analysis of non-proliferative basal cells from UW and WO samples after removal of proliferative cells.

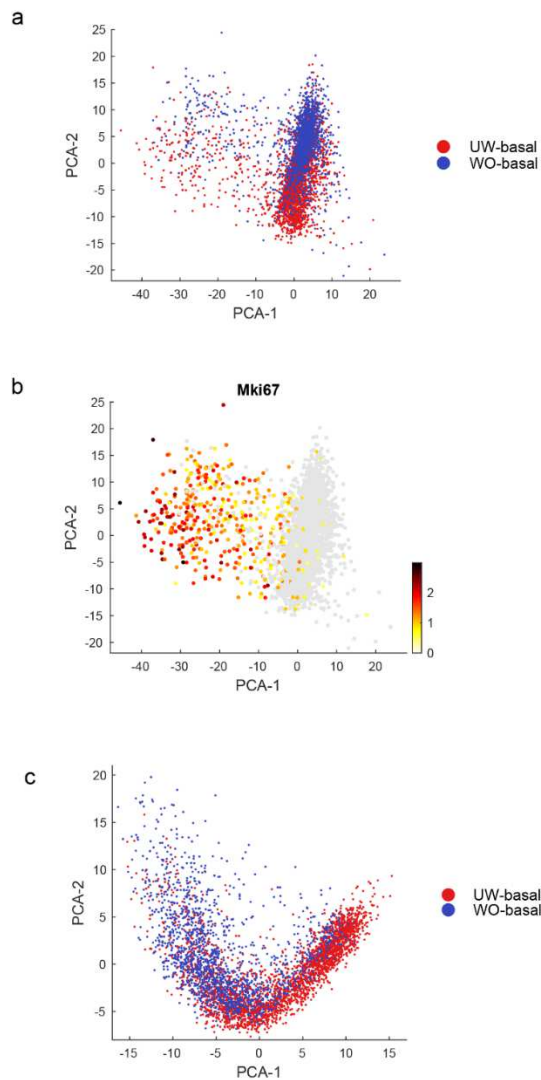
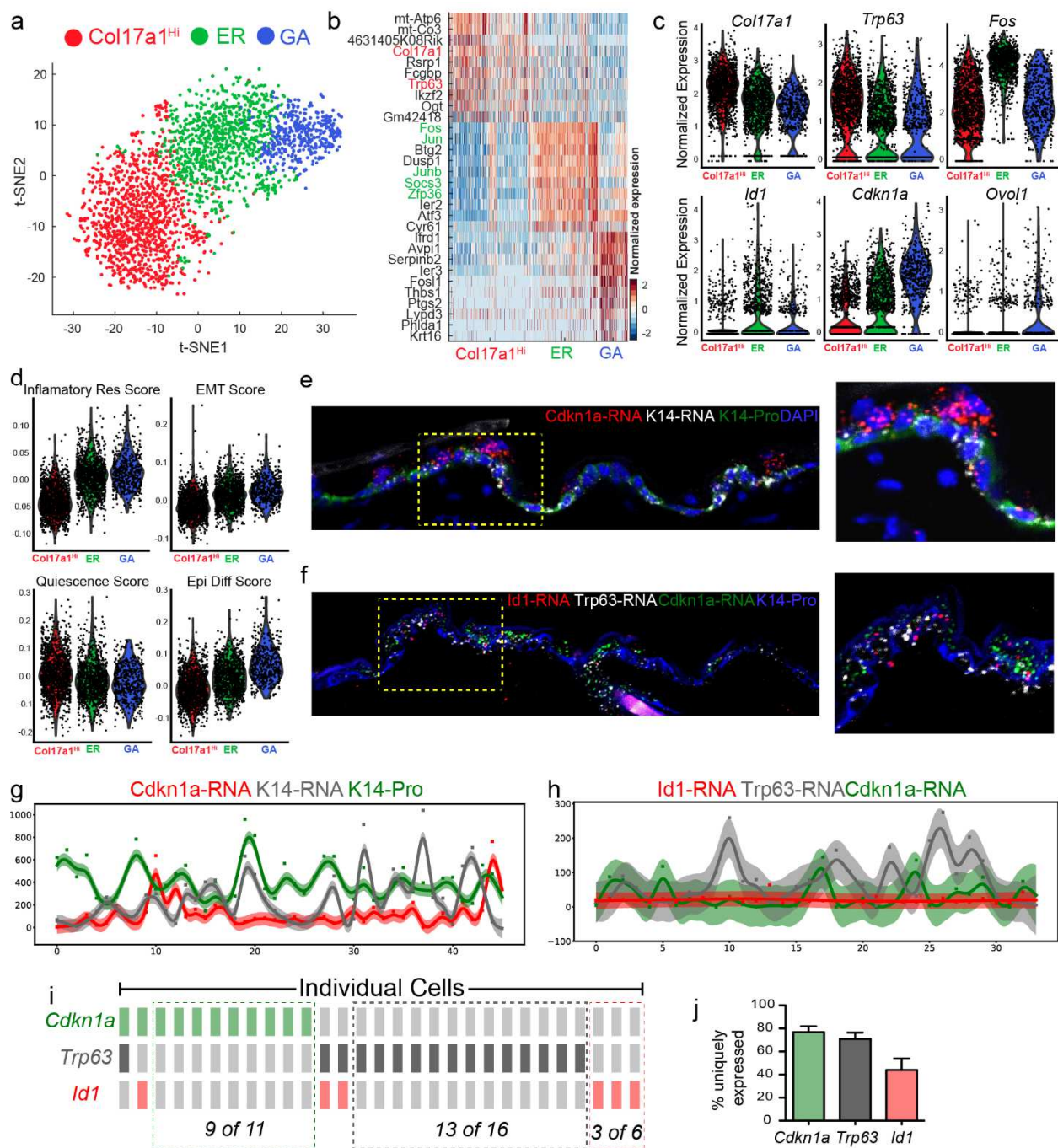


Figure 4.3: Three distinct non-proliferative basal cell subsets exist in un-wounded skin

- (A) tSNE plot of non-proliferative basal cells from UW sample. ER = early response, GA = growth arrested.
- (B) Heatmap of the different basal populations in (A).
- (C) Violin plots of key notable marker genes in each of the basal clusters from UW sample.
- (D) Gene scoring analysis for various terms between the different basal clusters from UW sample.
- (E) *Cdkn1a* and *Krt14* in situ hybridization by RNAScope with Krt14 indirect immunofluorescence. On right is enlarged image of boxed area.
- (F) *Cdkn1a*, *Trp63*, *Id1* in situ hybridization by RNAScope with K14 indirect immunofluorescence. On right is enlarged image of boxed area.
- (G) Quantification of fluoresce intensity of *Cdkn1a*, *Krt14*, and K14 within individual cells across all basal cells in representative section in sequential order. Each dot represents fluorescence of indicated transcript or protein. The curve represents a Gaussian Process Regression and a 95% confidence interval is shown as shaded area.
- (H) Quantification of fluoresce intensity of *Cdkn1a*, *Trp63*, and *Id1* within individual cells across all basal cells in representative section in sequential order. Each dot represents fluorescence of indicated transcript or protein. The curve represents a Gaussian Process Regression and a 95% confidence interval is shown as shaded area.
- (I) OncoPrint type representation of *Cdkn1a*, *Trp63*, and *Id1* expression within individual cells where a column represents an individual cell. A colored in rectangle indicates high expression of indicated gene. Ratio of exclusive expression of *Cdkn1a*, *Trp63*, and *Id1* in individual cells indicated on right.
- (J) Ratios of exclusive expression of *Cdkn1a*, *Trp63*, and *Id1* (n = 3 replicates). Error bars represent mean \pm SEM.



Supplemental Figure 4.7: Basal cell analysis in UW skin

- (A) Key marker genes enriched in the Col17a1^{Hi}, ER, and GA basal cell clusters.
- (B) LRC gene score for Col17a1^{Hi}, ER, and GA basal cell clusters.
- (C) GO analysis of UW basal clusters.
- (D) Local spatial autocorrelation analysis of RNAScope analysis of *Cdkn1a*, *Krt14*, and *Krt14*.
- (E) Local spatial autocorrelation analysis of RNAScope analysis of *Cdkn1a*, *Trp63*, and *Id1*.
- (F) Heatmap showing density estimation with dashed lines being cutoffs for binarization.

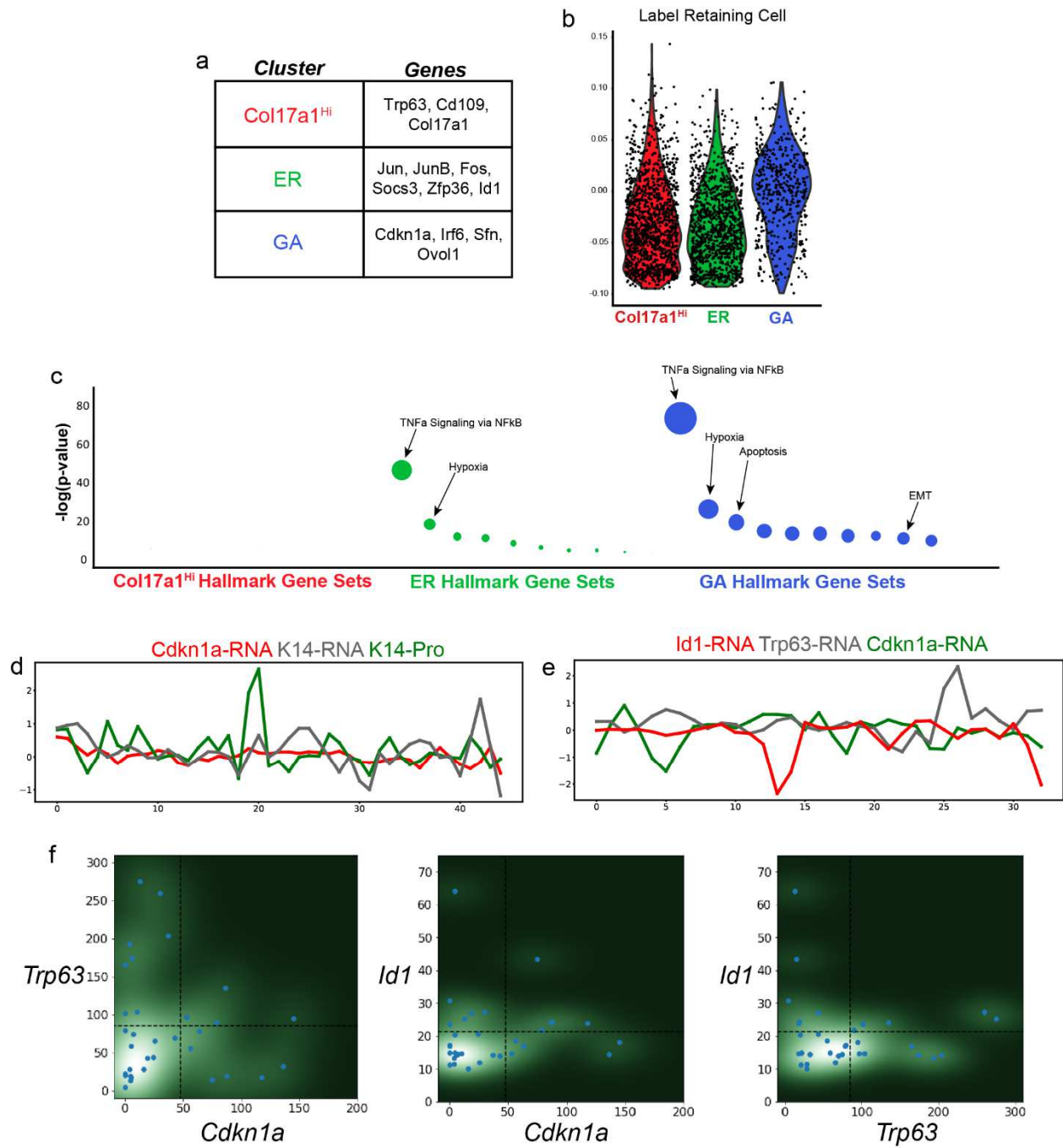
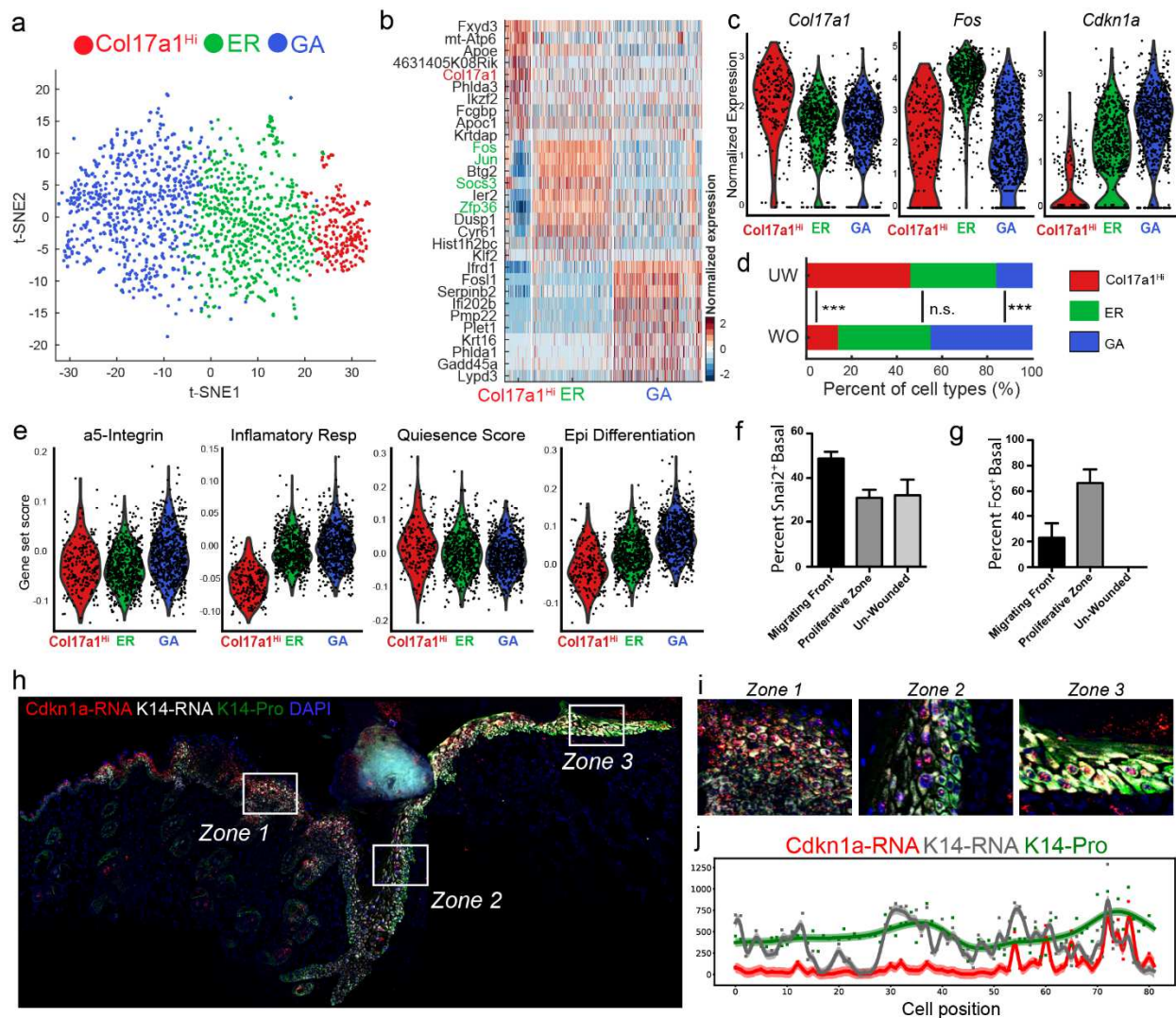


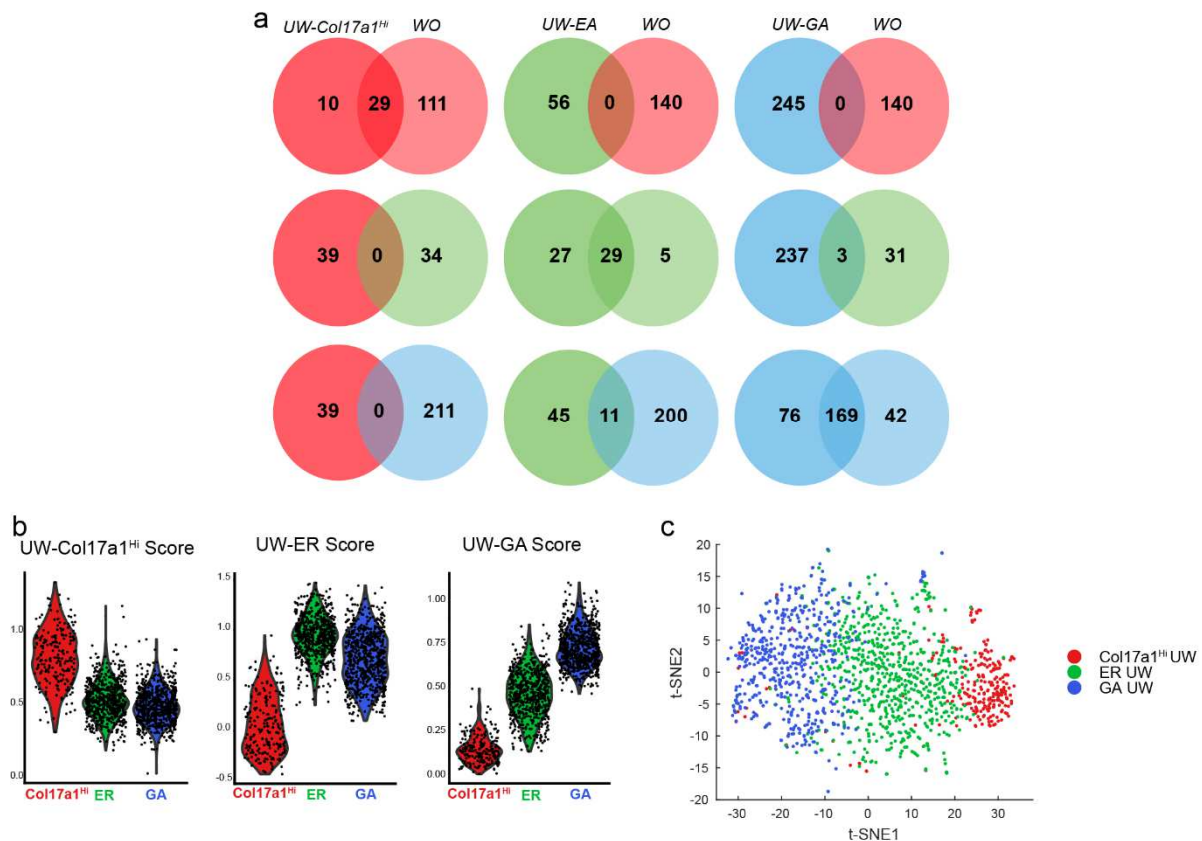
Figure 4.4: Alteration and spatial partitioning of basal cell subsets in wounded skin

- (A) tSNE plot of non-proliferative basal cells from WO sample. ER = early response, GA = growth arrested.
- (B) Heatmap of the different basal populations in (A).
- (C) Violin plots of key notable marker genes identified in UW sample in each of the different basal clusters from WO sample.
- (D) Percentage makeup of basal cell state in UW and WO samples. For statistical analysis, Chi-squared test was used ($p < 0.0005$).
- (E) Gene scoring analysis for various terms between the different basal cell clusters in the WO sample.
- (F) Quantification of Snai2⁺ cells within the basal layer of indicated regions.
- (G) Quantification of Fos⁺ cells within the basal layer of the indicated regions.
- (H) *Cdkn1a* and *Krt14* in situ hybridization by RNAScope with Krt14 indirect immunofluorescence.
- (I) Zoomed in regions of (H).
- (J) Quantification of fluorescence intensity of *Cdkn1a*, *Krt14*, and Krt14 within individual cells across all basal cells in representative section in sequential order from wound margin to wound tip. Each dot represents fluorescence of indicated transcript or protein. The curve represents a Gaussian Process Regression and a 95% confidence interval is shown in shaded area.



Supplemental Figure 4.8: Basal cell states are similar in UW and WO samples

- (A) Marker gene overlap between the Col17a1^{Hi}, ER, and GA basal cell clusters from UW samples and basal cell clusters from basal cell clusters identified in WO sample.
- (B) Scoring different basal cell clusters from WO sample using marker genes from basal cell cluster from UW samples.
- (C) Random forest classification of basal cells from WO sample using basal cells from UW sample as training class.



Supplemental Figure 4.9: GO and marker gene analysis of basal cells from WO sample

- (A) GO analysis of WO basal cell clusters.
- (B) Diagram of equivalent wound with migrating front and proliferative zone.
- (C) Known marker genes that have specific localization in epithelial cells around wound.
- (D) Indirect immunofluorescence for Snai2 in different regions of wound.
- (E) Indirect immunofluorescence for Fos in different regions of the wound.
- (F) Local spatial autocorrelation analysis of RNAScope analysis of *Cdkn1a*, *Krt14*, and *Krt14*.

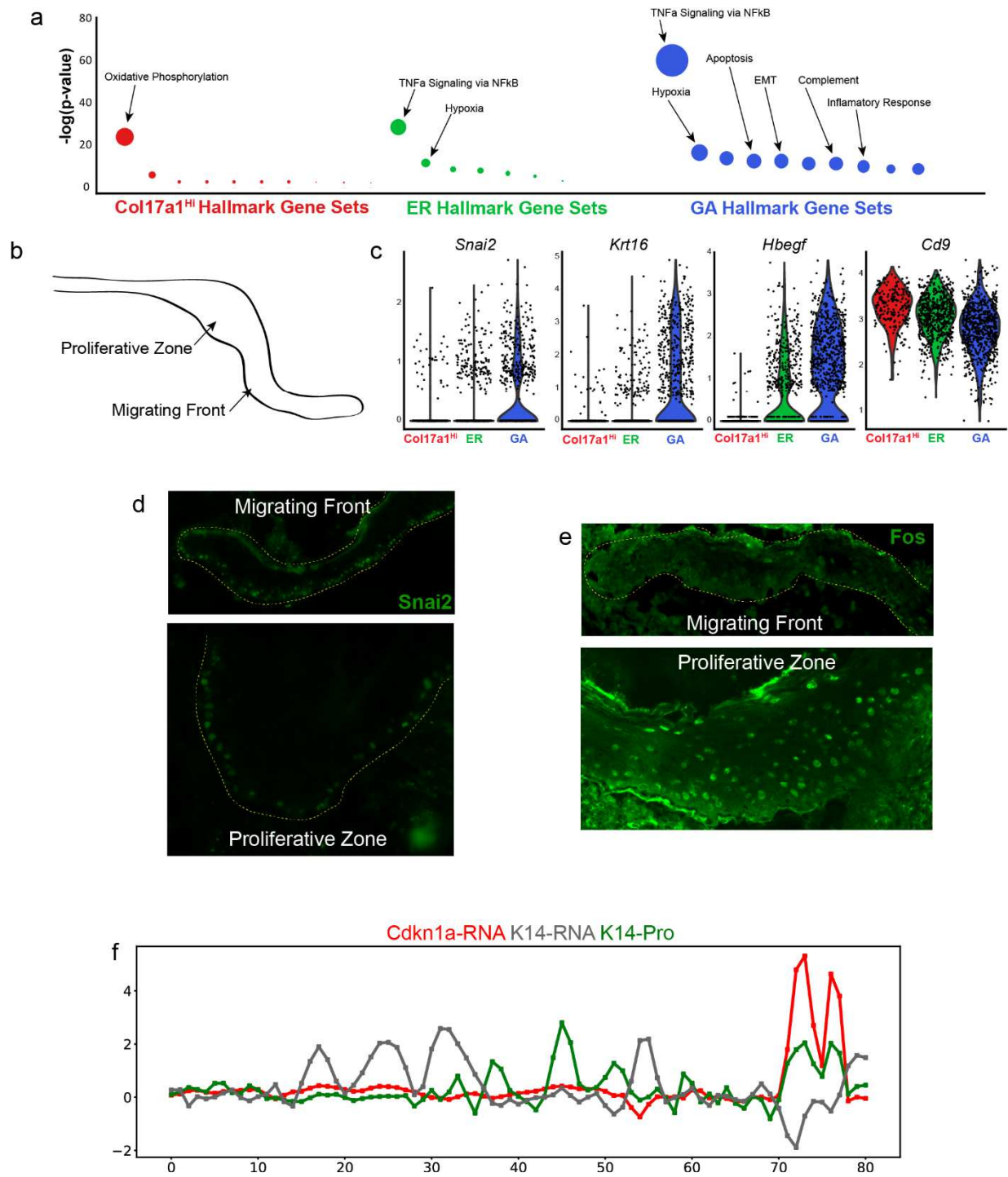
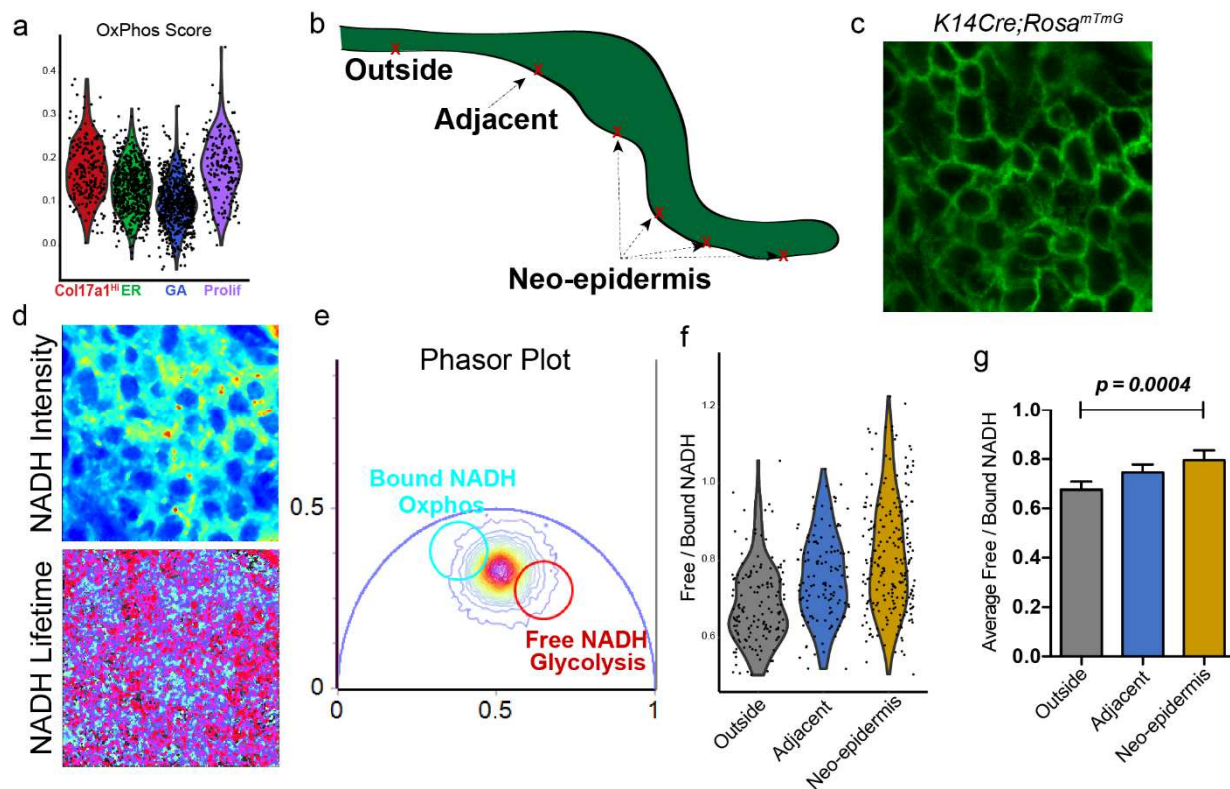


Figure 4.5: Metabolic heterogeneity in basal cells of the normal and wounded skin

- (A) Gene scoring of oxidative phosphorylation in all basal cells from WO sample (proliferative and non-proliferative).
- (B) Theoretical diagram of a histological section through a wound with labeled regions of the neo-epidermis to be probed.
- (C) Representative image of epidermal cells in wound as indicated by GFP reporter.
- (D) Representative images of in vivo genetic fluorescence labeling, NADH signal, and NADH lifetime signal.
- (E) Representative phasor plot.
- (F) Violin plot indicating free/bound ratios of all individual cells from all samples.
- (G) Quantification of the free/bound ratio at distinct regions within and outside the neo-epidermis.



Supplemental Figure 4.10: Spatial localization of basal cells during repair dictates metabolic state

(A) Gene scoring of oxidative phosphorylation in all basal cells from UW sample (proliferative and non-proliferative).

(B) Violin plot for *Hif1a* expression in basal cells from WO sample.

(C) Violin plot for *Hif1a* expression in basal cells from the UW sample.

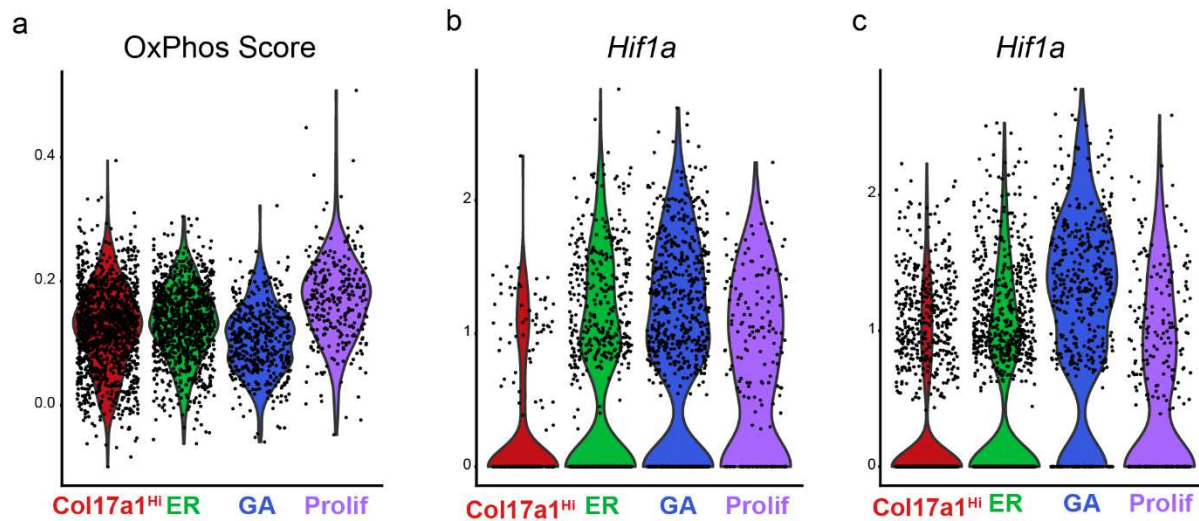
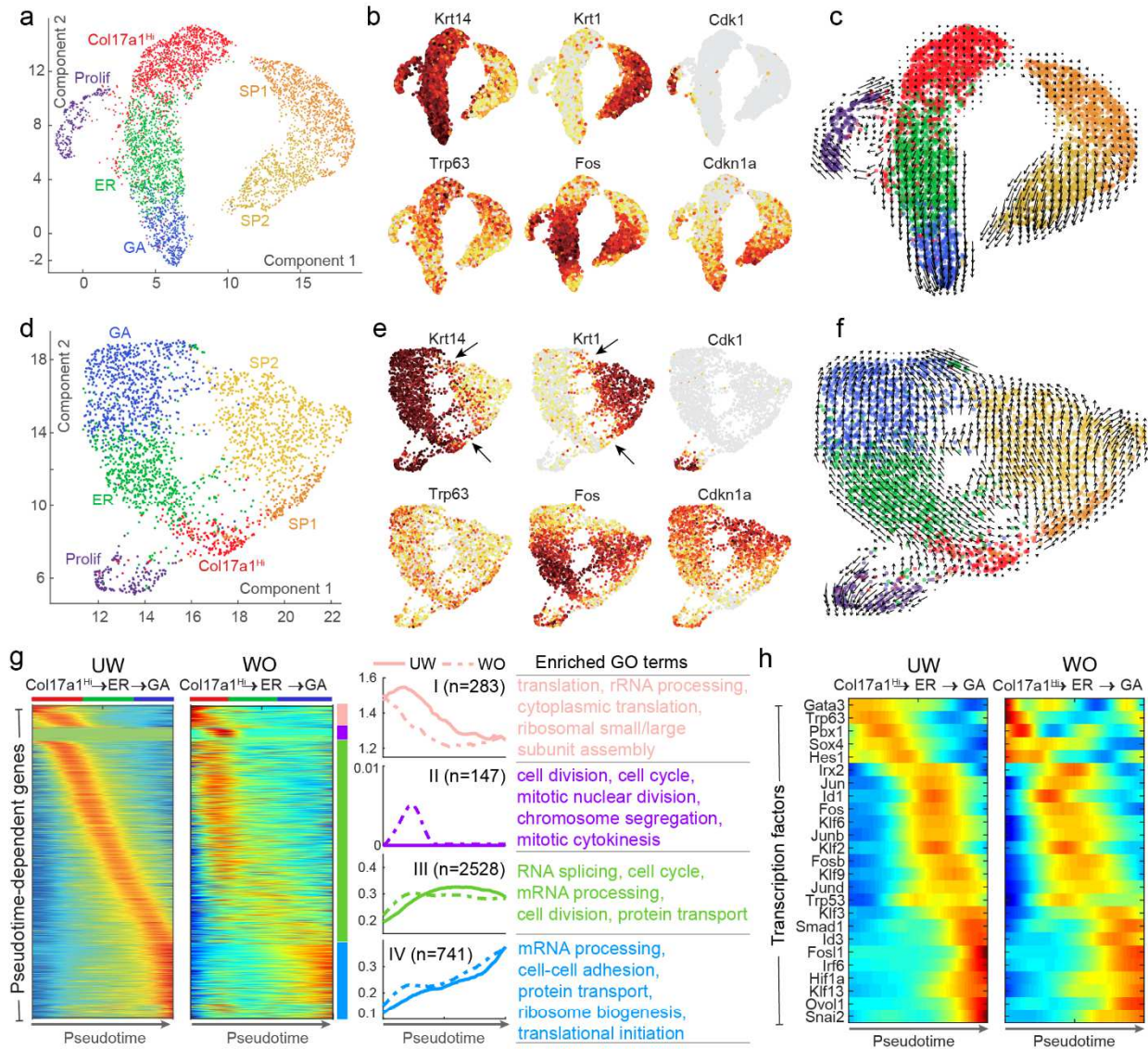


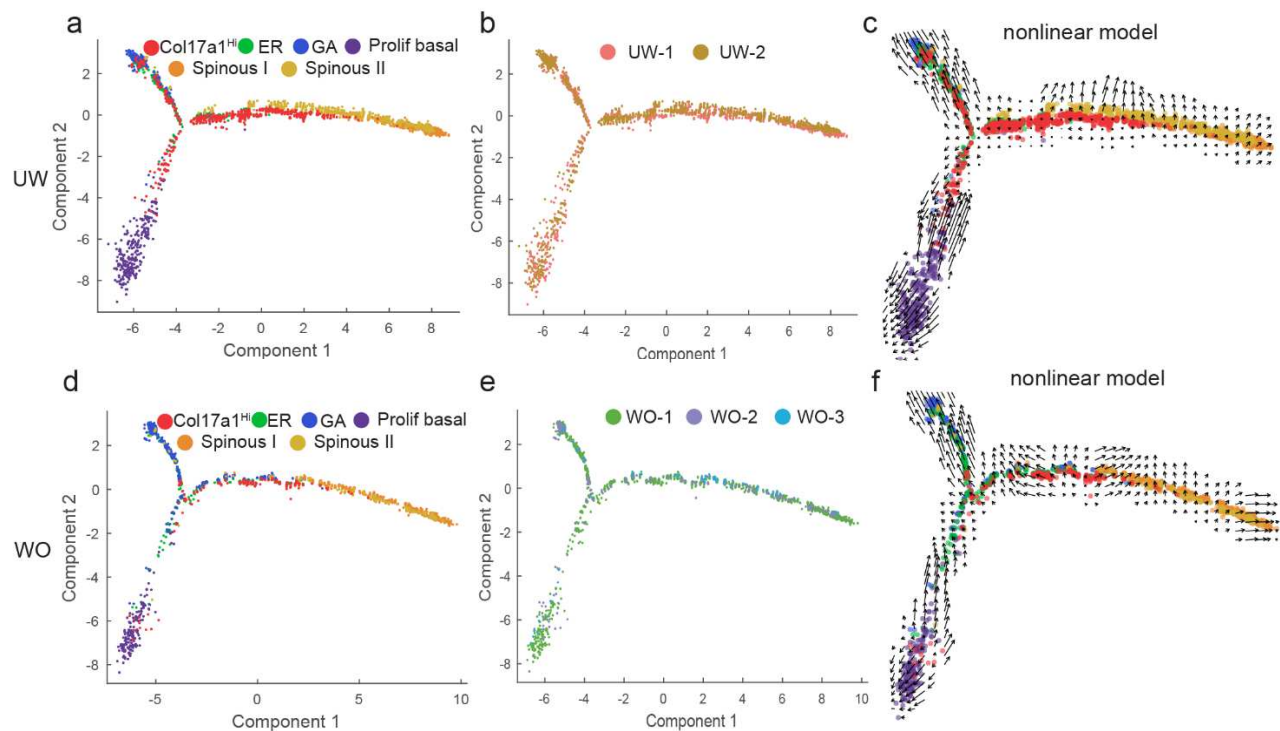
Figure 4.6: Pseudotemporal ordering and RNA velocity analysis reveal three different programs

- (A) UMAP dimensional reduction of all basal populations (proliferative and non-proliferative) with spinous cell populations from UW.
- (B) Feature plots of (A) for key genes.
- (C) RNA velocity overlay of (A).
- (D) UMAP dimensional reduction of all basal populations (proliferative and non-proliferative) with spinous cell populations from WO.
- (E) Feature plots of (D) for key genes.
- (F) RNA velocity overlay of (D).
- (G) Pseudotemporal dynamics of the identified 3,699 pseudotime-dependent genes (from UW sample) along the Col17a1^{Hi} to GA path in the UW and WO samples. Cell identity (Col17a1^{Hi}, ER or GA) was indicated on the top of each heatmap generated by the smoothed, normalized gene expression (For the colormap, blue and red colors indicate the low and high expression, respectively.). Each row/gene was normalized to its peak value along the pseudotime. Distinct gene clusters during pseudotime represented by pink, purple, green, and blue bars. The average gene expression of each gene cluster was shown for UW (solid line) and WO (dashed line) samples, respectively. The number of genes in each gene cluster was indicated. GO analysis of these different clusters is listed.
- (H) Subsets of transcription factors and with their corresponding pseudotemporal dynamics in both UW and WO basal cells along the Col17a1^{Hi} to GA path.



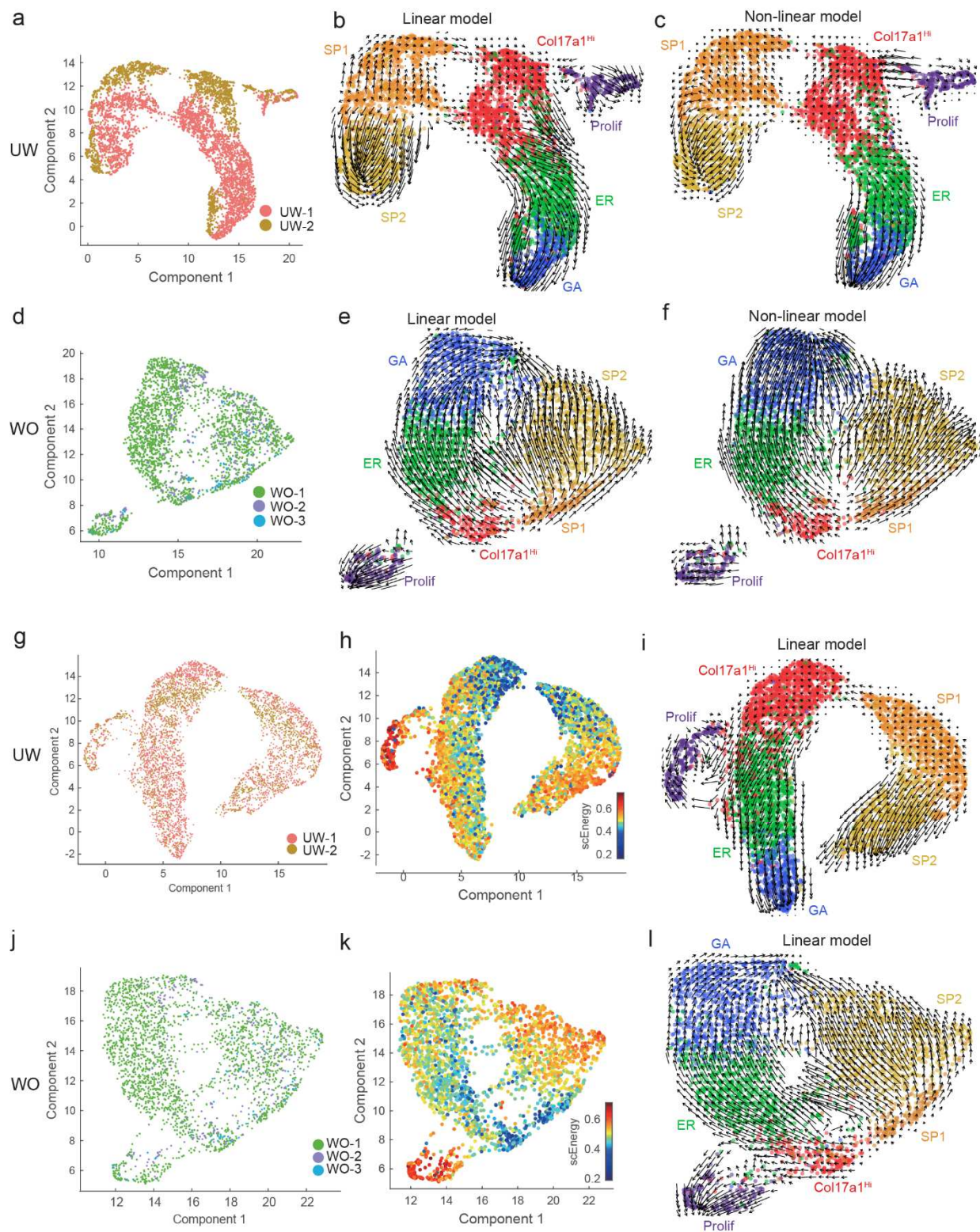
Supplemental Figure 4.11: Monocle lineage analysis in UW and WO skin

- (A) Lineage analysis of basal cells (proliferative and non-proliferative) and spinous cells in UW sample using Monocle.
- (B) Monocle analysis as in (A) but colored by sample replicate.
- (C) Monocle analysis as in (A) but with RNA Velocity projection.
- (D) Lineage analysis of basal cells (proliferative and non-proliferative) and spinous cells in WO sample using Monocle.
- (E) Monocle analysis as in (D) but colored by sample replicate.
- (F) Monocle analysis as in (D) but with RNA Velocity projection.



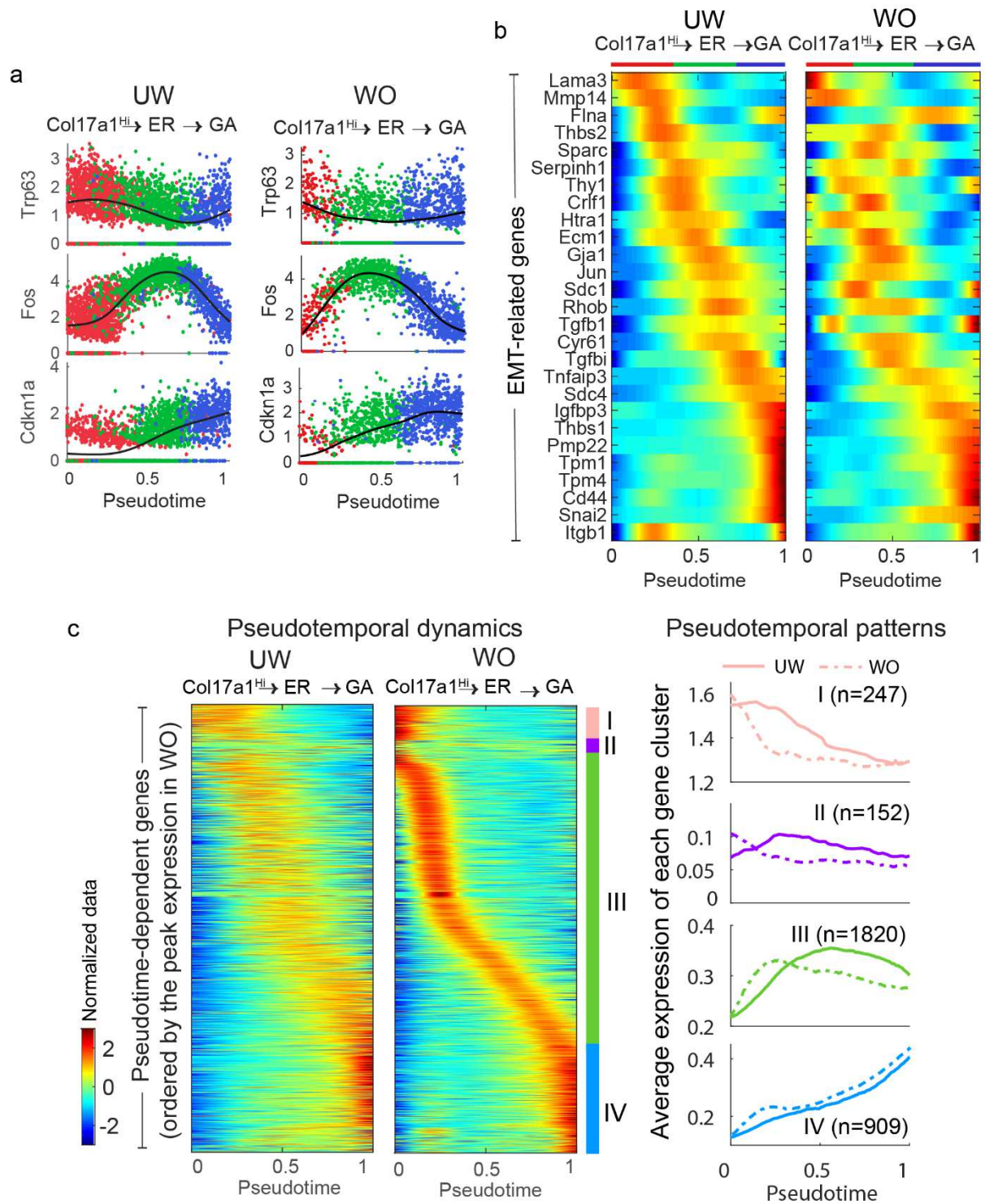
Supplemental Figure 4.12: Lineage analysis by scEpath and RNA Velocity

- (A) Initial UMAP dimensional reduction for UW sample with cells identified by their replicate identity.
- (B) Initial UMAP dimensional reduction for UW sample with all basal populations (non-proliferative and proliferative). RNA velocity overlay of (A) utilizing the linear model.
- (C) RNA velocity similar to (B) using a non-linear model.
- (D) Initial UMAP dimensional reduction for WO sample with cells identified by their replicate identity.
- (E) Initial UMAP dimensional reduction for WO sample with all basal populations (non-proliferative and proliferative). RNA velocity overlay of (D) utilizing the linear model.
- (F) RNA velocity similar to (E) using a non-linear model.
- (G) UMAP dimensional reduction for UW sample with cells identified by their replicate identity after batch correction.
- (H) UMAP dimensional reduction for UW sample similar to (G) with scEnergy indicated.
- (I) RNA velocity overlay for (G) using a linear model.
- (J) UMAP dimensional reduction for WO sample with cells identified by their replicate identity after batch correction.
- (K) UMAP dimensional reduction for UW sample similar to (J) with scEnergy indicated.
- (L) RNA velocity overlay for (J) using a linear model.



Supplemental Figure 4.13: Pseudotemporal changes in gene expression

- (A) Dynamic changes in gene expression of *Trp63*, *Fos*, *Cdkn1a*, and *Cdk1* over pseudotime down the Col17a1^{Hi} to GA and the Col17a1^{Hi} to proliferative basal paths.
- (B) Subsets of EMT-related genes with their corresponding pseudotemporal dynamics in both UW and WO basal cells along the Col17a1^{Hi} to GA path.
- (C) Pseudotemporal dynamics of the identified 3,128 pseudotime-dependent genes (from WO sample) along the Col17a1^{Hi} to GA path in the UW and WO samples. Cell identity (Col17a1^{Hi}, ER or GA) was indicated on the top of each heatmap generated by the smoothed, normalized gene expression (For the colormap, blue and red colors indicate the low and high expression, respectively.). Each row/gene was normalized to its peak value along the pseudotime. Distinct gene clusters during pseudotime represented by pink, purple, green, and blue bars. The average gene expression of each gene cluster was shown for UW (solid line) and WO (dashed line) samples, respectively. The number of genes in each gene cluster was indicated.



CHAPTER 5: Conclusions and Perspectives

Overview

The mouse epidermis and HF represent leading models in the field of epithelial stem cell biology (Blanpain and Fuchs 2014). In this work, I utilized the mouse epidermis and HF models, addressing questions surrounding both the homeostatic maintenance of the tissue via their putative epithelial stem cell populations and subsequently how they respond in the context of wound healing to facilitate repair. In both these contexts, epithelial stem cells are integral to facilitate tissue maintenance and repair. I took a multi-scale approach including (1) a whole skin analysis to understand the difference in cellular dynamics between wounded and un-wounded skin, focus on the dynamics and heterogeneity of EpdSCs, and (2) identification of a key EMT transcriptional circuit that regulates epithelial stem cell dynamics during wound healing and HF regeneration. For the whole skin approach, I utilized scRNA-Seq to transcriptionally profile all cells in un-wounded (UW) and wounded (WO) skin. From there I subsetting out basal/EpdSCs, for further transcriptional analysis and subsequent identification of EpdSC heterogeneity. In the other work, I explored the function of *Ovol2*, a known transcriptional repressor of EMT. I reported that loss of *Ovol2* leads to defects in HF regeneration as well as during epidermal wound healing (Haensel et al., 2018). These defects are attributed in part to loss of directional cell migration, a process regulated by the *Ovol2*-*Zeb1* transcriptional circuit. In summary, I successfully studied several aspects of skin epithelial biology with particular emphasis on epidermal homeostasis, epidermal repair, and HF regeneration.

Chapter 3

In chapter 3 of the dissertation, I include published work (*Haensel et al., 2018 EMBO Reports*), which focuses on the role of EMT-inhibiting TF Ovol2 in both HF regeneration/cycling as well as its role in epidermal repair (Haensel et al., 2018). I show through a number of *in vivo* and *in vitro* experiments, that the Ovol2-Zeb1 transcriptional circuit is central to the regulation of directional migration of epithelial cells (Haensel et al., 2018). This regulation is predominant during both HF regeneration, as loss of Ovol2 leads to delays in HF cycle, and in the context of epidermal repair, as Ovol2 loss leads to defective wound healing (Haensel et al., 2018).

Although EMT is typically thought of in the context of cancer metastasis or embryonic development, recent evidence has pointed to EMT-like being present in committed epithelial tissues (Sha et al., 2019). Previous work has shown the importance of Ovol TFs and their prominence in restricting EMT-like events during epidermal morphogenesis (Lee et al., 2014). My work builds on this notion that EMT regulation is functionally critical to the regeneration of adult epithelial tissues such as the HF but also re-addressed its role in epidermal repair (Haensel et al., 2018). *In vivo* live imaging strikingly illustrated the migratory behavior of keratinocytes during both HF regeneration and during epidermal repair suggesting that there are indeed times where a relaxation of the rigid epithelial phenotype would be desirable to promote a regenerative- or repair-type of event (Rompolas et al., 2012; Rompolas et al., 2013; Park et al., 2017). What has become more clear though is that relaxation doesn't equate to loss, as previous work and this work indicate that during epithelial development, adult regeneration, and repair, loss

of negative regulators of EMT leads to defects in regenerative and repair events (Lee et al., 2014; Haensel et al., 2018; Watanabe et al., 2014).

Extensive work has identified that the EMT-inducing transcription factor Snai2/Slug is focal for promoting the migratory phenotypes observed in keratinocytes during wound healing, but little is known what prevents these cells from becoming full mesenchymal type cells (Haensel and Dai 2018; Arnoux et al., 2005; Hudson et al., 2009). My work highlighted the role of Ovol2 as a vital component to restrict the mesenchymal tendencies of epidermal keratinocytes during wound healing (Haensel et al., 2018). To further test the roles of EMT-regulating TFs, both activators (such as Snai2, Zeb1, Twist1) and repressors (such as Ovol2 and Grhl3), utilizing an intravital approach to monitor the movement of the epidermal keratinocytes would be extremely useful (Park et al., 2017). These studies would be able to not only monitor the migration rate but also examine the directionality of the keratinocytes. This approach would allow us to further validate our *in vitro* live imaging results but also continue to explore the contribution of other EMT transcription factors.

Although fairly intuitive in the context of wound healing, whether EMT plays roles in regenerative events is less obvious. Briefly mentioned above, during HF regeneration, live imaging indicates that epithelial components of the HF adopt migratory features as they actively proliferate and migrate down into deeper regions of the dermis (Rompolas et al., 2012; Rompolas et al., 2013). Our work suggested that a disruption in the transcriptional control of EMT during HF regeneration leads to defective anagen progression (Haensel et al., 2018). Disruption did not lead to a failure of HG activation, but rather there appeared to be defects in anagen progression leading to more subtle

defects in HF cycling (Haensel et al., 2018). Although I was able to show the importance of the *Ovol2-Zeb1* transcriptional circuit *in vitro* using Bu-HFSCs, to further this work, it would be important to generate mice to simultaneously delete *Ovol2* and *Zeb1* in an *in vivo* mouse model in order to show a rescue of HF cycling. Better yet, it would be valuable to monitor these alterations (defects and potential rescues) in a similar *in vivo* imaging setting.

In multiple cases, enhanced EMT-like migratory features are associated with reduced proliferation (Haensel et al., 2018). These defects were observed both during epidermal wound healing as well as *in vitro* cell culture models for NBPKs and Bu-HFSCs deficient for *Ovol2*. It is a well observed and accepted phenomenon that EMT is associated with reduced proliferation and that MET can even promote proliferation (Nieto et al., 2016). It would be particularly interesting if I could further examine this connection between proliferation and EMT. Of particular interest was our *in vitro* Bu-HFSC cultures, which were monitored by live imaging. I found an increase in 'Type-2' divisions, which are characterized by excessive cell rounding and at times, defective cytokinesis (Haensel et al., 2018). Further work could be done to (1) determine whether there are alterations in spindle orientations leading to this defective division, (2) whether these defects are observed *in vivo*, (3) whether these types of divisions are generalizable to other contexts where EMT is modulated or if this is an *Ovol2* specific phenotype, and (4) whether *Zeb1* depletion could rescue the division behavior in the *Ovol2*-deficient cells.

In a clinical context, this work provides potentially relevant considerations when approaching wound care. Perhaps most relevant would be in the context of diabetes where foot ulcers are quite common and characterized by their inability to effectively heal due to

failed migration of the keratinocytes (Brem and Tomic-Canic 2007). In the treatment of wounds, our data would suggest if the goal was to induce migration of keratinocytes, it would be important to consider how enhanced migration might influence the directional movement of the keratinocytes. To further our understanding on how modulation of *Ovol2* as well as other EMT TFs could potentially regulate the migratory abilities of keratinocytes in the context of diabetes, I could conduct wound healing studies using a diabetic mouse model or high fat diet model where EMT regulators (*Ovol2* or *Snai2*) have been lost.

Chapter 4

In chapter 4, I took a global approach capturing total cells from UW and WO skin for scRNA-Seq. At a global level, the major changes in cellular compositions include increased numbers of immune cells and fibroblasts in the wounded sample. Although I capture total cells (epidermal, HF-associated, immune, and fibroblast), major focus is on the EpdSCs of the epidermis. As previously mentioned, these EpdSCs are the key drivers of epidermal homeostasis and play crucial roles in re-establishment of the barrier after wounding (Gurtner et al., 2008; Haensel and Dai 2018). I transcriptionally profiled these EpdSCs, identify heterogeneity, and compare/contrast the EpdSCs found in UW and WO skin. After computationally subsetting basal cells from UW and WO samples, I made a direct comparison of gene expression between total basal cells from the UW and WO samples. This analysis did not generate much surprise as I noted the enhanced gene expression of both migratory and immune-related genes in the WO sample.

The notion that basal cell heterogeneity exists and that there is some functional hierarchy within the epidermis has existed for some time (Liu et al., 2019; Mascré et al.,

2012; Sada et al., 2016; Gonzales and Fuchs 2017). These studies have beautifully utilized lineage tracing strategies but whether these experiments are generalizable to the entire epidermis at a global level is not clear. Our work identifies three key non-proliferative (Col17a1^{Hi}, ER, and GA) basal cell states, which I go on to validate in situ. Coupled with lineage analysis, I find that the Col17a1^{Hi} population represents the population at the start of pseudotime indicating that this population might be the most primitive stem-like cell within the epidermis. This Col17a1^{Hi} population also has the highest expression of *Col17a1*, a desmosome gene that helps with attachment to the basement membrane. Interestingly, recent lineage tracing studies of this population find that Col17a1⁺ clones tend to outcompete Col17a1⁻ clones, eventually overtaking the entire epidermis, which indicates that these cells have the most potential and are likely the most primitive stem-like cell in the epidermis (Liu et al., 2019). To follow up on this observation, it would be important to co-stain for *Trp63* and *Col17a1* to then show that these genes are indeed co-expressed. To further our understanding of this potential lineage hierarchy that exists in the epidermis, lineage tracing of the Col17a1^{Hi} basal cell cluster would be the natural initial step. As our computational lineage predictive tools suggest a hierarchy within the different basal cell states, coupling lineage tracing with the functional validation of this hierarchy could be accomplished via assessing the potential of cells from each of these states. If sorting or enriching for these different basal cell states was possible, I could subject these cells to various in vitro clonal growth assays to assess stem potential. This could be achieved by identifying cell surface markers that either enrich or de-enrich for the different basal cell populations.

My data suggests that a similar heterogeneity exists in the WO sample but at different proportions. Although within the UW sample, there may be some spatial patterning that currently remains unclear, within the WO sample, I was able to roughly map back the different basal cell subsets. Subsequent lineage analysis showed similar results as the UW sample. Beyond the confirmation of the existence of the different basal subsets, our *in situ* analysis identified dynamic expression of *Krt14* throughout the epidermis. At the protein level, the levels of Krt14 does not dramatically change throughout the epidermis. At the RNA level, it would be particularly interesting to go back *in situ* and carefully stain for and quantify other keratinocyte markers such as *Krt1* to examine patterns within the normal epidermis. This *in situ* technique appears much more sensitive than traditional methods allowing for more quantifiable analysis. It would be interesting to compare ratios of *Krt14/Krt1* and their spatial localizations within the epidermis. A whole-mount type of approach would be useful in this case in order to get a 3D spatial map of the entire epidermal landscape rather than through a traditional section. This type of data would indicate how differentiation dynamics fluctuate throughout the epidermis, such as near HFs or if there is distinct organization of pockets/zones of differentiation.

Within the WO sample, it is clear there was an expansion of *Krt14* expressing cells even in clearly suprabasal positions. This raises the possibility that wounding induces fluctuations in the differentiation potential within the epidermis. Again, staining for both *Krt14* and *Krt1* would allow for determination of whether these cells in the suprabasal positions are both *Krt14+* and *Krt1+* or if these cells are just an additional layer of cells that are strictly transcriptionally basal. It is clear from the lineage analysis that when I

incorporate RNA velocity, the dynamics (as revealed by vectors) is more fluid and tracks seem to toggle between basal and spinous cells. Although more work is needed, it is tempting to attribute this expansion of *Krt14*⁺ cells in suprabasal positions to this enhanced fluidity observed by RNA velocity.

As I captured total cells (epithelial, fibroblast, and immune cells), further work is needed to explore the changes in fibroblast heterogeneity and immune cell populations during wound healing (Gurtner et al., 2008). As computational models develop, models incorporating methods for capturing cell-cell communications via known receptor/ligand pairs would become very useful in large data sets containing multiple cell types. During wound healing, damage signals from keratinocytes must be sent to other cell types such as the immune cells in order to facilitate clearance of any foreign pathogens (Gurtner et al., 2008; Haensel and Dai 2018). Mapping the presence and degree of these different communications via receptor/ligand pair analysis along with highlighting the wound-specific communications (relative to UW skin) that arise would prove very informative. Additional WO timepoints could also be analyzed eventually leading back to fully healed skin allowing for a clear picture of the cellular compositions and communications during the entire wound healing time course. To date I have two un-wounded samples, three samples from four days after wounding, and two samples from seven days after wounding. Beyond simply profiling, these types of cell-cell communication analysis tools would be of particular use to better characterize diabetic wound healing. Diabetic wounds would be ideal models to utilize these tools as they are generally characterized by poor wound closure associated with both reduced migration of keratinocytes as well a large inflammatory response (Brem and Tomic-Canic 2007). Mapping, characterizing, and

comparing the major types of cellular communication between normal and diabetic wounds would prove informative.

Finally, the observation regarding the metabolic heterogeneity and spatial localization during epidermal wound healing raises a number of intriguing questions. Wounds are known to be hypoxic environments, thus our observations that the migrating front prefers an aerobic metabolic pathway is well justified. Even in regions outside the wound, it appears that there exists some metabolic heterogeneity in basal cells. It would be interesting to examine large regions of normal skin and determine whether this heterogeneity has any type of particular patterning.

Overall, I present clear descriptions and work towards a better understanding of normal skin homeostasis and the dynamic changes incurred during repair. I take a multi-scale approach, describing these changes at a global level using scRNA-Seq, providing insight on the major alterations in gene expression within the EpdSCs, describe the global changes in cellular heterogeneity as well as within the EpdSCs, and clearly describe the lineage dynamics. Finally, my work described a key transcriptional circuit between EMT-TF regulators, *Ovol2* and *Zeb1*, which I showed was critically for regulating the directional migration of epithelial cells in the context of HF regeneration and epidermal repair.

Appendix 1: Ovol1 in adult AD model

Work was done in collaboration with Parama Dey, Ding-Hsiang Huang, and Peng Sun.

Introduction

Atopic dermatitis (AD) is a common skin disease with a complicated epidemiology, affecting large populations of individuals from young children to adults. Compared to more rural areas, AD seems to be far more prevalent in more urban areas. Patients with acute symptoms tend to have lesions which can lead to visible blisters, inflammation, and spongiosis. Chronic AD is characterized by relapsing skin inflammation, disruption of the epidermal barrier function, and sometimes an IgE-mediated sensitization to food and environmental allergens (Bieber 2008). The exact mechanisms for underlying AD etiology overall remains fairly unclear, it is clear that significant barrier defects as there are very few generalizable characteristics across the disease. Clear links have been made in some cases with patients having mutations in filaggrin identifying the FLG gene as a major susceptibility locus. Genome wide associated studies (GWAS) have identified other risk loci for AD as well as *Acne vulgaris*, one of which is OVOL1 (Paternoster et al., 2012; Hirota et al., 2012; Navarini et al., 2014). Ovol1 is a zinc finger transcription factor that is expressed in spinous cells of the epidermis (Nair et al., 2006). In the developing embryo, loss of Ovol1 leads to defective epidermal differentiation characterized by a failure of cells to exit cell cycle (Nair et al., 2006). In this work, our initial experiments aimed at examining the role of Ovol1 in skin inflammatory disease utilizing an AD-like model to test the potential role of Ovol1 as a susceptibility locus in AD (Li et al., 2006). This work made a

number of key observations leading to subsequent studies to dissect the role of *Ovol1* in psoriasis.

Results

To induce AD in mice, I used the chemical MC903 (vitamin D analogue), which induces AD-like symptoms leading to expression of the cytokine TSLP (Li et al., 2006). Application of MC903 on the ears of *Ovol1*-null mice (*Ovol1*^{-/-}) led to thicker ears relative to control mice (Appendix Figure 1.1.A and 1.1.B). At the histological level, I noticed distinct thickening of the epidermis of the *Ovol1*-null mice as well as ridge like structures that protruded into the dermis (Appendix Figure 1.1.C). The basal cells of the *Ovol1*-null mice also appeared to be smaller perhaps reflecting hyperproliferation (Appendix Figure 1.1.C). I noted that in the ears of completely untreated mice, *Ovol1*-null epidermal layer looked indistinguishable compared to the controls (Appendix Figure 1.1.D). Control mice exhibited thickened epidermis after treatment but differentiation markers remained intact as basal cells and spinous cells were marked by K14 and K1 respectively (Appendix Figure 1.1.E). Compared to the control, in the *Ovol1*-null epidermis, I found that the boundaries between EpdSCs and suprabasal layers were less clear and that a lot of these epidermal cells were double positive for both K14 and K1 (Appendix Figure 1.1.E). As one might predict from the histology, there was enhanced proliferation in the *Ovol1*-null mice (Appendix Figure 1.1.F). Together, this data indicates that *Ovol1*-null mice have more robust AD-like symptoms when treated with MC903 characterized by the enhanced proliferation and disrupted differentiation of epidermal cells.

In our AD-like model, MC903 is applied to one ear of the mice, while the other ear is treated with vehicle control, and then simultaneously measured (Appendix Figure 1.1A). Interestingly, I found that these sham/vehicle control ears were also thicker in the *Ovol1*-Null mice compared to controls (Appendix Figure 1.2.A and 1.2.B). In mice that were not treated with MC903 but vehicle control alone, the epidermal thickness between *Ovol1*-null and control mice had no difference indicating that this increase was MC903 dependent (Appendix Figure 1.2.B). The sham ears of *Ovol1*-null mice also displayed enhanced proliferation relative to controls (Appendix Figure 1.2.C). With this increased thickness of the sham ear in the *Ovol1*-null mice, I wondered whether there was increased thickness in other locations of the mice to rule out the simple possibility that the *Ovol1*-null mice were transferring MC903 from the treated ear to the sham ear. Although I couldn't definitively rule this out as a possibility, I found that the *Ovol1*-null mice back skin epidermis was thicker than controls when appropriate ears had been treated with MC903, suggesting possible systemic effects (Appendix Figure 1.2.D). Similar to the differentiation defects observed in treated ears (Appendix Figure 1.1.E), the sham ear of *Ovol1*-null mice also had disrupted differentiation (Appendix Figure 1.2.E). Important to note, *Ovol1*-null mice did still express filaggrin (Appendix Figure 1.2.F).

With the apparent enhanced inflammation in other regions of the mouse (sham treated ear and back skin), I wondered whether there were possible immune related alterations that could explain the systemic effects. I noted that *Ts/p* levels, which are generally elevated in AD were downregulated in the ears of *Ovol1*-null mice (Appendix Figure 1.3.A) (Li et al., 2006). Serum analysis identified upregulation of G-CSF and Cxcl2 in *Ovol1*-null mice (Appendix Figure 1.3.B). ELISA for IgE proved inconclusive and varied

when comparing the serum of control and Ovol1-null mice (Appendix Figure 1.3.C). With alterations in potential immune attracting cytokines, I stained for neutrophils in control and Ovol1-null mice (Appendix Figure 1.3.D). I found a number of neutrophils in the treated ears of control mice, localized in the dermal regions of the ear (Appendix Figure 1.3.D). Interestingly, I found that in the Ovol1-null mice, neutrophils appeared on the surface of the epidermis of the ears, almost as if they had migrated to the epidermal surface (Appendix Figure 1.3.D). In line with the enhanced inflammation of the Ovol1-null sham ear, I noted neutrophils in the dermal regions of these mice although not as severe as MC903 treated (Appendix Figure 1.3.D). I also examined for the presence of mast cells in the ears of control and Ovol1-null mice (Appendix Figure 1.3.E). Although there was no difference in the number of mast cells in the MC903 treated ears between control and Ovol1-null mice (Appendix Figure 1.3.F), there were significantly more in the sham treated ears of the Ovol1-null mice (Appendix Figure 1.3.G).

Discussion

GWAS studies have implicated the role of OVOL1 in skin inflammatory diseases including AD and acne. In this work, I utilized an AD-like model to test the function of Ovol1 in this setting. I found that loss of Ovol1 leads to more severe AD-like phenotypes, indicating that Ovol1 likely plays a protective function. When ears are treated with the AD-inducing agent MC903, Ovol1-null mice display hyperproliferative phenotypes associated with a thicker epidermis and defective differentiation. Interestingly, the observations in the sham treated ears indicate the possibility of systemic effects. Back skin from these mice also displayed signs of thickened epidermis indicating the likelihood of systemic effects.

Examining serum from Ovol1-null mice, I found that levels of G-CSF and Cxcl2 were both upregulated. At the sites of treatment, I noted presence of neutrophils but in the Ovol1-null mice, I found that the neutrophils had migrated to the surface of the epidermis, likely indicating a more severe type of response. Overall this work has led to the further investigation of the role of Ovol1 in skin inflammatory disease.

Additional Materials/Methods

MC903 treatments and thickness measurements

MC903 was dissolved in 70% EtOH and then 4 nmol's were applied to the right ear of those mouse. The left was applied with 70% EtOH as a vehicle control. The ears were treated for 14 consecutive days. Ears were carefully measured using electronic calipers.

Serum analysis prep

At terminal sacrifice, ~1 mL of blood was removed from heart and then placed on ice to allow clot to form for about 15 minutes. Spin the blood down by chilled centrifugation for 10 minutes at 14,000rpm. Save the serum at -80.

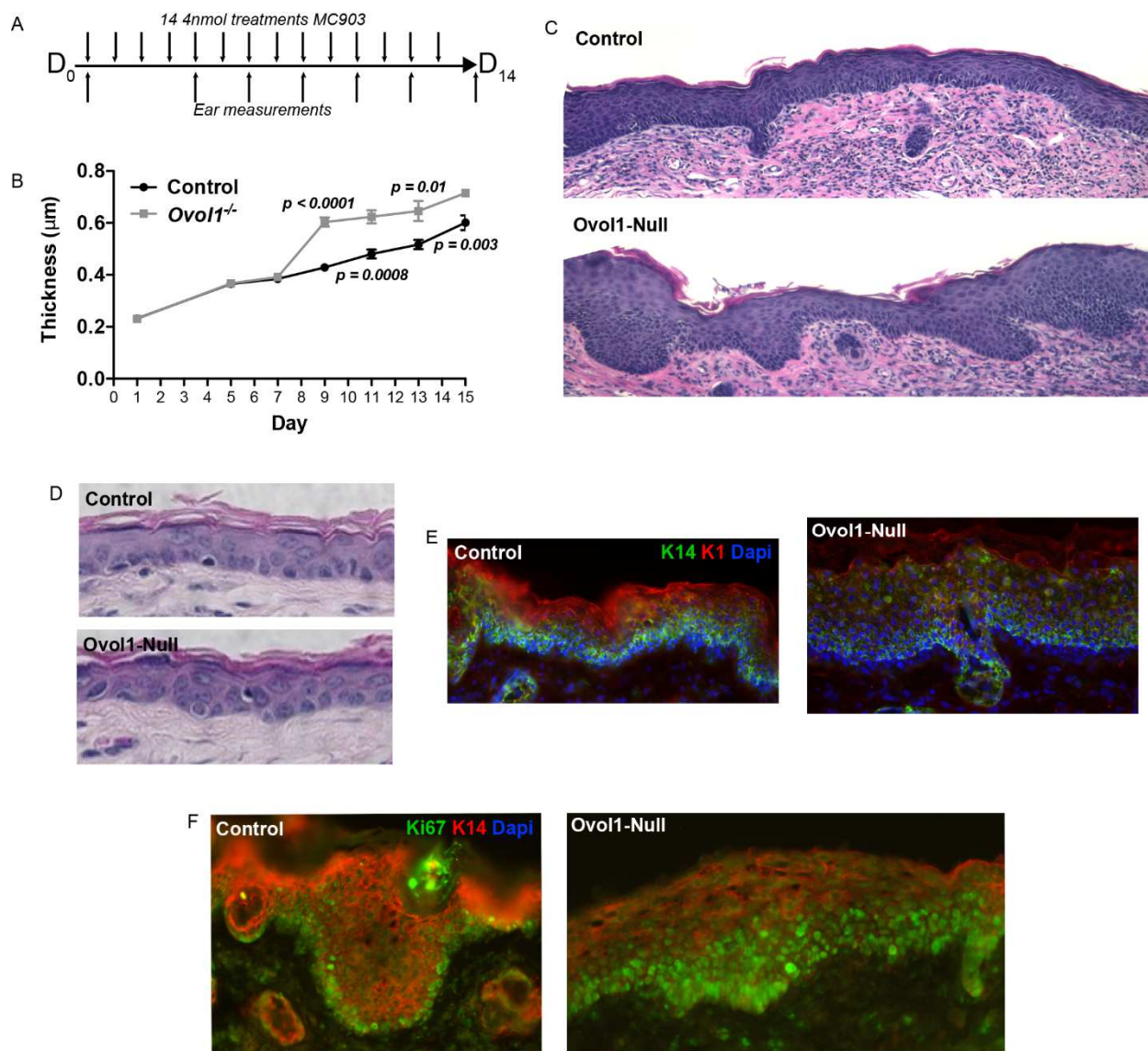
Mast cell staining

Slides were dried in incubator for 10 minutes and then fixed with 4% PFA for 15 minutes. Wash the slides with 1X PBS and then water, each for 5 minutes. Stain with Toluidine Blue Solution for 5 minutes. Rinse with running tap water for 5 minutes. Dry and then mount with permount. To make Toluidine Blue Solution: Mix 4 grams of Urea with

120 mL of water, add 280 mL of isopropanol, and then 2.8 g of toluidine blue O.
Completely dissolve and then filter.

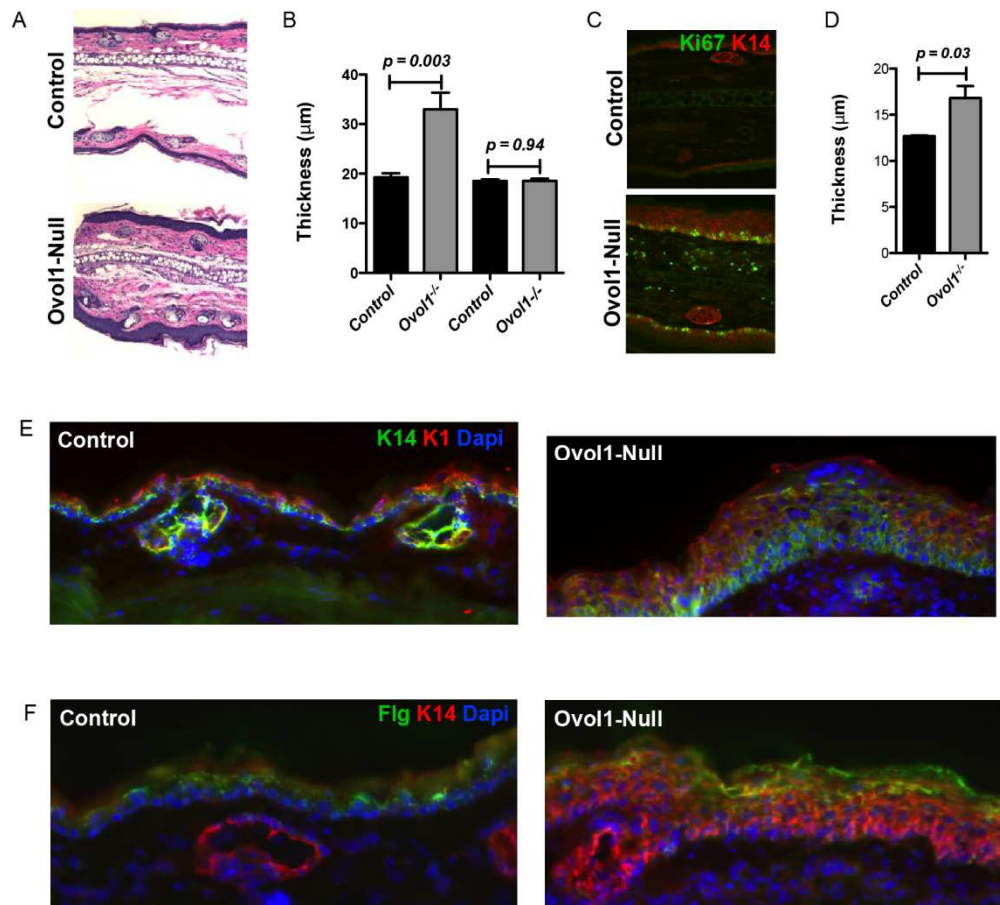
Appendix Figure 1.1. *Ovol1*-null mice have enhanced AD-like symptoms when treated with MC903

- Experimental treatment design over two week period.
- Ear thickness measurements of MC903 treated ears over time course. N = 6 pairs of control and *Ovol1*-null mice.
- H/E of control and *Ovol1*-null ear epidermis after time course treatment with MC903.
- H/E of un-treated control and *Ovol1*-null ear epidermis.
- Indirect immunofluorescence for differentiation markers of control and *Ovol1*-null ear epidermis after time course treatment with MC903.
- Indirect immunofluorescence for proliferative markers of control and *Ovol1*-null ear epidermis after time course treatment with MC903.



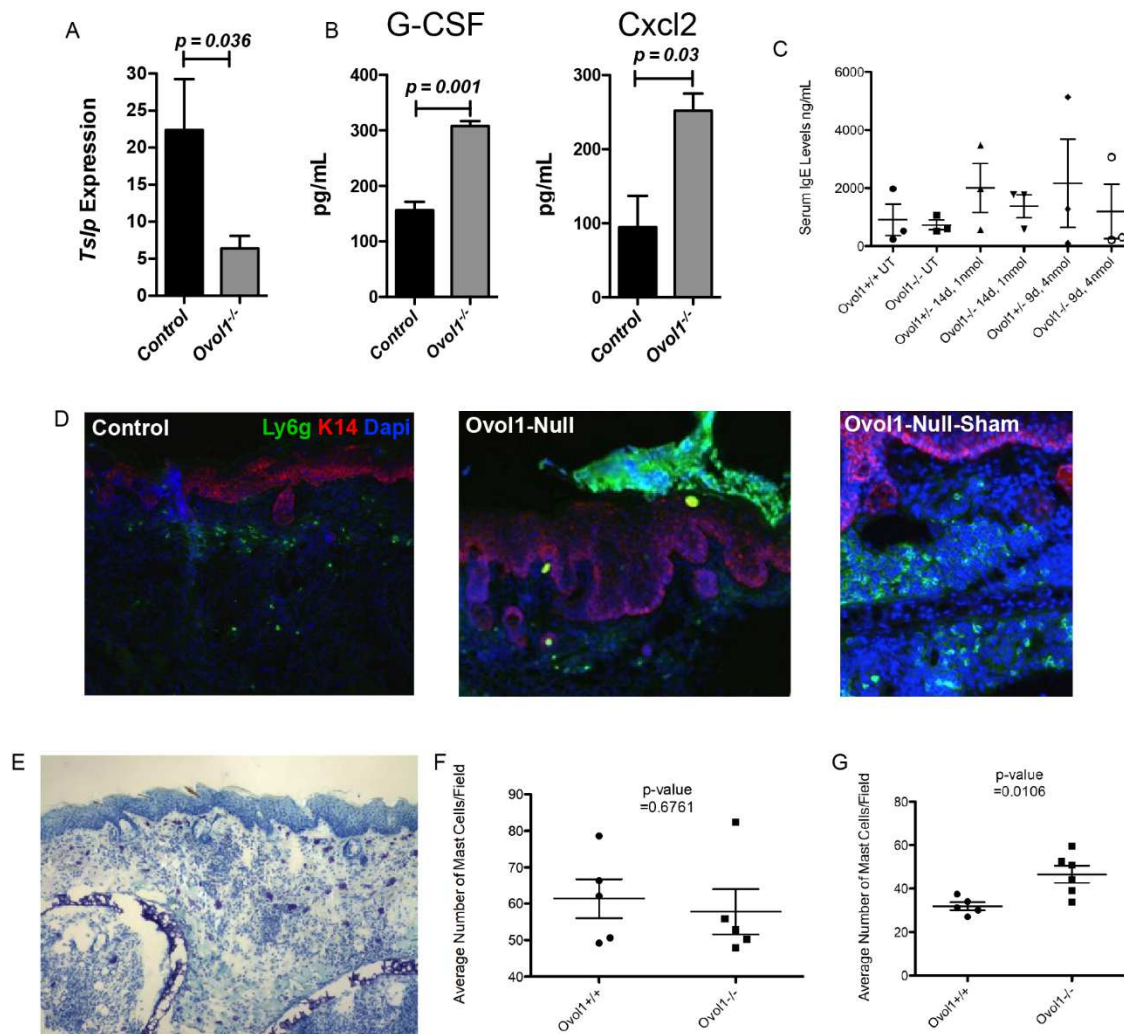
Appendix Figure 1.2. Ovol1-null mice have enhanced AD-like symptoms in sham-treated ears

- H/E of control and Ovol-null ear epidermis from the sham treated ear after time course treatment with MC903.
- Epidermal ear thickness measurements of sham treated (left) or non-treated (right) of control and Ovol1-null mice.
- Indirect immunofluorescence for proliferative markers of control and Ovol1-null ear epidermis from sham treated ear after time course treatment with MC903.
- Epidermal back skin thickness measurements of control and Ovol1-null where mice were subjected to standard MC903 treatment regiment.
- Indirect immunofluorescence for differentiation markers of control and Ovol1-null ear epidermis from sham treated ear after time course treatment with MC903.
- Indirect immunofluorescence for differentiation markers typically mutated in AD of control and Ovol1-null ear epidermis after time course treatment with MC903.



Appendix Figure 1.3. *Ovol1*-null mice have altered endemic and systemic immune responses

- RT-PCR of *Tslp* of control and *Ovol1*-null ear epidermal cells.
- Serum analysis identifying upregulation of circulating cytokines after time course treatment with MC903. Results from Eve Technologies.
- ELISA for IgE in control and *Ovol1*-null mice with indicated treatment regiments.
- Indirect immunofluorescence for Ly6g⁺ neutrophils in control and *Ovol1*-null ears treated with MC903 (left and center respectively). Indirect immunofluorescence for Ly6g⁺ neutrophils in *Ovol1*-null sham treated ears.
- Staining example for mast cells using toluidine blue.
- Quantification of mast cells in MC903 treated ears from control and *Ovol1*-null mice.
- Quantification of mast cells in sham ears from control and *Ovol1*-null mice.



Appendix 2: Inducible deletion of *Ovol2* in HF and epithelial cells

Introduction

Bu-HFSCs are a typically quiescent HF population but can become activated when the HF enters the regenerative anagen phase of the HF cycle (Gonzales and Fuchs 2017). Previous work has shown that when the EMT-inhibiting transcription factor *Ovol2* is lost, there is a delay in HF cycling (Haensel et al., 2018). This model utilized a constitutively active cre-recombinase under the *Krt14* promoter, meaning that recombinase activity initiates at an early embryonic stage. To test direct effects of the loss of *Ovol2* on HF cycling at the adult stage, I decided to utilize two inducible models in order to bypass any potential earlier morphogenic defects incurred with *Ovol2* loss. One cre-recombinase was under inducible activation of the bulge specific *Sox9* and the other was under the inducible activation of the *Krt14* promoter.

Results

For both inducible models, 5 tamoxifen injections were used to induce cre-recombinase expression (Appendix Figure 2.1.A and 2.1.F). To test location of expression using the *Sox9* promoter, I bred with a reporter mouse in order to track cells that have undergone recombination. In the back skin, expression was restricted to the bulge regions of the HF with expression observed in both the inner and outer bulge regions (Appendix Figure 2.1.B left). In the tail epidermis, the expression was seen exclusively in the HF as well but appeared more localized to the inner bulge regions. Flow cytometry of mouse back skin was used to show that approximately 55% of the bulge cells ($CD49f^+CD34^+$) were tdT⁺ (Appendix Figure 2.1.C). To test whether the loss of *Ovol2* in *Sox9* expressing cells disrupts HF cycle, control and *Ovol2^{fl/-};Sox9CreERT;tdT* (iBuKO) mice were waxed

after tamoxifen injections and then analyzed thirteen days later after the mice had entered anagen (Appendix Figure 2.1.A and 2.1.D). Quantification of the number of bulge cells by flow cytometric analysis found no appreciable differences in percentage between control and iBuKO mice.

To further examine the role of *Ovol2* function in regulating HF cycling, an inducible model under the control of *Krt14* promoter (*Ovol2^{fl/-};K14CreERT*; iSSKO) was used to knockout *Ovol2* (Appendix Figure 2.1.F). Although larger proportions of cells (HF and epidermis) would have been targeted, I saw no definitive defects in HF cycling (Appendix Figure 2.1.F and G).

Discussion

Although this study was largely unsuccessful, the tools and methods utilized could be useful in future HF studies in the Dai lab. From a method standpoint, this work provided insight into utilizing the tail epidermis as a potential model. The tail epidermis can be easily used for whole-mount immunofluorescence and genetic labeling. This work also carefully examined the ability to induce anagen via a waxing approach, finding that our methods our timeline of anagen entry is largely in line with published work. This work established a new mouse line in the Dai lab for future use. What this work does suggest is that the ability of *Ovol2* to affect HF cycling is likely due to an accumulation of events beginning during development or dependent on systemic loss over time as adult.

Additional Materials/Methods

Tamoxifen applications and injections

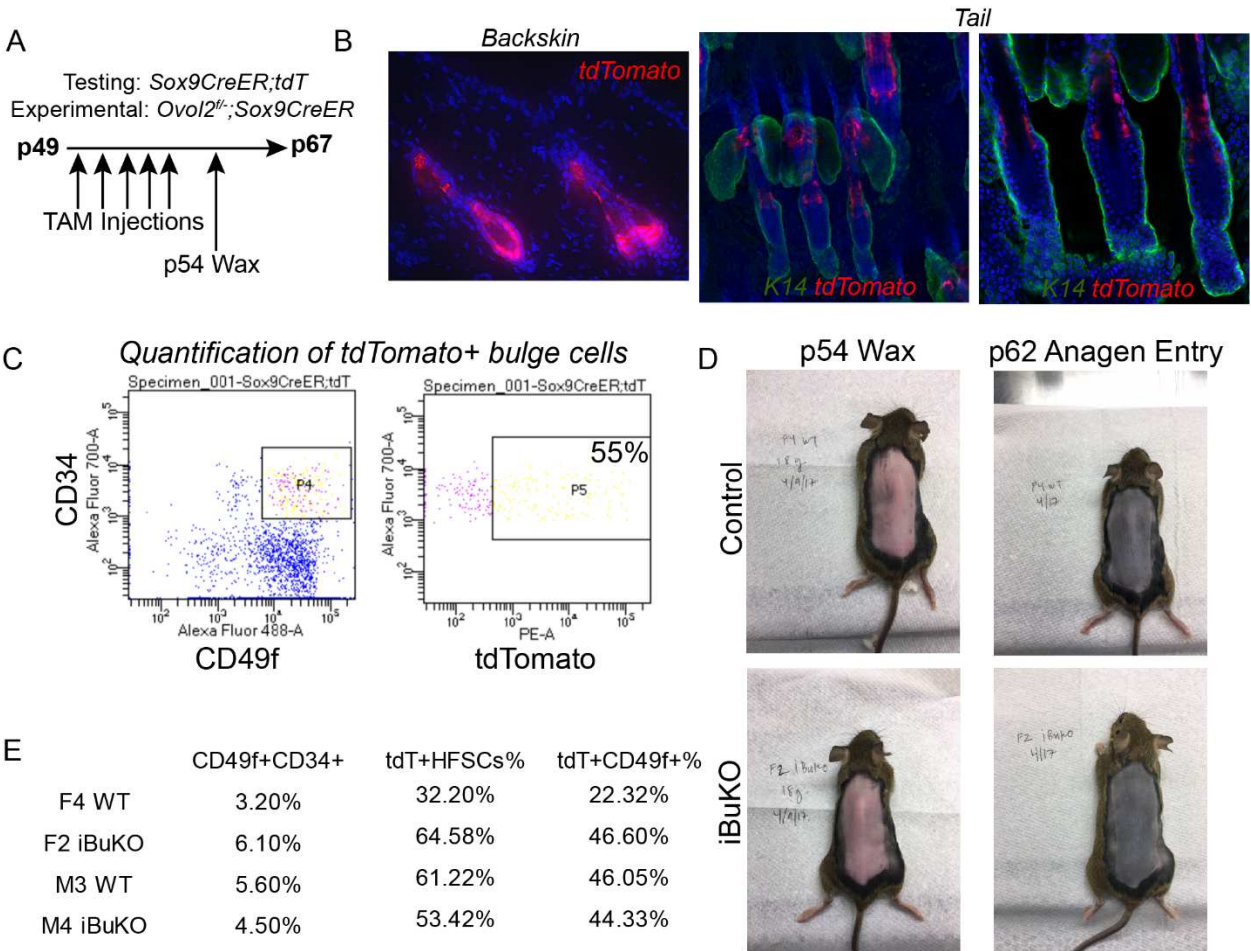
For injections, tamoxifen is dissolved in corn oil at a concentration of 20 mg/mL for at least 4 hours to completely dissolve. Injections are then made at 75 mg of tamoxifen per kg of body weight. For topical applications, I utilize a protocol from the Kobiela lab, which applies 200 μ L of 25 mg/mL to the backs of shaved mice three times between p18-p20.

Wax

To wax mice, mice were initially shaved, waxing pad was applied to the back and then allowed to dry for about 5 minutes before removing.

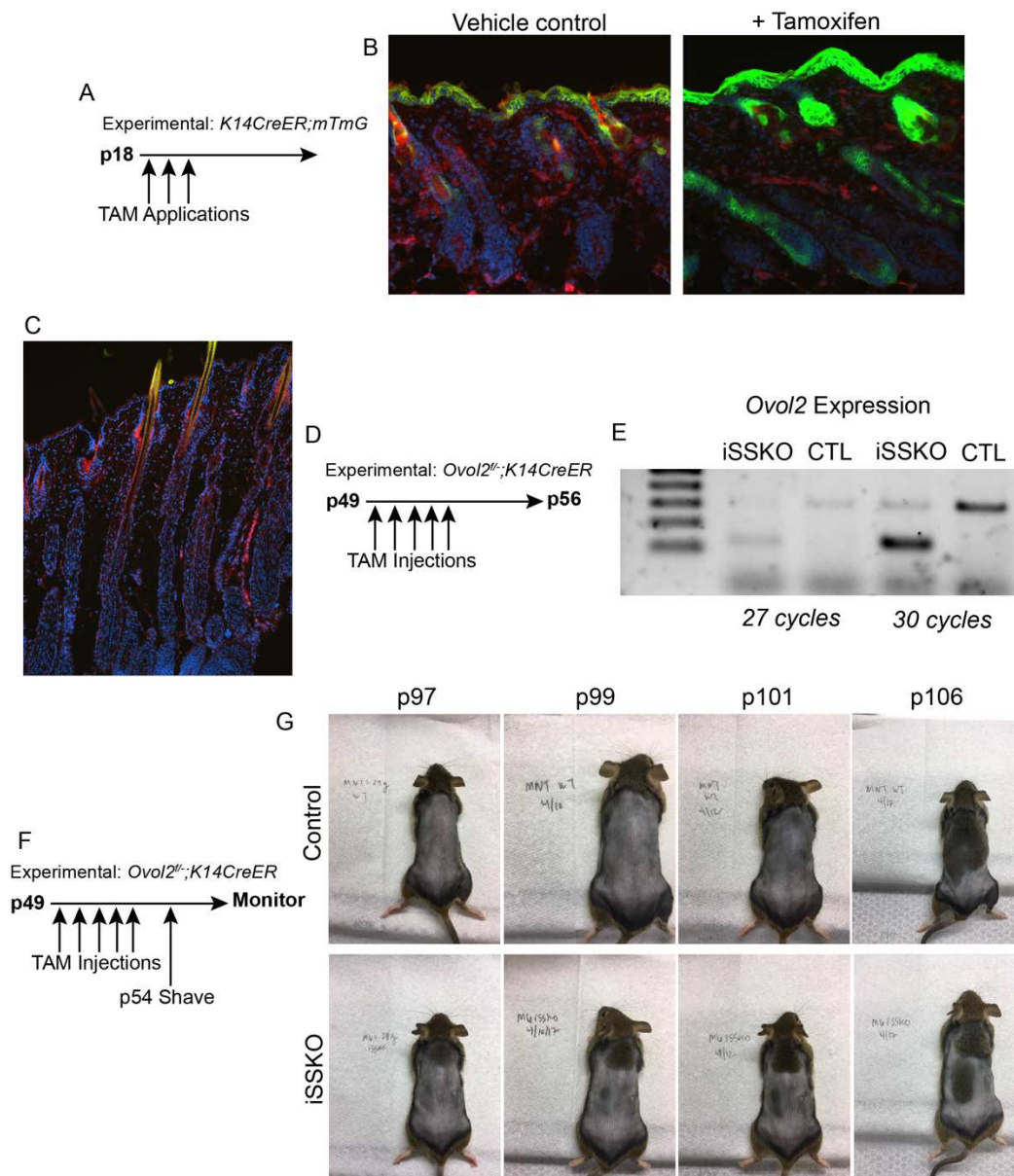
Appendix Figure 2.1. Inducible deletion of *Ovol2* in HF and epithelial cells using *Sox9CreERT*

- A. Schematic diagram of induction and experimental strategy for *Sox9CreERT* based experiments.
- B. Immunofluorescence of back skin and tail epidermis for tdTomato signal.
- C. Flow cytometric analysis of BuHFSCs ($CD49f^+CD34^+$) and the proportion of tdTomato positive cells.
- D. Images of mice after waxing and then a number of days later indicting anagen entry.
- E. Percentages of BuHFSCs 13 days after waxing during active anagen.



Appendix Figure 2.2. Inducible deletion of *Ovol2* in HF and epithelial cells using *K14CreER*

- Schematic diagram of topical induction for some *K14CreER* based experiments.
- Immunofluorescence of back skin at p28 either after 3 topical treatments with tamoxifen or the vehicle control (mice are in same cage).
- Immunofluorescence of back skin at p28 after no treatment indicating.
- Schematic diagram of induction (via IP injections) and experimental strategy for *K14CreER* testing of recombination.
- Ovol2* expression analysis of control and iSSKO mice after tamoxifen injections.
- Schematic diagram of induction and experimental strategy for *K14CreER* based experiments.
- Monitoring anagen entry after shaving.



Appendix 3: Immune response characterization in *Ovo/2* SSKO wounds

Introduction

Epidermal wound healing is a multi-step process involving the recruitment of various immune cells to both assist in the clearance of pathogens and promote the regenerative processes of the epidermis (Gurtner et al., 2008). Directly after a major wound trauma, initial inflammation and coagulation begin, preventing blood loss and initial recruitment of immune cells to clear any pathogens (Gurtner et al., 2008). I have previously identified that there is an upregulation of immune related genes after the loss of *Ovo/2* in cultured new born primary keratinocytes (Haensel et al., 2018). I aimed to validate this up-regulation of immune related genes in an *in vivo* wound model and whether I could detect any modulation in immune response.

RESULTS

In previous published studies, I found that there was an up-regulation of certain immune related gene signatures and specific immune genes (Haensel et al., 2018). Of note, Gene Set Enrichment Analysis (GSEA) found enrichment for both interferon- α and interferon- γ responses in the *Ovo/2*-deficient cells (Appendix Figure 3.1.A). Subsequent confirmation by qRT-PCR showed *Ccl2* and *Ccl7* upregulation in *Ovo/2*-deficient keratinocytes, indicating that loss of *Ovo/2* might alter immune type responses (Appendix Figure 3.1.B). To elicit an immune response *in vivo*, I wounded *Ovo/2* SSKO and control mice (Appendix Figure 3.1.C). I sorted epidermal cells from the migrating front of the wounds utilizing a novel cell surface marker, CD51, which is highly up-regulated in this

region (Aragona et al., 2017). qRT-PCR analysis of these CD51⁺CD49f⁺ cells found a general upregulation of *Ccl2* and *Ccl7* in vivo (Appendix Figure 3.1.D and 3.1.E). As *Ccl2* and *Ccl7* are known macrophage chemoattractants, I aimed to quantify the number of F4/80⁺ immune cells present in the wounds. In general, I reinforced an anecdotal observation (from H/E of *Ovo2* SSKO wounds) of increased cellularity within the wounds of *Ovo2*-deficient mice (Appendix Figure 3.1.F). I also noted that there were both more CD45⁺ immune cells and more CD49f⁺ epithelial cells in the wounds of *Ovo2* SSKO mice (Appendix Figure 3.1.F). Finally, I found that although there is some variability between mouse pairs, the *Ovo2* SSKO mice always had more immune cells compared to their same sex littermate control (Appendix Figure 3.1.G-I).

Discussion

The immune response after wounding is critical to facilitate pathogen clearance as well as facilitate effective wound regeneration (Gurtner et al., 2008). This work highlights a potential role of *Ovo2* in modulation of pro-inflammatory molecules from epidermal keratinocytes as its loss leads to up-regulation of pro-inflammatory cytokines that recruit macrophages. It is tempting to speculate that this is through a direct *Ovo2*-regulated mechanism but further studies would be needed. Also this work established the use of a new surface marker in the Dai lab, I was able to sort cells directly from the migrating front of the wound and use low numbers of cells (under 1000) for qRT-PCR.

Additional Materials/Methods

Single cell suspensions of wounds

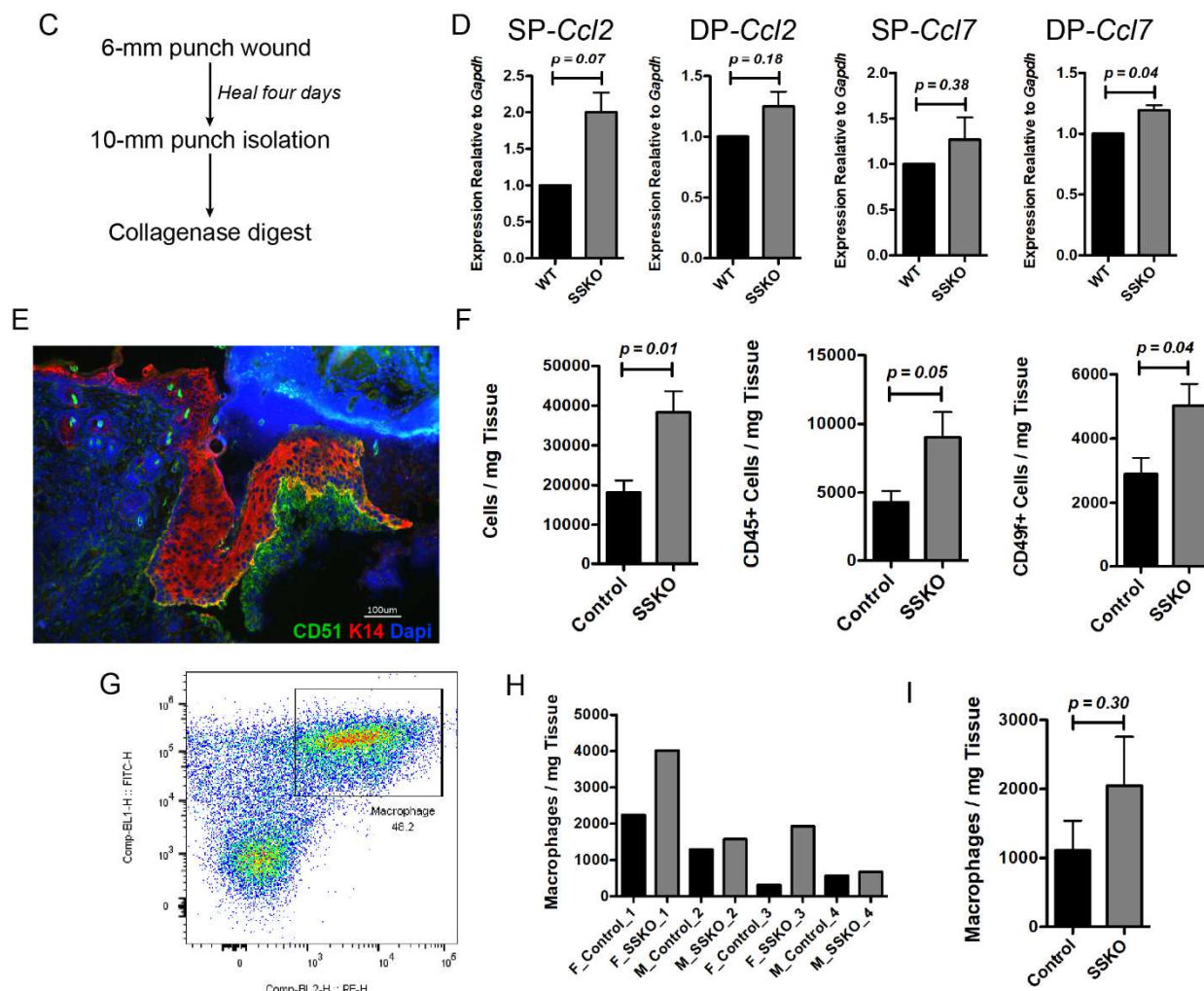
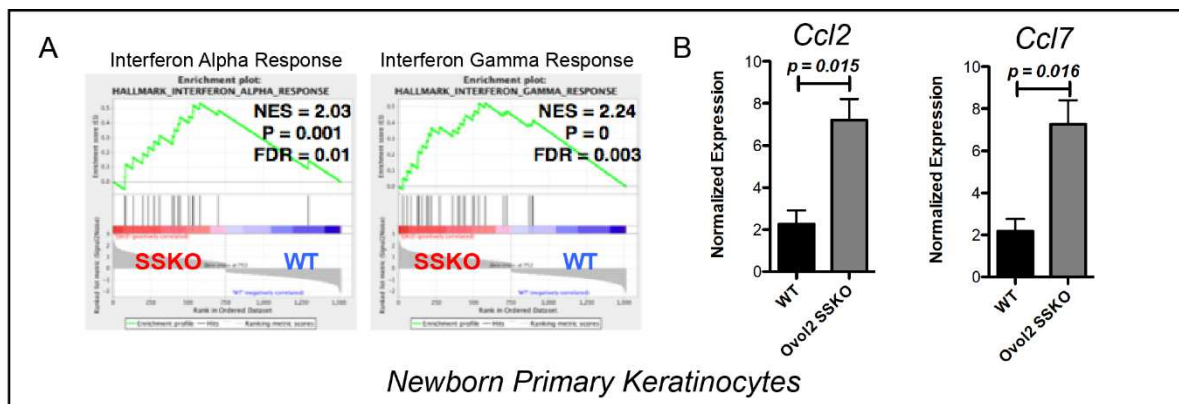
To isolate cells from wounded back skin, skin was removed, large pieces of fat attached to underside of wound were carefully removed, a 10-mm punch (Acuderm; 0413) was then used to punch out both off the wounds (capturing the wound and a portion of un-wounded skin adjacent to the wound). The wounds were then minced into pieces less than 1 mm in diameter. The minced samples were placed in 15-mL conical tubes and digested with 10 mL of collagenase mix (0.25% collagenase (Sigma; C9091), 0.01M HEPES (Fisher; BP310), 0.001M Sodium Pyruvate (Fisher; BP356), and 0.1 mg/mL DNase (Sigma; DN25)). Samples are incubated at 37 °C for 2 hours with rotation. Samples are then filtered with 70-µm and 40-µm filters, spun down, and resuspended in 2% FBS.

Low cell number expression analysis

After single cell isolation from wounds, cells were stained for CD49f and CD51. Using the plate function on FACS Aria, 1000 cells, were sorted into 96-well plates that were either CD49f⁺CD51⁺ or CD49f⁺CD51⁻. Cells were sorted into lysis buffer from the Cells-to-CT Kit (Invitrogen; A35379) and then manufacture instructions were subsequently followed.

Appendix Figure 3.1. Immune response characterization in *Ovo/2* SSKO wounds

- A. GSEA of NBPKs from control and *Ovo/2* SSKO mice. N = 2 pairs.
- B. qRT-PCR analysis of NBPKs from control and *Ovo/2* SSKO mice. N = 4 pairs.
- C. Schematic diagram of wounding and wound isolation.
- D. qRT-PCR analysis of sorted SP (single positive, CD49f⁺) or DP (double positive, CD49f⁺CD51⁺) cells isolated from control and *Ovo/2* SSKO wounds. N = 3 pairs.
- E. Indirect immunofluorescence of wound during active re-epithelialization.
- F. Total numbers of cells, immune cells (CD45⁺), and epidermal cells (CD49f⁺) from control and *Ovo/2* SSKO wounds. N = 4 pairs.
- G. Representative flow cytometric plot for macrophage staining.
- H. Individual analysis of total numbers of macrophages in each sample. N = 4 pairs.
- I. Averaged numbers of macrophages in control and *Ovo/2* SSKO mice. N = 4 pairs.



Appendix 4 *Ovol1*/*Ovol2* double knockout generation and initial phenotypic analysis

Introduction

Previous studies have knocked out both *Ovol1* and *Ovol2* in the developing epidermis and found severe morphogenic phenotypes including during HF morphogenesis and epidermal differentiation (Lee et al., 2014). Previous work has also identified the role of *Ovol2* in regulating HF cycling in the adult mouse (Haensel et al., 2018). In this work I aimed to test the function of both *Ovol1* and *Ovol2* in the adult mouse, generating a completely inducible mouse model to simultaneously target both genes at a desired timepoint. As loss of both *Ovol1* and *Ovol2* may lead to lethality in adult mice, utilization of an inducible model with cre-recombinase under the control of the *Krt14* promoter would bypass embryonic perpetuated phenotypes.

Results

Initial characterization of DKO mice (*Ovol1*^{f/-};*Ovo2*^{f/-};*K14CreER*) focused on identifying potential defects in HF cycling (Appendix Figure 4.1.A). For initial studies I shaved the mice after completion of tamoxifen injections and watched for anagen entry but found no major defects (Appendix Figure 4.1.B). I next checked whether I could elicit defects in HF entry after plucking hairs from the backs of mice after tamoxifen injections but again found no major defects (Appendix Figure 4.1.C). I also checked whether there were apparent differences in timing of tamoxifen injections (p19-23 vs p49-53). I reasoned that at an earlier injection schedule would add an additional round of cycling (Appendix 4.1.D and 4.1.E). Interestingly, it appeared that when DKO mice were injected at the

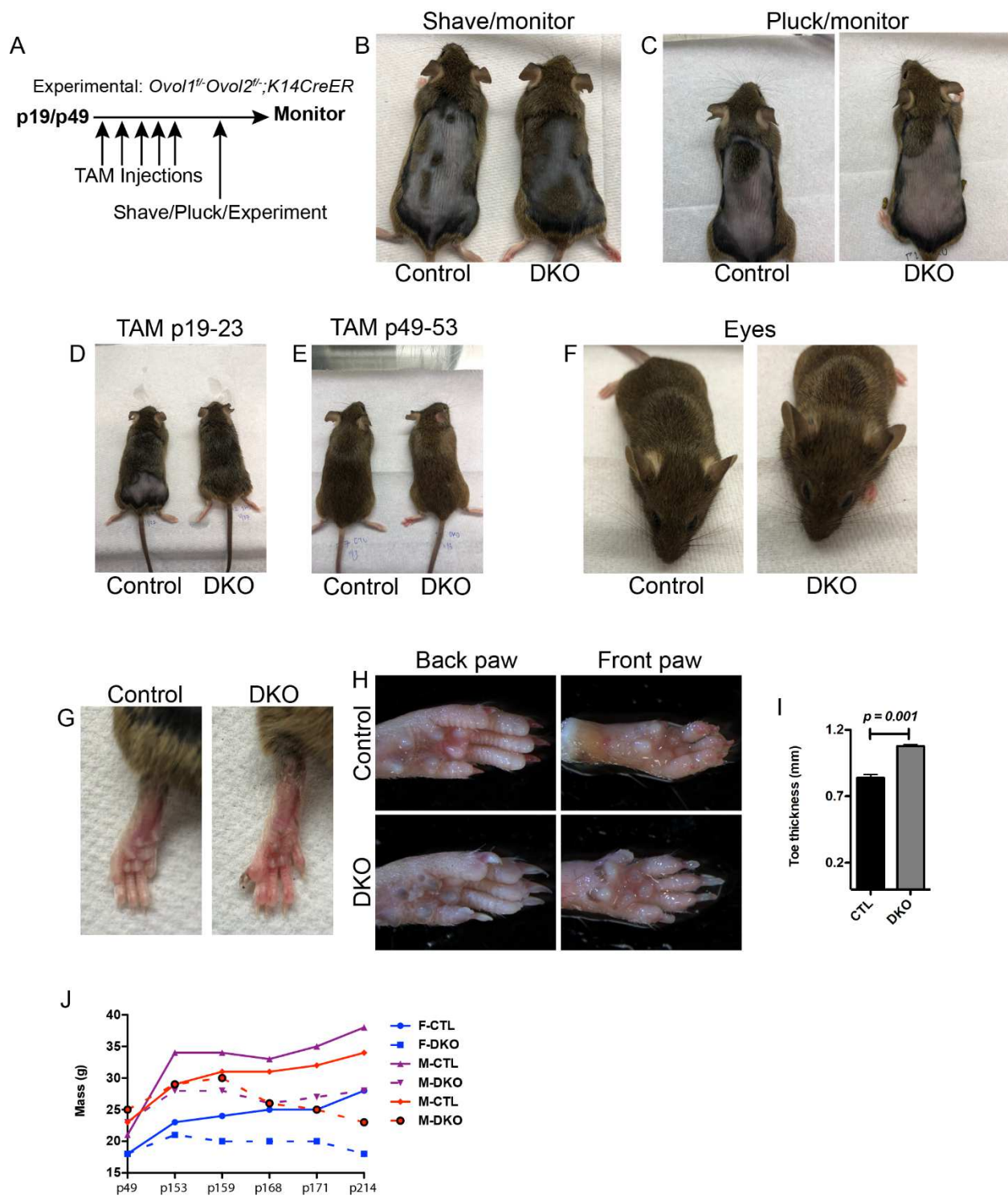
earlier timepoint, they appeared to be characterized by more 'aged' type hair with more matted hair and (Appendix 4.1.D). Additional 'aged' phenotypes were seen around the eyes of DKO mice, with slight discolorations of the hair around the eyes (Appendix Figure 4.1.F). The most striking phenotypes were observed in the nails of the DKO mice, which appeared to be inflamed with longer nails (Appendix Figure 4.1.G-I). The footpads of the DKO mice also appeared to have dark discoloration (Appendix Figure 4.1.H). I also noted that there were severe defects with respect to weight gain (Appendix Figure 4.1.J).

Conclusions

In this work, I generated a new inducible mouse model leading to the simultaneous knockout of both *Ovo1* and *Ovo2*. Our preliminary findings identify that loss of *Ovo1* and *Ovo2* lead to severe phenotypes with age. The toes of DKO mice appear enlarged and have longer nails suggesting that there might be alterations in the toe stem cell populations. The severe weight difference (although initially fine) suggest that mice are not able to maintain weight but what defects this might be mechanistically attributed remains to be investigated.

Appendix Figure 4.1. Ovol1/Ovol2 double knockout generation and initial phenotypic analysis

- A. Schematic diagram of injection strategy.
- B. Pictures of control and DKO mice that have been injected with tamoxifen from p49-p53, shaved, and then imaged at p96.
- C. Pictures of control and DKO mice that have been injected with tamoxifen from p19-p23, hairs plucked at p56, and then imaged at p72.
- D. Pictures of control and DKO mice that have been injected with tamoxifen from p19-p23, shaved at p54, and then imaged at p121.
- E. Pictures of control and DKO mice that have been injected with tamoxifen from p49-p53, shaved at p54, and then imaged at p145.
- F. Pictures of control and DKO mice focusing on eye regions. Mice have been aged, injected with tamoxifen from p49-p53, shaved at p54, and then imaged at p145.
- G. Zoomed in images of control and DKO mice focusing on the feet of mice. Mice have been aged, injected with tamoxifen from p49-p53, shaved at p54, and then imaged at p145.
- H. Further analysis of feet using dissecting microscope of mice from (G).
- I. Thickness measurements of toes from control and DKO mice.
- J. Analysis of body weights of paired control and DKO mice that have been injected with tamoxifen between p49-p53.



References

- Adam, R. C. *et al.* (2015) 'Pioneer factors govern super-enhancer dynamics in stem cell plasticity and lineage choice', *Nature*, 521(7552), pp. 366–370. doi: 10.1038/nature14289.
- Andl, T. (2004) 'Epithelial Bmpr1a regulates differentiation and proliferation in postnatal hair follicles and is essential for tooth development', *Development*. doi: 10.1242/dev.01125.
- Andrianne, M. *et al.* (2017) 'Tristetraprolin expression by keratinocytes controls local and systemic inflammation', *JCI Insight*, 2(11). doi: 10.1172/jci.insight.92979.
- Aragona, M. *et al.* (2017) 'Defining stem cell dynamics and migration during wound healing in mouse skin epidermis', *Nature Communications*, 8. doi: 10.1038/ncomms14684.
- Arnoux, V. *et al.* (2005) 'Cutaneous wound reepithelialization: a partial and reversible EMT', in *Rise and fall of epithelial phenotype*.
- Arnoux, V. *et al.* (2008) 'Erk5 controls slug expression and keratinocyte activation during wound healing', *Mol Biol Cell*, 19(11), pp. 4738–4749. doi: 10.1091/mbc.E07-10.
- Arwert, E. N., Hoste, E. and Watt, F. M. (2012) 'Epithelial stem cells, wound healing and cancer', *Nat Rev Cancer*, 12(3), pp. 170–180. doi: 10.1038/nrc3217.
- Beaudry, V. G. *et al.* (2010) 'Loss of the desmosomal component perp impairs wound healing in vivo', *Dermatol Res Pract*, 2010, p. 759731. doi: 10.1155/2010/759731.
- Bieber, T. (2008) 'Atopic dermatitis', *New England Journal of Medicine*, 258, pp. 1483–1494. doi: 10.5021/ad.2010.22.2.125.
- Bielefeld, K. A., Amini-Nik, S. and Alman, B. A. (2013) 'Cutaneous wound healing:

recruiting developmental pathways for regeneration', *Cell Mol Life Sci*, 70(12), pp. 2059–2081. doi: 10.1007/s00018-012-1152-9.

Blanpain, C. *et al.* (2004) 'Self-renewal, multipotency, and the existence of two cell populations within an epithelial stem cell niche', *Cell*, 118(5), pp. 635–648. doi: 10.1016/j.cell.2004.08.012.

Blanpain, C. and Fuchs, E. (2014) 'Plasticity of epithelial stem cells in tissue regeneration', *Science*, 344(6189). doi: 10.1126/science.1242281.

Blanpain, C., Horsley, V. and Fuchs, E. (2007) 'Epithelial Stem Cells: Turning over New Leaves', *Cell*. doi: 10.1016/j.cell.2007.01.014.

Brabletz, S. *et al.* (2017) 'Generation and characterization of mice for conditional inactivation of Zeb1', *Genesis*, 55(4). doi: 10.1002/dvg.23024.

Brabletz, S. and Brabletz, T. (2010) 'The ZEB/miR-200 feedback loop--a motor of cellular plasticity in development and cancer?', *EMBO Rep*, 11(9), pp. 670–677. doi: 10.1038/embor.2010.117.

Brem, H. and Tomic-Canic, M. (2007) 'Cellular and molecular basis of wound healing in diabetes', *J Clin Invest*, 117(5), pp. 1219–1222. doi: 10.1172/JCI32169.

van den Brink, S. C. *et al.* (2017) 'Single-cell sequencing reveals dissociation-induced gene expression in tissue subpopulations', *Nature Methods*, 14(10), pp. 935–936. doi: 10.1038/nmeth.4437.

Briso, E. M. *et al.* (2013) 'Inflammation-mediated skin tumorigenesis induced by epidermal c-Fos', *Genes and Development*, 27(18), pp. 1959–1973. doi: 10.1101/gad.223339.113.

Butler, A. *et al.* (2018) 'Integrating single-cell transcriptomic data across different

conditions, technologies, and species', *Nat Biotechnol*, 36(5), pp. 411–420. doi: 10.1038/nbt.4096.

Chaffer, C. L. *et al.* (2016) 'EMT, cell plasticity and metastasis', *Cancer and Metastasis Reviews*. doi: 10.1007/s10555-016-9648-7.

Chakrabarti, R. *et al.* (2012) 'Elf5 inhibits the epithelial-mesenchymal transition in mammary gland development and breast cancer metastasis by transcriptionally repressing Snail2', *Nat Cell Biol*, 14(11), pp. 1212–1222. doi: 10.1038/ncb2607.

Cheng, F. *et al.* (2016) 'Vimentin coordinates fibroblast proliferation and keratinocyte differentiation in wound healing via TGF-beta-Slug signaling', *Proc Natl Acad Sci U S A*, 113(30), pp. E4320-7. doi: 10.1073/pnas.1519197113.

Cheung, T. H. and Rando, T. A. (2013) 'Molecular regulation of stem cell quiescence.', *Nature reviews. Molecular cell biology*, 14(6), pp. 329–340. doi: 10.1038/nrm3591.

Chigurupati, S. *et al.* (2007) 'Involvement of notch signaling in wound healing', *PLoS One*, 2(11), p. e1167. doi: 10.1371/journal.pone.0001167.

Cinco, R. *et al.* (2016) 'Spatial Characterization of Bioenergetics and Metabolism of Primordial to Preovulatory Follicles in Whole Ex Vivo Murine Ovary', *Biology of Reproduction*, 95(6), p. 129. doi: 10.1095/biolreprod.116.142141.

Colyer, R. A., Lee, C. and Gratton, E. (2008) 'A novel fluorescence lifetime imaging system that optimizes photon efficiency', *Microscopy Research and Technique*, 71(3), pp. 201–213. doi: 10.1002/jemt.20540.

Cotsarelis, G., Sun, T. T. and Lavker, R. M. (1990) 'Label-retaining cells reside in the bulge area of pilosebaceous unit: Implications for follicular stem cells, hair cycle, and skin carcinogenesis', *Cell*. doi: 10.1016/0092-8674(90)90696-C.

- Coulombe, P. (1997) 'Towards a molecular definition of keratinocyte activation after acute injury to stratified epithelia', *Biochemical and Biophysical Research Communications*, 236, pp. 231–238.
- Coulombe, P. A. (2003) 'Wound epithelialization: accelerating the pace of discovery', *J Invest Dermatol*, 121(2), pp. 219–230. doi: 10.1046/j.1523-1747.2003.12387.x.
- Dekoninck, S. and Blanpain, C. (2019) 'Stem cell dynamics, migration and plasticity during wound healing', *Nature Cell Biology*, 21, pp. 12–24. doi: 10.1038/s41556-018-0237-6.
- Digman, M. A. *et al.* (2008) 'The phasor approach to fluorescence lifetime imaging analysis', *Biophysical Journal*, 94(2). doi: 10.1529/biophysj.107.120154.
- Eming, S. A., Martin, P. and Tomic-Canic, M. (2014) 'Wound repair and regeneration: mechanisms, signaling, and translation', *Sci Transl Med*, 6(265), pp. 1–16. doi: 10.1126/scitranslmed.3009337.
- Ferguson, M. W. and O'Kane, S. (2004) 'Scar-free healing: from embryonic mechanisms to adult therapeutic intervention', *Philos Trans R Soc Lond B Biol Sci*, 359(1445), pp. 839–850. doi: 10.1098/rstb.2004.1475.
- Florin, L. *et al.* (2006) 'Delayed wound healing and epidermal hyperproliferation in mice lacking JunB in the skin', *Journal of Investigative Dermatology*, 126(4), pp. 902–911. doi: 10.1038/sj.jid.5700123.
- Friedl, P. and Gilmour, D. (2009) 'Collective cell migration in morphogenesis, regeneration and cancer', *Nat Rev Mol Cell Biol*, 10(7), pp. 445–457. doi: 10.1038/nrm2720.
- Garrod, D. R. *et al.* (2005) 'Hyper-adhesion in desmosomes: its regulation in wound

healing and possible relationship to cadherin crystal structure', *J Cell Sci*, 118(Pt 24), pp. 5743–5754. doi: 10.1242/jcs.02700.

Gawronska-Kozak, B. *et al.* (2016) 'Foxn1 Transcription Factor Regulates Wound Healing of Skin through Promoting Epithelial-Mesenchymal Transition', *PLoS One*, 11(3), p. e0150635. doi: 10.1371/journal.pone.0150635.

Ge, Y. *et al.* (2017) 'Stem Cell Lineage Infidelity Drives Wound Repair and Cancer', *Cell*, 169(4), p. 636–650 e14. doi: 10.1016/j.cell.2017.03.042.

Gonzales, K. A. U. and Fuchs, E. (2017) 'Skin and Its Regenerative Powers: An Alliance between Stem Cells and Their Niche', *Dev Cell*, 43(4), pp. 387–401. doi: 10.1016/j.devcel.2017.10.001.

Greco, V. *et al.* (2009) 'A two-step mechanism for stem cell activation during hair regeneration', *Cell Stem Cell*, 4(2), pp. 155–169. doi: 10.1016/j.stem.2008.12.009.

Grinnell, F. (1992) 'Wound repair, keratinocyte activation and integrin modulation', *J Cell Sci*, 101, pp. 1–5.

Guo, W. *et al.* (2012) 'Slug and Sox9 cooperatively determine the mammary stem cell state', *Cell*, 148(5), pp. 1015–1028. doi: 10.1016/j.cell.2012.02.008.

Gurtner, G. C. *et al.* (2008) 'Wound repair and regeneration', *Nature*, 453. doi: 10.1038/nature07039.

Haensel, D. *et al.* (2018a) 'An Ovol2-Zeb1 transcriptional circuit regulates epithelial directional migration and proliferation', *EMBO reports*, p. e46273. doi: 10.15252/embr.201846273.

Haensel, D. *et al.* (2018b) 'An Ovol2-Zeb1 transcriptional circuit regulates epithelial directional migration and proliferation', *EMBO Reports*. doi:

10.15252/embr.201846273.

Haensel, D. and Dai, X. (2018) 'Epithelial-to-mesenchymal transition in cutaneous wound healing: Where we are and where we are heading', *Dev Dyn*, 247(3), pp. 473–480. doi: 10.1002/dvdy.24561.

Haensel, D., McNeil, M. A. and Dai, X. (2018) 'Ex Vivo Imaging and Genetic Manipulation of Mouse Hair Follicle Bulge Stem Cells', *Methods Mol Biol*. doi: 10.1007/7651_2018_136.

Hammond, N. L., Headon, D. J. and Dixon, M. J. (2012) 'The cell cycle regulator protein 14-3-3 is essential for hair follicle integrity and epidermal homeostasis', *Journal of Investigative Dermatology*, 132(6), pp. 1543–53. doi: 10.1038/jid.2012.27.

Han, X. *et al.* (2018) 'Mapping the Mouse Cell Atlas by Microwell-Seq', *Cell*, 172(5), pp. 1091–1107. doi: 10.1016/j.cell.2018.02.001.

Herschman, H. (1991) 'Primary Response Genes Induced By Growth Factors And Tumor Promoters', *Annual Review of Biochemistry*, 60, pp. 281–319. doi: 10.1146/annurev.biochem.60.1.281.

Hirota, T. *et al.* (2012) 'Genome-wide association study identifies eight new susceptibility loci for atopic dermatitis in the Japanese population', *Nat Genet*, 44(11), pp. 1222–1226. doi: 10.1038/ng.2438.

Hong, W. X. *et al.* (2014) 'The Role of Hypoxia-Inducible Factor in Wound Healing', *Advances in Wound Care*, 3(5), pp. 390–399. doi: 10.1089/wound.2013.0520.

Hopfensitz, M. *et al.* (2012) 'Multiscale binarization of gene expression data for reconstructing Boolean networks', *IEEE/ACM Transactions on Computational Biology and Bioinformatics*, 9(2), pp. 487–98. doi: 10.1109/TCBB.2011.62.

- Hsu, Y. C. (2015) 'Theory and practice of lineage tracing', *Stem Cells*. doi: 10.1002/stem.2123.
- Hsu, Y. C., Li, L. and Fuchs, E. (2014) 'Emerging interactions between skin stem cells and their niches', *Nat Med*, 20(8), pp. 847–856. doi: 10.1038/nm.3643.
- Hudson, L. G. *et al.* (2009) 'Cutaneous wound reepithelialization is compromised in mice lacking functional Slug (Snai2)', *J Dermatol Sci*, 56(1), pp. 19–26. doi: 10.1016/j.jdermsci.2009.06.009.
- Ingraham, C. R. *et al.* (2006) 'Abnormal skin, limb and craniofacial morphogenesis in mice deficient for interferon regulatory factor 6 (Irf6)', *Nature Genetics*, 38(11), pp. 1335–40. doi: 10.1038/ng1903.
- Inman, J. L. *et al.* (2015) 'Mammary gland development: cell fate specification, stem cells and the microenvironment', *Development*. doi: 10.1242/dev.087643.
- Irvine, A. D., McLean, W. H. I. and Leung, D. Y. M. (2011) 'Filaggrin mutations associated with skin and allergic diseases.', *The New England journal of medicine*, 365, pp. 1315–1327. doi: 10.1056/NEJMra1011040.
- Ito, M. *et al.* (2004) 'Hair follicle stem cells in the lower bulge form the secondary germ, a biochemically distinct but functionally equivalent progenitor cell population, at the termination of catagen', *Differentiation*, 72(9).
- Ito, M. *et al.* (2007) 'Wnt-dependent de novo hair follicle regeneration in adult mouse skin after wounding', *Nature*, 447(7142), pp. 316–320. doi: 10.1038/nature05766.
- Jiang, R. *et al.* (1998) 'The slug gene is not essential for mesoderm or neural crest development in mice', *Dev Biol*, 198(2), pp. 227–285.
- Jiang, X. pin *et al.* (2013) 'Downregulation of CD9 in Keratinocyte Contributes to Cell

Migration via Upregulation of Matrix Metalloproteinase-9', *PLoS ONE*, 8(10). doi: 10.1371/journal.pone.0077806.

Jin, S. *et al.* (2018) 'ScEpath: Energy landscape-based inference of transition probabilities and cellular trajectories from single-cell transcriptomic data', *Bioinformatics*, 34(12), pp. 2077–2086. doi: 10.1093/bioinformatics/bty058.

Jolly, M. K. *et al.* (2017) 'EMT and MET: necessary or permissive for metastasis?', *Molecular Oncology*. doi: 10.1002/1878-0261.12083.

Joost, S. *et al.* (2016) 'Single-Cell Transcriptomics Reveals that Differentiation and Spatial Signatures Shape Epidermal and Hair Follicle Heterogeneity', *Cell Systems*, 3(3), pp. 221–237. doi: 10.1016/j.cels.2016.08.010.

Joost, S. *et al.* (2018) 'Single-Cell Transcriptomics of Traced Epidermal and Hair Follicle Stem Cells Reveals Rapid Adaptations during Wound Healing', *Cell Reports*, 25(3), pp. 585–597. doi: 10.1016/j.celrep.2018.09.059.

Kalluri, R. and Weinberg, R. A. (2009) 'The basics of epithelial-mesenchymal transition', *J Clin Invest*, 119(6), pp. 1420–1428. doi: 10.1172/JCI39104.

Keyes, B. E. *et al.* (2016) 'Impaired Epidermal to Dendritic T Cell Signaling Slows Wound Repair in Aged Skin', *Cell*, 167(5), p. 1323–1338 e14. doi: 10.1016/j.cell.2016.10.052.

Kim, D. *et al.* (2013) 'TopHat2: accurate alignment of transcriptomes in the presence of insertions, deletions and gene fusions', *Genome Bio*, 14(R36).

Kim, S. M. *et al.* (2016) 'Targeting cancer metabolism by simultaneously disrupting parallel nutrient access pathways', *Journal of Clinical Investigation*, 126(11), pp. 4088–4102. doi: 10.1172/JCI87148.

- Kuwahara, M. *et al.* (2001) 'E-cadherin expression in wound healing of mouse skin', *J Cutan Pathol*, 28, pp. 191–199.
- Lamouille, S., Xu, J. and Derynck, R. (2014) 'Molecular mechanisms of epithelial-mesenchymal transition', *Nat Rev Mol Cell Biol*, 15(3), pp. 178–196. doi: 10.1038/nrm3758.
- Langmead, B. and Salzberg, S. L. (2012) 'Fast gapped-read alignment with Bowtie 2', *Nat Methods*, 9(4), pp. 357–359. doi: 10.1038/nmeth.1923.
- Le, M. *et al.* (2012) 'Transforming growth factor Beta 3 is required for excisional wound repair in vivo', *PLoS One*, 7(10), p. e48040. doi: 10.1371/journal.pone.0048040.
- Lee, B. *et al.* (2014) 'Transcriptional mechanisms link epithelial plasticity to adhesion and differentiation of epidermal progenitor cells', *Dev Cell*, 29(1), pp. 47–58. doi: 10.1016/j.devcel.2014.03.005.
- Lewis, C. J. *et al.* (2014) 'Bone morphogenetic protein signaling suppresses wound-induced skin repair by inhibiting keratinocyte proliferation and migration', *Journal of Investigative Dermatology*. doi: 10.1038/jid.2013.419.
- Li, L. *et al.* (2019) 'TFAP2C- and Col17a1-Dependent Networks Sequentially Rearrange Chromatin Landscapes to Drive Human Epidermal Lineage Commitment', *Cell Stem Cell*, 24(2), pp. 271–284. doi: 10.1016/j.stem.2018.12.012.
- Li, M. *et al.* (2006) 'Topical vitamin D3 and low-calcemic analogs induce thymic stromal lymphopoietin in mouse keratinocytes and trigger an atopic dermatitis', *Proc Natl Acad Sci U S A*, 103(31), pp. 11736–11741. doi: 10.1073/pnas.0604575103.
- Liang, X. *et al.* (2012) 'Delayed cutaneous wound healing and aberrant expression of hair follicle stem cell markers in mice selectively lacking Ctip2 in epidermis', *PLoS One*,

7(2), p. e29999. doi: 10.1371/journal.pone.0029999.

Lichti, U., Anders, J. and Yuspa, S. H. (2008) 'Isolation and short-term culture of primary keratinocytes, hair follicle populations and dermal cells from newborn mice and keratinocytes from adult mice for in vitro analysis and for grafting to immunodeficient mice', *Nat Protoc*, 3(5), pp. 799–810. doi: 10.1038/nprot.2008.50.

Lien, W. H. *et al.* (2011) 'Genome-wide maps of histone modifications unwind in vivo chromatin states of the hair follicle lineage', *Cell Stem Cell*, 9(3), pp. 219–232. doi: 10.1016/j.stem.2011.07.015.

Lim, J. and Thiery, J. P. (2012) 'Epithelial-mesenchymal transitions: insights from development', *Development*, 139(19), pp. 3471–3486. doi: 10.1242/dev.071209.

Liu, N. *et al.* (2019) 'Stem cell competition orchestrates skin homeostasis and ageing', *Nature*. Springer US, 568(7752), pp. 344–350. doi: 10.1038/s41586-019-1085-7.

Losick, V. P., Fox, D. T. and Spradling, A. C. (2013) 'Polyploidization and cell fusion contribute to wound healing in the adult *Drosophila* epithelium', *Curr Biol*, 23(22), pp. 2224–2232. doi: 10.1016/j.cub.2013.09.029.

Mackay, D. R. *et al.* (2006) 'The mouse *Ovol2* gene is required for cranial neural tube development', *Dev Biol*, 291(1), pp. 38–52. doi: 10.1016/j.ydbio.2005.12.003.

Mah, E. J. *et al.* (2018) 'Collagen density modulates triple-negative breast cancer cell metabolism through adhesion-mediated contractility', *Scientific Reports*, 8(1). doi: 10.1038/s41598-018-35381-9.

Mani, S. A. *et al.* (2008) 'The epithelial-mesenchymal transition generates cells with properties of stem cells', *Cell*, 133(4), pp. 704–715. doi: 10.1016/j.cell.2008.03.027.

La Manno, G. *et al.* (2018) 'RNA velocity of single cells', *Nature*, 560(7719), pp. 494–

498. doi: 10.1038/s41586-018-0414-6.

Martin, P. and Lewis, J. (1992) 'Actin cables and epidermal movement in embryonic wound healing', *Nature*, 360, pp. 179–183.

Mascr , G. *et al.* (2012) 'Distinct contribution of stem and progenitor cells to epidermal maintenance', *Nature*, 489, pp. 257–262. doi: 10.1038/nature11393.

McCluskey, J. and Martin, P. (1995) 'Analysis of the tissue movements of embryonic wound healing--Dil studies in the limb bud stage mouse embryo', *Dev Biol*, 170, pp. 102–114.

Meador, J. P. *et al.* (2014) 'Massively parallel single-cell RNA-seq for marker-free decomposition of tissues into cell types', *Science*, 343(6172), pp. 776–779. doi: 10.1126/science.1247651.

Miao, Q. *et al.* (2014) 'Tcf3 promotes cell migration and wound repair through regulation of lipocalin 2', *Nat Commun*, 5, p. 4088. doi: 10.1038/ncomms5088.

Mills, A. A. *et al.* (1999) 'Col17a1 is a p53 homologue required for limb and epidermal morphogenesis', *Nature*, 398(6729), pp. 708–713. doi: 10.1038/19531.

Mitchison, T. and Cramer, L. (1993) 'Actin-based cell motility and cell locomotion', *Cell*, 84, pp. 371–379.

Morel, A. P. *et al.* (2008) 'Generation of breast cancer stem cells through epithelial-mesenchymal transition', *PLoS ONE*. doi: 10.1371/journal.pone.0002888.

Muller-Rover, S. *et al.* (2001) 'A Comprehensive Guide for the Accurate Classification of Murine Hair Follicles in Distinct Hair Cycle Stages', *JID*, 117(1).

Mustoe, T. *et al.* (1987) 'Accelerated healing of incisional wounds in rats induced by transforming growth factor-beta', *Science*, 237(4820), pp. 1333–1336.

- Nair, M. *et al.* (2006) 'Ovol1 regulates the growth arrest of embryonic epidermal progenitor cells and represses c-myc transcription', *Journal of Cell Biology*, 173(2), pp. 253–264. doi: 10.1083/jcb.200508196.
- Nassour, M. *et al.* (2012) 'Slug Controls Stem/Progenitor Cell Growth Dynamics during Mammary Gland Morphogenesis', *PLoS ONE*. doi: 10.1371/journal.pone.0053498.
- Navarini, A. A. *et al.* (2014) 'Genome-wide association study identifies three novel susceptibility loci for severe Acne vulgaris', *Nature Communications*. doi: 10.1038/ncomms5020.
- Nguyen, Q. H. *et al.* (2018) 'Profiling human breast epithelial cells using single cell RNA sequencing identifies cell diversity', *Nature Communications*. doi: 10.1038/s41467-018-04334-1.
- Nieto, M. A. *et al.* (1994) 'Control of cell behavior during vertebrate development by Slug, a zinc finger gene', *Science*, 264, pp. 835–839.
- Nieto, M. A. (2002) 'The snail superfamily of zinc-finger transcription factors', *Nat Rev Mol Cell Biol*, 3(3), pp. 155–166. doi: 10.1038/nrm757.
- Nieto, M. A. *et al.* (2016) 'Emt: 2016', *Cell*, 166(1), pp. 21–45. doi: 10.1016/j.cell.2016.06.028.
- Nowak, J. A. and Fuchs, E. (2009) 'Isolation and culture of epithelial stem cells', *Methods Mol Biol*, 482, pp. 215–232. doi: 10.1007/978-1-59745-060-7_14.
- Nunan, R. *et al.* (2015) 'Ephrin-Bs Drive Junctional Downregulation and Actin Stress Fiber Disassembly to Enable Wound Re-epithelialization', *Cell Rep*, 13(7), pp. 1380–1395. doi: 10.1016/j.celrep.2015.09.085.
- Odland, G. and Ross, R. (1968) 'Human wound repair', *J Cell Biol*, 39, pp. 135–151.

- Park, S. *et al.* (2017) 'Tissue-scale coordination of cellular behavior promotes epidermal wound repair in live mice', *Nat Cell Biol*, 19(3), pp. 155–164. doi: 10.1038/ncb3472.
- Park, S. A. *et al.* (2014) 'Full-thickness splinted skin wound healing models in db/db and heterozygous mice: implications for wound healing impairment', *Wound Repair Regen*, 22(3), pp. 368–380. doi: 10.1111/wrr.12172.
- Paternoster, L. *et al.* (2012) 'Meta-analysis of genome-wide association studies identifies three new risk loci for atopic dermatitis', *Nat Genet*, 44(2), pp. 187–192. doi: 10.1038/ng.1017.
- Pattison, J. M. *et al.* (2018) 'Retinoic acid and BMP4 cooperate with Col17a1 to alter chromatin dynamics during surface epithelial commitment', *Nature Genetics*, 50(12), pp. 1658–1665. doi: 10.1038/s41588-018-0263-0.
- Payre, F., Vincent, A. and Carreno, S. (1999) 'ovo/svb Integrates Wingless and DER pathways to control epidermis differentiation', *Nature*. doi: 10.1038/22330.
- Pedregosa, F. *et al.* (2011) 'Scikitlearn: Machine Learning in Python', *Journal of Machine Learning Research*.
- Picelli, S. *et al.* (2013) 'Smart-seq2 for sensitive full-length transcriptome profiling in single cells', *Nat Methods*, 10(11), pp. 1096–1098. doi: 10.1038/nmeth.2639.
- Picelli, S. *et al.* (2014) 'Tn5 transposase and tagmentation procedures for massively scaled sequencing projects', *Genome Res*, 24(12), pp. 2033–2040. doi: 10.1101/gr.177881.114.
- Plikus, M. V *et al.* (2008) 'Cyclic dermal BMP signalling regulates stem cell activation during hair regeneration', *Nature*, 451(7176), pp. 340–344. doi: 10.1038/nature06457.
- Plikus, M. V (2012) 'New activators and inhibitors in the hair cycle clock: targeting stem

cells' state of competence', *J Invest Dermatol*, 132(5), pp. 1321–1324. doi: 10.1038/jid.2012.38.

Plikus, M. V *et al.* (2017) 'Regeneration of fat cells from myofibroblasts during wound healing', *Science*, 355(6326), pp. 748–752. doi: 10.1126/science.aai8792.

Qiu, X., Mao, Q., *et al.* (2017) 'Reversed graph embedding resolves complex single-cell trajectories', *Nature Methods*, 14(10), pp. 979–982. doi: 10.1038/nmeth.4402.

Qiu, X., Hill, A., *et al.* (2017) 'Single-cell mRNA quantification and differential analysis with Census', *Nature Methods*, 14(3), pp. 309–315. doi: 10.1038/nmeth.4150.

Rasmussen, C. E. and Williams, C. K. I. (2006) 'Gaussian Processes for Regression', *Gaussian Processes for Machine Learning*. doi: 10.1093/bioinformatics/btq657.

Razzell, W., Wood, W. and Martin, P. (2011) 'Swatting flies: modelling wound healing and inflammation in *Drosophila*', *Dis Model Mech*, 4(5), pp. 569–574. doi: 10.1242/dmm.006825.

Redd, M. J. *et al.* (2004) 'Wound healing and inflammation: embryos reveal the way to perfect repair', *Philos Trans R Soc Lond B Biol Sci*, 359(1445), pp. 777–784. doi: 10.1098/rstb.2004.1466.

Richardson, R. *et al.* (2013) 'Adult zebrafish as a model system for cutaneous wound-healing research', *J Invest Dermatol*, 133(6), pp. 1655–1665. doi: 10.1038/jid.2013.16.

Rompolas, P. *et al.* (2012) 'Live imaging of stem cell and progeny behaviour in physiological hair-follicle regeneration', *Nature*, 487(7408), pp. 496–499. doi: 10.1038/nature11218.

Rompolas, P., Mesa, K. R. and Greco, V. (2013) 'Spatial organization within a niche as a determinant of stem-cell fate', *Nature*, 502(7472), pp. 513–518. doi:

10.1038/nature12602.

Rorth, P. (2009) 'Collective cell migration', *Annu Rev Cell Dev Biol*, 25, pp. 407–429.

doi: 10.1146/annurev.cellbio.042308.113231.

Rotzer, D. *et al.* (2006) 'Id proteins: Novel targets of activin action, which regulate epidermal homeostasis', *Oncogene*, 25(14), pp. 2070–2081. doi:

10.1038/sj.onc.1209230.

Sada, A. *et al.* (2016) 'Defining the cellular lineage hierarchy in the interfollicular epidermis of adult skin', *Nat Cell Biol*, 18(6), pp. 619–631. doi: 10.1038/ncb3359.

Sano, Y. *et al.* (2007) 'Col17a1 induces key target genes required for epidermal morphogenesis', *Proceedings of the National Academy of Sciences*. doi:

10.1073/pnas.0611376104.

Satija, R. *et al.* (2015) 'Spatial reconstruction of single-cell gene expression data', *Nature Biotechnology*, 33(5), pp. 495–502. doi: 10.1038/nbt.3192.

Saunders, L. R. and McClay, D. R. (2014) 'Sub-circuits of a gene regulatory network control a developmental epithelial-mesenchymal transition', *Development*. doi:

10.1242/dev.101436.

Savagner, P., Yamada, K. and Thiery, J. P. (1997) 'The zinc-finger protein slug causes desmosome dissociation, an initial and necessary step for growth factor-induced epithelial-mesenchymal transition', *J Cell Biol*, 137(6), pp. 1403–1419.

Scheel, C. *et al.* (2011) 'Paracrine and autocrine signals induce and maintain mesenchymal and stem cell states in the breast', *Cell*, 145(6), pp. 926–940. doi:

10.1016/j.cell.2011.04.029.

Schneider, M. R., Schmidt-Ullrich, R. and Paus, R. (2009) 'The hair follicle as a dynamic

miniorgan', *Curr Biol*, 19(3), pp. R132–42. doi: 10.1016/j.cub.2008.12.005.

Sha, Y. *et al.* (2019) 'Intermediate cell states in epithelial-to-mesenchymal transition', *Physical biology*. doi: 10.1088/1478-3975/aaf928.

Shaw, T. J. and Martin, P. (2009) 'Wound repair at a glance', *J Cell Sci*, 122(Pt 18), pp. 3209–3213. doi: 10.1242/jcs.031187.

Shirakata, Y. (2005) 'Heparin-binding EGF-like growth factor accelerates keratinocyte migration and skin wound healing', *Journal of Cell Science*, 118, pp. 2363–2370. doi: 10.1242/jcs.02346.

Shirley, S. H. *et al.* (2010) 'The skinny on Slug', *Mol Carcinog*, 49(10), pp. 851–861. doi: 10.1002/mc.20674.

Sorce, B. *et al.* (2015) 'Mitotic cells contract actomyosin cortex and generate pressure to round against or escape epithelial confinement', *Nat Commun*, 6, p. 8872. doi: 10.1038/ncomms9872.

Stone, R. C. *et al.* (2016) 'Epithelial-mesenchymal transition in tissue repair and fibrosis', *Cell Tissue Res*, 365(3), pp. 495–506. doi: 10.1007/s00441-016-2464-0.

Stringari, C. *et al.* (2012) 'Metabolic trajectory of cellular differentiation in small intestine by Phasor Fluorescence Lifetime Microscopy of NADH', *Scientific Reports*, 2(568). doi: 10.1038/srep00568.

Stringari, C. *et al.* (2015) 'In Vivo Single-Cell Detection of Metabolic Oscillations in Stem Cells', *Cell Reports*, 10(1), pp. 1–7. doi: 10.1016/j.celrep.2014.12.007.

Subramanian, A. *et al.* (2005) 'Gene set enrichment analysis: A knowledge-based approach for interpreting genome-wide expression profiles', *Proc Natl Acad Sci U S A*, 102(43).

- Terao, M. *et al.* (2011) 'Enhanced epithelial-mesenchymal transition-like phenotype in N-acetylglucosaminyltransferase V transgenic mouse skin promotes wound healing', *J Biol Chem*, 286(32), pp. 28303–28311. doi: 10.1074/jbc.M111.220376.
- Teschendorff, A. E. and Enver, T. (2017) 'Single-cell entropy for accurate estimation of differentiation potency from a cell's transcriptome', *Nature Communications*, 8(15599). doi: 10.1038/ncomms15599.
- Theveneau, E. and Mayor, R. (2013) 'Collective cell migration of epithelial and mesenchymal cells', *Cell Mol Life Sci*, 70(19), pp. 3481–3492. doi: 10.1007/s00018-012-1251-7.
- Thiery, J. P. *et al.* (2009) 'Epithelial-mesenchymal transitions in development and disease', *Cell*, 139(5), pp. 871–890. doi: 10.1016/j.cell.2009.11.007.
- Thomason, H. A. *et al.* (2012) 'Direct evidence that PKC α positively regulates wound re-epithelialization: correlation with changes in desmosomal adhesiveness', *J Pathol*, 227(3), pp. 346–356. doi: 10.1002/path.4016.
- Topley, G. I. *et al.* (1999) 'p21(WAF1/Cip1) functions as a suppressor of malignant skin tumor formation and a determinant of keratinocyte stem-cell potential.', *Proceedings of the National Academy of Sciences of the United States of America*, 96(16), pp. 9089–9094. doi: 10.1073/pnas.96.16.9089.
- Trapnell, C. *et al.* (2013) 'Differential analysis of gene regulation at transcript resolution with RNA-seq', *Nat Biotechnol*, 31(1), pp. 46–53. doi: 10.1038/nbt.2450.
- Trapnell, C. *et al.* (2014) 'The dynamics and regulators of cell fate decisions are revealed by pseudotemporal ordering of single cells', *Nat Biotechnol*, 32(4), pp. 381–386. doi: 10.1038/nbt.2859.

- Truong, A. B. *et al.* (2006) 'Col17a1 regulates proliferation and differentiation of developmentally mature keratinocytes', *Genes Dev*, 20(22), pp. 3185–3197. doi: 10.1101/gad.1463206.
- Unezaki, S. *et al.* (2007) 'Ovol2/Movo, a homologue of *Drosophila* ovo, is required for angiogenesis, heart formation and placental development in mice', *Genes Cells*, 12(6), pp. 773–785. doi: 10.1111/j.1365-2443.2007.01084.x.
- Vagnozzi, A. N., Reiter, J. F. and Wong, S. Y. (2015) 'Hair follicle and interfollicular epidermal stem cells make varying contributions to wound regeneration', *Cell Cycle*, 14(21), pp. 3408–3417. doi: 10.1080/15384101.2015.1090062.
- Veniaminova, N. A. *et al.* (2013) 'Keratin 79 identifies a novel population of migratory epithelial cells that initiates hair canal morphogenesis and regeneration', *Development*, 140(24), pp. 4870–4880. doi: 10.1242/dev.101725.
- Wang, D. *et al.* (2014) 'Identification of multipotent mammary stem cells by protein C receptor expression', *Nature*. doi: 10.1038/nature13851.
- Watanabe, K. *et al.* (2014) 'Mammary morphogenesis and regeneration require the inhibition of EMT at terminal end buds by Ovol2 transcriptional repressor', *Dev Cell*, 29(1), pp. 59–74. doi: 10.1016/j.devcel.2014.03.006.
- Watanabe, M. *et al.* (2017) 'Type XVII collagen coordinates proliferation in the interfollicular epidermis', *eLife*, 6. doi: 10.7554/eLife.26635.
- Wawersik, M. J. *et al.* (2013) 'Increased Levels of Keratin 16 Alter Epithelialization Potential of Mouse Skin Keratinocytes In Vivo and Ex Vivo', *Molecular Biology of the Cell*, 12(11), pp. 3439–3450. doi: 10.1091/mbc.12.11.3439.
- Wood, W. *et al.* (2002) 'Wound healing recapitulates morphogenesis in *Drosophila*

- embryos', *Nat Cell Biol*, 4(11), pp. 907–912. doi: 10.1038/ncb875.
- Yan, C. *et al.* (2010) 'Epithelial to mesenchymal transition in human skin wound healing is induced by tumor necrosis factor-alpha through bone morphogenic protein-2', *Am J Pathol*, 176(5), pp. 2247–2258. doi: 10.2353/ajpath.2010.090048.
- Yang, A. *et al.* (1999) 'Col17a1 is essential for regenerative proliferation in limb, craniofacial and epithelial development', *Nature*, 398(6729), pp. 714–718. doi: 10.1038/19539.
- Ye, X. *et al.* (2015) 'Distinct EMT programs control normal mammary stem cells and tumour-initiating cells', *Nature*, 525(7568), pp. 256–260. doi: 10.1038/nature14897.
- Zenz, R. and Wagner, E. F. (2006) 'Jun signalling in the epidermis: From developmental defects to psoriasis and skin tumors', *Int J Biochem Cell Biol*, 38(7), pp. 1043–1049. doi: 10.1016/j.biocel.2005.11.011.
- Zhang, Y. V *et al.* (2009) 'Distinct self-renewal and differentiation phases in the niche of infrequently dividing hair follicle stem cells', *Cell Stem Cell*, 5(3), pp. 267–278. doi: 10.1016/j.stem.2009.06.004.
- Zheng, Y. *et al.* (2005) 'Organogenesis from dissociated cells: generation of mature cycling hair follicles from skin-derived cells', *J Invest Dermatol*, 124(5), pp. 867–876. doi: 10.1111/j.0022-202X.2005.23716.x.
- Zheng, Y. *et al.* (2016) 'Isolation of Mouse Hair Follicle Bulge Stem Cells and Their Functional Analysis in a Reconstitution Assay', *Methods Mol Biol*, 1453, pp. 57–69. doi: 10.1007/978-1-4939-3786-8_8.
- Zhu, B. M. *et al.* (2008) 'SOCS3 negatively regulates the gp130-STAT3 pathway in mouse skin wound healing', *Journal of Investigative Dermatology*, 128(7), pp. 1821–

1829. doi: 10.1038/sj.jid.5701224.